Techniques for Nonlinear Distortion Suppression in Radio over Fiber Communication Systems

Biagio Masella

A Thesis

In

The Department

Of

Electrical and Computer Engineering

Presented in Partial Fulfillment of the Requirements

For the Degree of Doctor of Philosophy at

Concordia University

Montréal, Québec, Canada

January 2009

Your file Votre référence
ISBN: 978-0-494-63376-2
Our file Notre référence
ISBN: 978-0-494-63376-2

ABSTRACT

Techniques for Nonlinear Distortion Suppression in Radio over Fiber Communication Systems

Biagio Masella, Ph. D.
Concordia University, 2009

Radio over fiber (RoF) is a promising technology that will indisputably compete as a viable solution for future wireless, cellular and broadband networks. RoF, when combined with dense wavelength division multiplexing (DWDM), such as SONET/SDH, it can become a complete flexible and cost effective solution to the global telecommunication network, where asynchronous and synchronous communications may be efficiently supported.

Subcarrier modulation (SCM) is utilized to modulate a RF signal on light, which in turn will be transmitted by fiber. Unfortunately, the transmission in most cases may become corrupted by nonlinear distortion that is induced by the nonlinear response of the optical transmitter, optical receiver and chromatic dispersion of the single mode fiber (SMF). The nonlinear distortion degrades the receiver sensitivity, which leads to a poor bit error rate (BER) and spurious free dynamic range (SFDR). Ultimately, this will increase RoF system costs and render it impractical.

The objective of this thesis is to develop linearization methods that reduce the nonlinear distortion, increase receiver sensitivity and increase SFDR. The designs should also address the entire RoF system by combating the optical power fading issue that will

be discussed in Chapter 2 without significantly adding great expense and complexity to the RoF system.

Four optical linearization methods are proposed and shown through extensive simulation and/or experimentation to outperform similar existing linearization systems described in literature. The proposed single wavelength balanced system is shown to improve the suppression of 2^{nd} order distortion over the dual wavelength balanced system, thereby leading to greater improvement in receiver sensitivity and BER. Furthermore, the design also suppresses relative intensity noise (RIN). The proposed tunable fiber Bragg grating (FBG) balanced system is capable of suppressing both 2^{nd} and 3^{rd} order distortions despite which RF carrier that is used. Furthermore, it was shown to outperform the conventional RoF system in terms of receiver sensitivity and BER. The proposed asymmetric Mach-Zehnder modulator (MZM) has been shown to generate optical single sideband (OSSB) transmissions and outperform the dual-parallel modulator, by improving 3^{rd} order intermodulation distortion (3IMD) suppression and increasing SFDR. The final proposed linearization method is the mixed-polarization MZM, where OSSB is also generated and outperforms the conventional OSSB RoF system in terms of 3IMD suppression and SFDR. Furthermore, close form expressions for SFDR are developed for the final two designs, which is crucial in study of their stability and performance.

Acknowledgments

I would like to thank Dr. J. X. Zhang for his guidance, discussions and long hours devoted to guiding my research and writings. I would like to also thank B. Hraimel for his insightful discussions and experimental lab work at the Advanced Photonics System Lab at Concordia University, Montréal, Canada that allowed me to include experimental work in my thesis. I would like to express my gratitude to Dr. M.N.S. Swamy for providing me with a thesis example. I would also like to extend my gratitude to Lise and Aimé Villeneuve for their encouragement and support throughout my studies. Finally, I am grateful to my parents and family for their support, encouragement and understanding.

Dedicated to

My parents

Modestina De Santis and Giuseppe Masella

For their continuous love and support.

Table of Contents

List of Figures

List of Tables

List of Acronyms

2HD	:	Second order harmonic distortion
2IMD	:	Second order intermodulation distortion
3HD	:	Third order harmonic distortion
3IMD	:	Third order intermodulation distortion
ADSL	:	Asynchronous digital subscriber line
ADM	:	Add drop multiplexer
AGC	:	Automatic gain control
AM-QAM	:	Amplitude modulation-quadrature amplitude modulation
AM-VSB	:	Amplitude modulation-vestigial sideband
ASC	:	Automatic slope control
ASK	:	Amplitude shift keying
B-LEAM	:	Balanced-linear electro-absorption modulator
B-NEAM	:	Balanced-nonlinear electro-absorption modulator
BBI	:	Balanced bridge interferometer
BER	:	Bit error rate
BPF	:	Bandpass filter
BPSK	:	Binary phase shift keying
CATV	:	Cable antenna television
CNR	:	Carrier to noise ratio
CB-NEAM	:	Conventional-balanced-nonlinear electro-absorption modulator
C-NEAM	:	Conventional-nonlinear electro-absorption modulator
CSO	:	Composite second order
CTB	:	Composite triple beat
CW	:	Continuous wave
DEMUX	:	De-multiplexer
dB	:	Decibel

DBS	:	Direct broadcast satellite
DFB	:	Distributed feedback
DM-DFB	:	Directly modulated distributed feedback
DSB	:	Double sideband
DWDM	:	Dense wavelength division multiplexing
EAM	:	Electro-absorption modulator
EAT	:	Electro-absorption transceiver
EDFA	:	Erbium doped fiber amplifier
EOM	:	Electro-optical modulator
FBG	:	Fiber Bragg grating
FWM	:	Four wave mixing
GHz	:	Gigahertz
GVD	:	Group velocity dispersion
HEC	:	Hybrid electrical coupler
HD	:	Harmonic distortion
HFC	:	Hybrid fiber coaxial
HP	:	Harmonic product
Hz	:	Hertz
IEEE	:	Institute of Electrical and Electronic Engineers
IF	:	Intermediate frequency
IMD	:	Inermodulation distortion
IMP	:	Intermodulation product
IP	:	Internet protocol
$LiNbO_3$	:	Lithium niobate oxide
LMPN	:	Laser mode partition noise
LNA	:	Low noise amplifier
MHE	:	Master head end
Mux	:	Multiplexer
MZI	:	Mach-Zehnder interferometer
MZM	:	Mach-Zehnder modulator

ODSB	:	Optical double sideband
OSSB	:	Optical single sideband
OTN	:	Optical termination network
OTU	:	Optical termination unit
PLL	:	Phase-locked-loop
PON	:	Passive optical network
PRBS	:	Pseudo-random bit stream
PSTN	:	Public switched telephone network
RF	:	Radio frequency
RIN	:	Relative intensity noise
RMS	:	Root mean square
ROF	:	Radio over fiber
ROF-WDM	:	Radio over fiber-wavelength division multiplexing
SBS	:	Stimulated Brillouin scattering
SCM	:	Subcarrier multiplexing
SCM-DWDM	:	Subcarrier multiplexing-dense wavelength multiplexing
SDH	:	Synchronous digital hierarchy
SFDR	:	Spurious free dynamic range
SMF	:	Single mode fiber
SNR	:	Signal to noise ratio
SONET/SDH	:	Synchronous optical network / Synchronous digital hierarchy
SRS	:	Stimulated Raman scattering
SSB	:	Single sideband
TDMA	:	Time division multiple access
XPM	:	Cross phase modulation

List of Symbols

m	:	Modulation index
$\Re$	:	Responsivity
q	:	Electron charge
$\langle i_{ns}^2 \rangle$	:	Means square shot noise
$\langle i_a \rangle$	:	Average PIN photodiode current
B_e	:	Electrical noise bandwidth or channel bandwidth
B_o	:	Optical filter bandwidth
f_k	:	k^{th} RF carrier
G	:	EDFA gain
P_{sp}	:	Spontaneous emission power at the output of the EDFA
$\overline{P_T}$	:	Laser mean power
h	:	Quantum efficiency
n_{sp}	:	Population inversion parameter
P_L	:	Fiber distribution and splitting loss
P_{Out}	:	Output power
P_{In}	:	Input power
$P_{In,ave}$	:	Average input power
$V(t)$	:	Applied DC bias and the modulating signal voltage
$f(\ )$	:	Transfer characteristics for the EAM
Ω	:	Radio frequency carrier
f_λ	:	Optical frequency at wavelength λ

v_m	:	Modulating signal voltage
v_b	:	DC bias
V	:	Modulating signal voltage
E_{In}	:	Average optical electric field input
E_{Out}	:	Output optical electric field
ω	:	Optical angular frequency
Δf	:	RF carrier frequency
$\Delta\phi$	:	Differential phase shift
ΔT	:	Propagation delay
c	:	Speed of light
D	:	Chromatic dispersion
L	:	Fiber length
L_{Period}	:	Periodic fade fiber length
$\Delta\omega$	:	RF angular frequency
$\Delta\lambda$	:	Wavelength spacing
$J(\ )$	:	Bessel function of the first kind
T	:	Magnitude transmission polynomial coefficients
α	:	Alpha factor
I	:	Received photocurrent
γ	:	Splitting ratio
τ	:	Relative time delay
ψ	:	Initial optical phase difference
φ	:	Subcarrier phase
V_π	:	Half wave switching voltage

Chapter 1

1 Introduction

1.1 Introduction

In the past two decades, telecommunication networks have been evolved in exploiting other telecommunication markets and meet the needs of an ever growing demand for bandwidth and services. After the global acceptance of the Internet in the mid 1990's and government deregulation act that allows telephone (local and long distance), cable TV, wireless and broadcasting companies to enter one another's markets, the need for more bandwidth provided at a lower cost has never been a greater priority. The objective of this chapter is to provide a background in broadband access networks, such as cable, cellular, wireless broadband and passive optical networks (PON). The major access networks will be described and an explanation as to how RoF may alleviate the deficiencies of traditional fiber optic and broadband networks is given. Also explained is how optical SCM and RoF systems function.

Traditional fiber optic communications mainly dealt with digital baseband, TDMA and DWDM, such as SONET/SDH. This form of communication transportation was mainly developed around digital voice communications and does not natively suit new evolving asynchronous communications technologies, such as Ethernet and TCP/IP. Because SONET/SDH is a synchronous digital communication transport, which makes use of TDMA and bit interleaving, the system clock is a crucial component in the

functioning of this system and makes it inherently expensive. For these reasons broadband access networks, such as hybrid fiber CATV (HFC), PON and RoF systems are require for access service for the customer. [1].

Since its first demonstration in 1990 in mobile networks, RoF systems have gained tremendous research interest [2]. RoF systems are an enabling technology, which will allow telecommunications companies to relay digital baseband and RF analog signals, such as WiFi, WiMax and mm-wave through the wide bandwidth of fiber in a cost effective manner. RoF systems make use of SCM and frequency division multiple access (FDMA), which will be further explained in this chapter, so it is inherently able to transport synchronous and asynchronous communication data. The main issue is to accurately recuperate the transmitted RF signals, which is where the issue of system nonlinearity plays a monumental role. The nonlinearity arises mainly from the frequency response of the optical transmitter, and receiver, along with other optical components, such as fiber. For example, the Mach-Zehnder modulator (MZM) has a sinusoidal frequency response, which will produce an optical transmission with nonlinearities. In situations where composite multiple RF channels need to be transmitted, higher-order distortion may be induced by nonlinearities in RoF systems, and thus these higher order distortion components will lead to lower SNR for neighboring channels. Optical system designers typically would have to install expensive optical filters, increase optical transmission power or unequally space RF channels allocations to increase SNR, which would undoubtedly increase complexity and cost. Figure 1.1 shows the performance comparison of analog and digital transport systems. It is seen from the figure that in the case of analog transport, there is a steady decline in performance due to nonlinear distortion, while for digital transport there is a constant performance until it is overcome

by quantization noise and synchronization loss. Beyond this point there is a dramatic performance loss. This indicates that digital communication transport is better choice for long haul transmission systems, and analog communication transport is a better choice for short haul transmission systems or as an access network, because of the gradual decline in performance and lower cost, so optical system designers are opting to use them together [3].

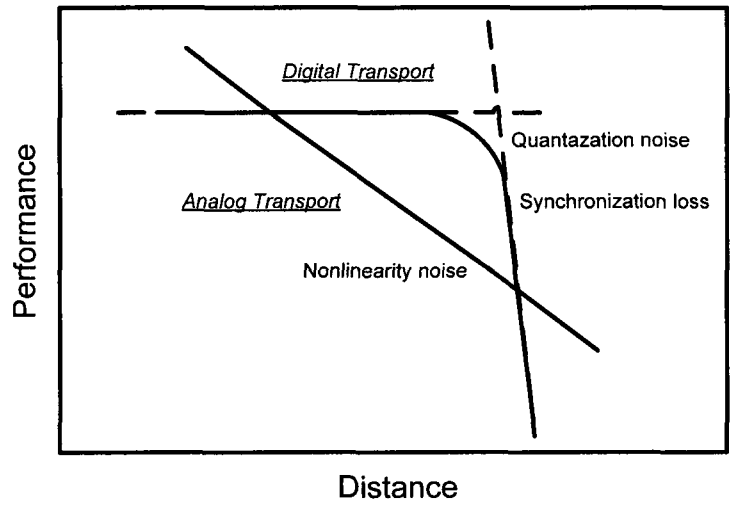

Figure 1.1 Digital (SONET/SDH) versus analog (RoF) communication transport [3].

1.2 Background and Theory

1.2.1 Hybrid Fiber Coaxial CATV Access Background

The telephone companies in North America have decided to exploit digital cable television markets by providing digital TV services via direct broadcast satellite (DBS) communications. The main issue with this technology is that the bandwidth is extremely

expensive and rarely allows for two way communications. They have also added broadband Internet services over their conventional copper telephone lines via asynchronous digital subscriber lines (ADSL) modems, which have limited bandwidth of 6.5 Mbit/s and distances to the customer premise must be less than 4.5 km depending on line signal conditions. On the other hand, cable companies have upgraded their old analog television broadcast to a bidirectional interactive hybrid fiber/cable access system. This new system allows for services such as, broadcast digital video, video on demand (VoD), web TV, Internet, IP telephony, TDMA telephony, IP video conferencing and multimedia services.

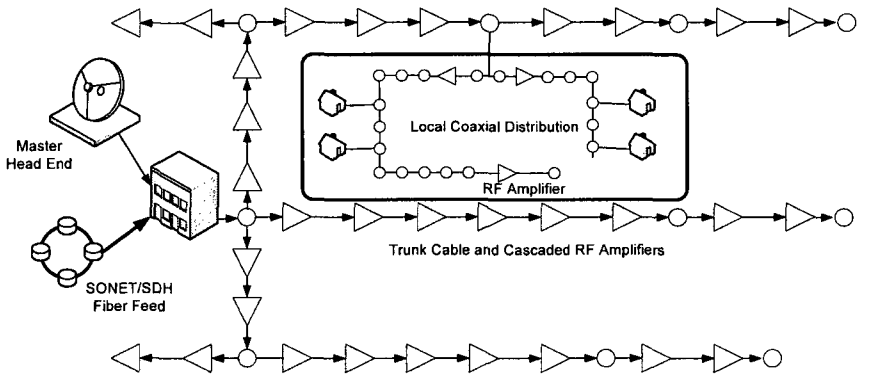

Figure 1.2 Traditional coaxial CATV broadcast system [4, 5].

1.2.2 Traditional Coaxial CATV Broadcast System

Traditional coaxial cable CATV systems use a tree and branch architecture as shown in Fig. 1.2. All signals to be broadcasted to customers are gathered at a master head end (MHE), such as satellites, trunk cables and SONET/SDH fiber feeds. They are amplitude modulated with vestigial sideband (AM-VSB) on different RF subcarriers, combined into

a single broadband signal and transmitted over a signal coaxial cable. The coaxial cable undergoes repeated branching with power splitters until it eventually reaches all streets in a community. The broadcast architecture is very cost effective, but it has a number of inherent limitations such as, broadband RF amplifiers are required every 0.5 km to overcome cable and branching losses. The amplifiers operate in a long cascaded chain and each adds noise and intermodulation distortion to the broadband signal. Furthermore, each amplifier must be adjusted to provide a very precise overall gain, frequency response and output power level, so that customer equipment operates correctly and does not become damaged. Total information capacity is also limited by high cable loss above 500 MHz, when many cascaded amplifiers are used to reach a wide community. The reliability and cost of the service limits the quality of service to subscribers.

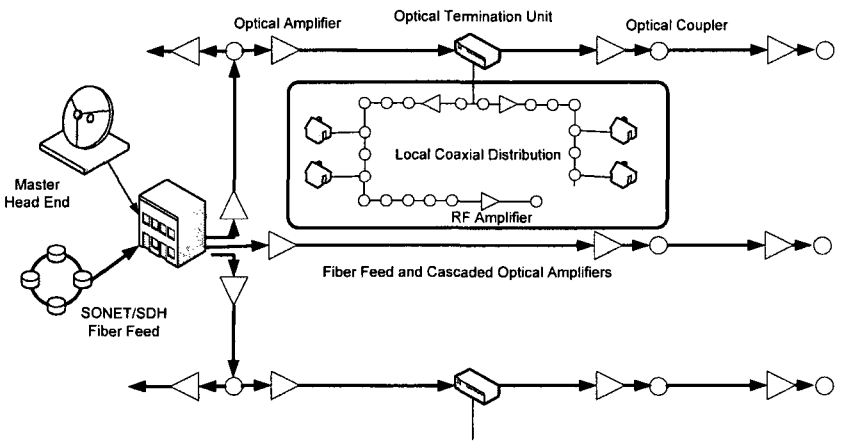

Figure 1.3 Hybrid fiber coaxial (HFC) broadcast system [4, 5].

1.2.3 Hybrid-Fiber Coaxial Broadcast System

Many of the inherent limitations of the coaxial cable CATV broadcast system may be overcome by breaking up the cascaded RF amplifier coaxial distribution network into a series of very short sections. Each section would then be fed from the MHE via an optical fiber. This has the effect of increasing channel capacity, improving RF channel to noise ratio, decreasing intermodulation distortion and increasing reliability. Such systems are known as hybrid fiber coaxial (HFC) systems. The HFC CATV system is depicted in Fig. 1.3. The composite subcarrier broadcast signal is modulated onto an optical carrier at the MHE via SCM. Each small coaxial network is fed by a low-loss optical fiber distribution network. An optical receiver at the optical termination unit (OTU) converts the optical signal back into a broadband RF spectrum suitable for local coaxial cable distribution to subscribers [4, 5].

Now the overall performance of an HFC CATV system depends on the linearity and noise characteristics of the analog optical fiber distribution system. A simple and low cost system may be achieved if AM-VSB linear modulation is maintained throughout. The only signal conversion that is required outside the MHE is from optical to electrical at each OTU. Hence, as shown in Fig. 1.4, the block diagram of the fiber backbone distribution system is only comprised of three components: the transmitter, fiber network and receiver.

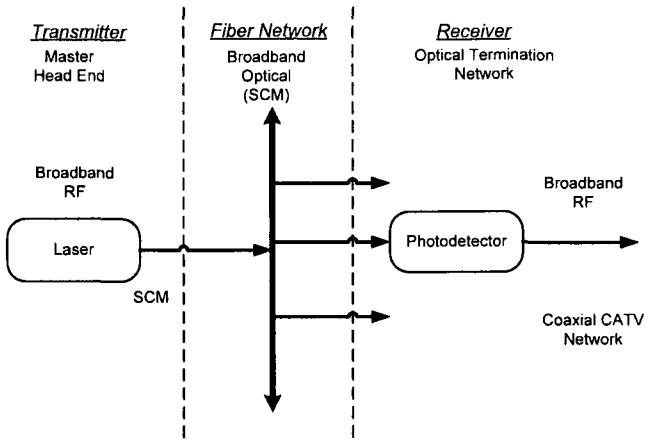

Figure 1.4 Block diagram of an optical fiber backbone network in an HFC system [4, 5].

1.2.4 Noise in a HFC Broadcast System

There are many processes that degrade the performance of a HFC broadcast system. The average photocurrent at the photodetector depends on the laser output power, the losses in the fiber cable, splitting components and the optical transmitter / receiver response. The photocurrent should be kept high to give a wide dynamic range, however this can lead to increased nonlinearity in the photodiode. The RF composite video modulated subcarrier signal in a directly modulated system varies the laser output in a nominally linear fashion. The RF signal current for each video channel depends on the modulation index (m), which is the measure of the ratio of peak modulation of each channel (subcarrier) to average optical power. For analog TV systems, the minimum carrier to noise ratio (CNR) must exceed 45 dB in order to satisfy the specification for minimum subjective television picture quality. Therefore, signal levels must be high at all stages in the CATV network and directly modulated lasers must operate with as high modulation index as possible, but increasing the modulation index also leads to increased nonlinearity. The maximum

usable modulation index is limited by the laser, which is the predominant source of nonlinearity in a directly modulated CATV system.

Also due to the quantum nature of light, the photodiode current gives rise to shot noise and the RF amplifier at the OTU contributes thermal noise described by the noise figure. Relative intensity noise (RIN) of the laser adds to the received noise and places an ultimate limit on the system noise. The channel carrying capacity of directly modulated lasers is fundamentally limited when the product of the number of channels and the modulation depth / channel exceeds the threshold current of the laser. This can occur occasionally with random phasing of the subcarriers causing the composite signal laser drive current to fall below the threshold current and this will lead to clipping distortion [5].

Optical noise impairments in optical CATV systems are laser RIN and modal instabilities due to optical reflections into the laser, leading to interferometric intensity noise. This results from mixing between directly received signals, delayed reflected signals and laser mode partition noise (LMPN). Systems using 1550 nm fiber and direct laser modulation will experience an increase in second order distortion due to the interaction of laser chirp and fiber dispersion [6-8]. It has been shown in [9] that the nonlinear noise due to dynamic laser clipping can cause a significant turn on or lasing delay with relaxation oscillations. Dynamic clipping distortion can dominate over other nonlinear distortion even when a laser diode is weakly clipped. Externally modulated optical transmissions, which makes use of a continuous wave (CW) lasers followed by a external optical modulator may reduce second order distortion and eliminate laser chirp,

but will have higher third order distortion. The third order distortion is caused by the inherently nonlinear power response characteristics of the external optical modulator.

1.2.5 Bidirectional Interactive Hybrid Fiber Coaxial Broadcast System

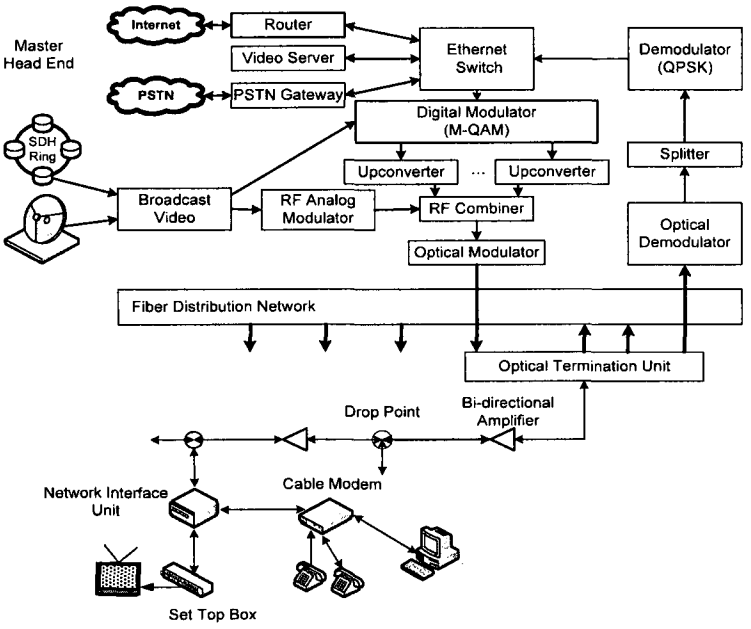

Figure 1.5 Bidirectional interactive hybrid fiber coaxial CATV system [10, 11].

Today HFC cable access system has evolved further to become a bidirectional interactive HFC cable access system as shown in Fig. 1.5. Bidirectional CATV system allows a network to be used for HFC CATV, along with data communications and telephony. A conventional broadcast HFC network is converted into a two way interactive system by adding equipment for the Internet and telephone access at the MHE. Upstream data is handled by separate fibers or may be wavelength division multiplexed on one fiber to the OTUs. Upgrading the coaxial cable access network mainly involves replacing all unidirectional (downstream) RF amplifiers with bidirectional RF amplifiers [10, 11]. Figure 1.6 shows an example of a SONET/SDH Erbium Doped Fiber Amplifier (EDFA)

based multi-wavelength, multi-channel hybrid AM-QAM CATV transmission with the three main access network technologies, bidirectional interactive HFC cable, PON and RoF, where PON and RoF will be further described in this chapter.

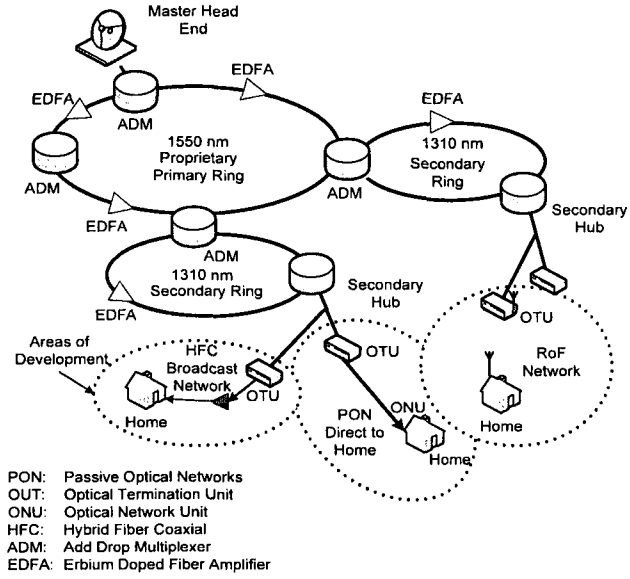

Figure 1.6 SONET/SDH EDFA based CATV distribution system using WDM primary ring with individual wavelengths optically dropped to the secondary rings and the three competing access technologies [11-13].

In order to maintain acceptable AM CNR the optical power budget of a 1310 nm directly modulated laser transmitter system is typically limited to around 10 dB [11-13]. This moderate power budget imposes upper limits on the length of the optical link and the number of optical power splitters. Many applications, such as long distance super trunking and high capacity HFC CATV distribution systems, which use PON structures, require a much higher link budget that can be provided by a directly modulated distributed feedback (DFB) laser [11].

The MHE transmits on multiple wavelengths usually around 1550 nm over a proprietary primary ring. The multi-wavelengths allow selective narrowcasting to

secondary rings. Each wavelength carries a mixture of AM and digital 64/256 QAM on subcarriers or at baseband using SONET/SDH transmission protocols. One or more wavelengths are connected to each secondary ring using add-drop multiplexers (ADMs) and the secondary hubs transfer data from the secondary rings to 1310 nm bidirectional hybrid HFC CATV system. PONs fed OTUs, which may also be extended to the optical network units (ONU) at each customer premise. RF add-drop multiplexers at the local hub and RoF systems can further target specific segments of the service area.

1.2.6 Ethernet Passive Optical Networks

Ethernet passive optical networks (EPON) are becoming a competing access network technology with the deregulation of the telecommunication industry, Internet spawning demand for broadband services, and rapid decline in cost of optical fiber and Ethernet components. It is being considered as a possible solution for the connection between the central office (CO) and business or residential customer locations. EPON has already evolved greatly from its debut in the mid 1990s with asynchronous transfer mode PON (APON), which was design around asynchronous transfer mode (ATM) protocols to support SONET rings, optical digital subscriber 3 (DS3) and copper base DS1 lines. EPON is emerging as the choice for local loops, such as fiber-to-the-business (FTTB) and fiber-to-the-home (FTTH), because of the short comings APON, such as lack of video capabilities and inappropriate bandwidth.

EPON is addressing the cost of running "point-to-point" fiber from customer location to the CO and installing costly active electronics, such as regulators, amplifiers and lasers at both ends of the fiber by using a point-to-multipoint technology instead. The point-to-

multipoint technology is a single feeder fiber that is split into 32 to 128 bidirectional runs that span up to 20 km in length at a bit rate of 1.25 Gbps. The two main components used for bidirectional transmission of packets between the CO and end user are the optical line terminal (OLT) and the optical network unit (ONU). The OLT routes packets through a specific optical feeder line to multiple ONUs. The ONU provides the interface between the end user's data, video and telephony networks and the EPON. The ONU also converts the optical transmission to the appropriate electrical signals compatible to the end user's equipment and routes via layer 2 and layer 3.

The data traffic flow broadcasted downstream and upstream in an EPON uses different technologies. The data broadcasted downstream as shown in Fig. 1.7 uses variable length packets up to 1518 bytes according to IEEE 802.3 to transmit packets from the OLT to ONU using a wavelength of 1510 nm. Packets destined for a specific users are allow through the user's ONU, while others are blocked. In the upstream traffic flow, EPON is utilizing TDM technology in which the transmission time slots are dedicated to the ONUs. The time slots are synchronized and do not interfere with other ONU's transmissions by transmitting a one byte code every 2 ms to synchronize the ONUs with the OLTs using a wavelength of 1310 nm.

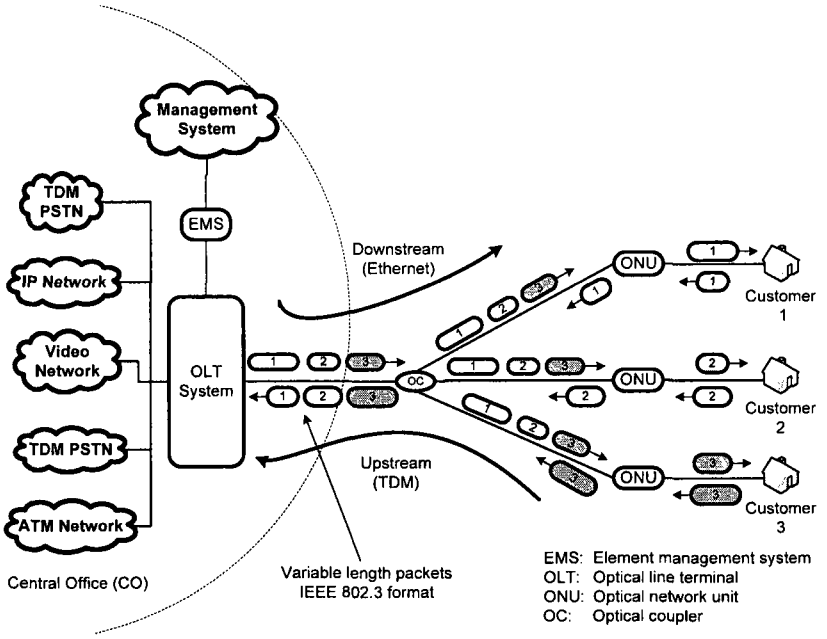

Figure 1.7 Downstream and upstream traffic flow in an EPON [14].

It is important to note that one of the greatest obstacles for the acceptance and deployment EPON is the cost of the ONU, which is located at every customer location in the FTTB and FTTH. This cost is not shared among many subscribers and typically represents 70% of the system cost in FTTB, and in FTTH deployment it can account for approximately 80%. Unlike RoF systems, which just relays RF signals onto the fiber and therefore there is no need for an ONU at the customer location [14].

1.2.7 Dense Wavelength Division Multiplexing as a Long Haul Transport Technology.

The use of dense wavelength division multiplexing (DWDM) as a long haul transport technology has recently emerged as a practical means for the targeted delivery of interactive services over HFC CATV networks. DWDM has the advantage of being transparent, flexible and easily upgraded. The downstream bandwidth, which is originally

allocated to multiple nodes, may be re-allocated to a smaller number of nodes as the number of subscribers increase. As the services increase, additional wavelengths may be added to the system without adding to the fiber count. Upstream data from multiple fiber nodes are aggregated and transmitted to the MHE also over DWDM networks [15].

SCM-DWDM systems impose higher requirements on the optical components compared with baseband digital systems, because the tolerance to nonlinear distortion of the signal is much lower. Nonlinear distortion can often result from DWDM filter passband tilt and EDFA gain tilt. These dense wavelength systems also exhibit fiber nonlinear effects such as cross-phase modulation (XPM), four-wave mixing (FWM) and stimulated Raman scattering (SRS) [15]. All of these nonlinear processes contribute to optical interference or crosstalk between the multiple optical channels.

In order to achieve the maximum CNR for a given optical link budget, the modulation index must be as large as possible, so that the effects of laser RIN, fiber losses and receiver noise can be minimized. On the other hand, the modulation index is limited so that unacceptably large nonlinear distortions and clipping effects are reduced [16, 17]. To meet the optical CATV system specifications, a variety of pre-distortion, feed-forward and distortion cancellation circuits are used. The CNR depends on parameters such as, modulation index, average photocurrent, RIN, second order harmonic and intermodulation and third order harmonic and intermodulation distortions [11-13]. In this thesis the focus will be on suppressing second and third order distortions, so that CNR is improved to meet the minimum subjective television picture quality. The distortions originate from the nonlinearities in the directly modulated laser, fiber and photodetector. For the laser, the intrinsic nonlinearities are described by the coupling of the injected

carrier density and the photon density in the laser's active region. Nonlinear effects such as carrier diffusion [18], spatial and spectral hole burning [19, 20] and photon absorption and damping due to spontaneous emission [21] will influence the nonlinear term in the rate equations.

These DWDM systems also exhibit fiber nonlinear effects such as cross-phase modulation (XPM), four-wave mixing (FWM) and stimulated Raman scattering (SRS). XPM occurs when optical modulation intensity fluctuation in one channel modulates the phase of the other co-propagating waves. Fiber group velocity dispersion (GVD) will convert these phase variations into amplitude fluctuations or crosstalk. FWM is a third order nonlinearity similar to composite triple beat (CTB) in electrical nonlinear systems. Two optical signals at different frequencies interact and generate a new optical signal at a third frequency [15]. Stimulated Brillouin scattering (SBS) is a process where higher frequency channels are depleted and lower frequency channels are amplified. Hence, the optical intensity of a modulated higher frequency channel will modulate the intensity of the lower frequency signal causing crosstalk. There are two primary mechanisms identified in photodetectors that produce nonlinear distortion in SCM transmission, space charge induced and absorption in undepleted semiconductor regions [22-25].

All harmonic and intermodulation products arising from different phase subcarriers will add on an incoherent or root mean square (RMS) basis. The total nonlinear distortion noise is obtained by adding up the number of each type of distortion terms in each channel [26, 27].

1.3 Benefits of RoF to Cellular and Broadband Networks

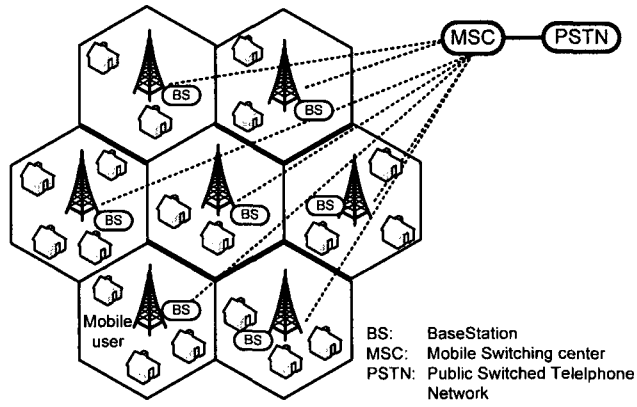

Figure 1.8 Conventional cellular networks.

Traditional wireless broadband access networks are very similar to large cell cellular systems, which consist of large cells with an expensive antenna located in the center of each cell as shown in Fig. 1.8 [3, 28]. These antennas are very expensive to build and maintain because of their complexity. All the antennas are directly connected to a base station (BS). The base stations are then connected to a mobile switching center (MSC) or mobile telephone switching office (MTSO) by land lines, where in turn the MSC is connected to the public switched telephone network (PSTN). Because of the limitation of available RF bandwidth, the antennas are deployed in a cellular spectral reuse pattern. The spectral reuse allows the communication network to reuse the same carrier frequencies of neighboring cells, because the radio transmission should be effectively faded as it reaches the boundary of each cell, thereby making it electromagnetically

isolated. This of course provided that the antenna power is adjusted correctly depending on terrain, structure and the use of directional antennas. The capacity of such systems is proportional to the geographical density of its component base station. High capacity networks require a large number of base stations with each covering a relativity small geographical region [29, 30].

It is obvious that it is not practical or economical to have complex base stations co-located at each antenna along with the infrastructure that goes along with it. So a more economical solution is to use RoF to rely radio signals from distant base stations to remote inexpensive antennas, this is seen in Fig. 1.9. There will be one inexpensive remote antenna per picocell, which is 10 to 200 m in diameter. Many picocells may be grouped together to form a microcellular network, which is 200 m to 1 km in diameter. The microcellular network is used in high traffic density regions, such as suburban areas. Many microcellular networks may be grouped together to form a macrocellular network. This cellular network has a significant foot print of 16 to 48 km in diameter and will have an inexpensive base station in the center of it. A mobile switching center controls all traffic within the market via the base station and is interconnected to the public switched telephone network. The service areas will be situated tens of kilometers away from the expensive base stations [29, 30].

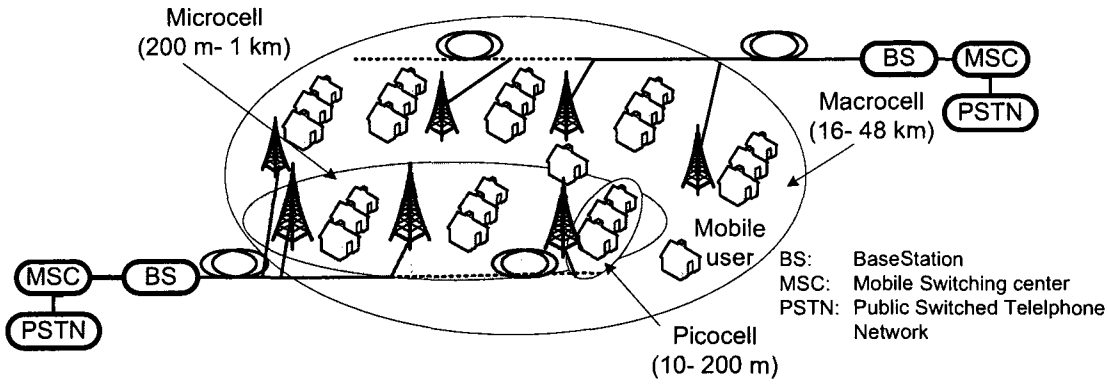

Figure 1.9 RoF wireless networks.

1.4 What is Optical Subcarrier Modulation?

Optical subcarrier modulation, which is also known as optical analog modulation, is a method used to modulate RF signals onto light. The idea may further be extended to modulate many RF signals onto light with the use of frequency division multiplexing (FDM). Figure 1.10 shows the general configuration of subcarrier modulation, where the composite RF signal made up of n-RF carriers Ω_1 to Ω_n, which are fed into an electro-optical modulator (EOM), which modulates a CW laser set to frequency of f_λ.

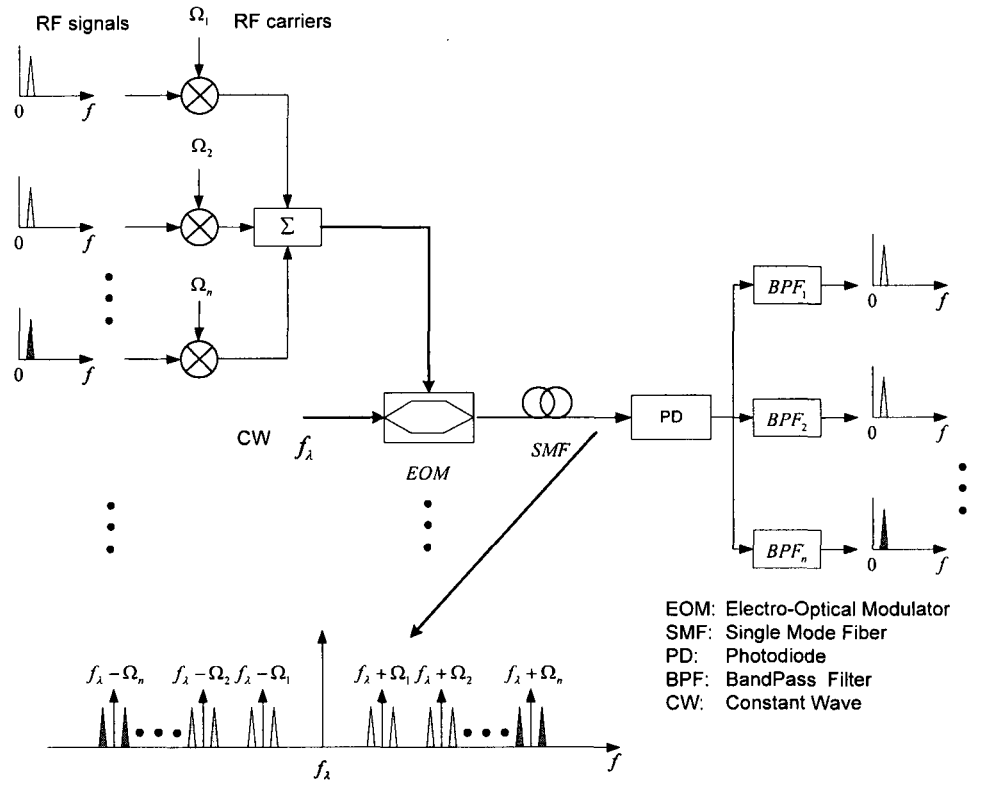

Figure 1.10 Multiple wavelength RoF system in which one wavelength carries multiple optical subcarriers.

The optical spectrum which is shown at the bottom of Fig. 1.10 is then received by the photodetector, where the received electrical signal is simultaneously fed to n-bandpass filters (BPF). Each BPF has its center frequency tuned to the original RF carrier frequency so that the original data transmission may be recovered. Instead of using BPFs, one may use homodyne or heterodyne detection, which will require a phase-locked-loop (PLL) and lowpass filter (LPF) to recover the original data transmission. The idea may be further expanded to include DWDM, where many sets of composite RF signals may be modulated with a separate wavelength and EOM, this will be further explained later in this chapter [31].

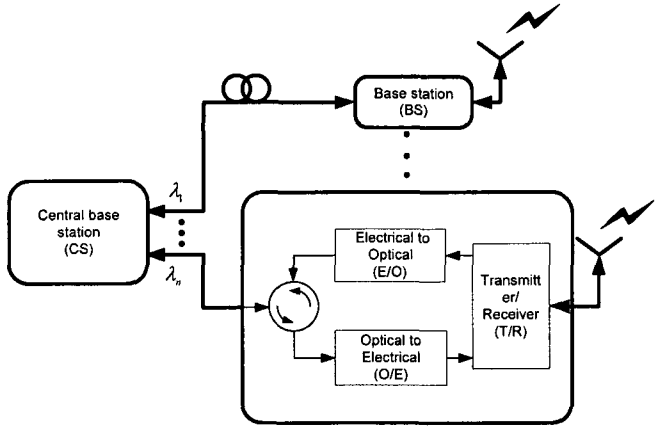

Figure 1.11 Block diagram of a RoF broadcast architecture.

1.5 What is Radio over Fiber?

Basically, radio over fiber (RoF) is a technology that relays RF analog or digital signals through optical fiber. Figure 1.11 shows the general RoF architecture, where each simple base station is connected back to the central station through fiber optic cables. Any wireless service may be received by the transceiver and the RF signal will be modulated onto a specific optical carrier allotted to that specific base station. Many optical carriers may be modulated and then optically coupled together before being transmitted back to the central station [31].

Figure 1.12 shows the details of a RoF uplink and downlink system, where the photodiode and optical modulator may be implemented with an electro-absorption transceiver (EAT). In this configuration the downlink will transmit two or more optical signals with a wavelength separation of 0.5 nm, once detected by the photodetector at the base station this will generate a beat frequency of around 60 GHz for wavelengths

between 1530 and 1565 nm or optical C-band. This beat frequency can be separated and be used as an intermediate frequency (IF) carrier. Because optical heterodyning technique is used one must take great care to keep the phase noise minimal [31].

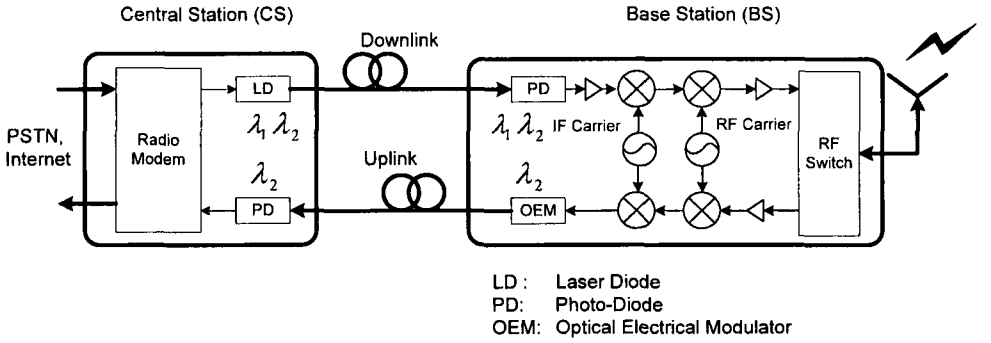

Figure 1.12 Detailed description of a RoF uplink and downlink system.

Figure 1.13 shows that DWDM and RoF may be combined to provide long haul transmission with the added cost benefit of RoF, where analog to digital and digital to analog converters are required. But this configuration may be also implemented for the short haul and these converters are not required, so that analog signals are transmitted to the destination without being converted from analog to digital and vice versa.

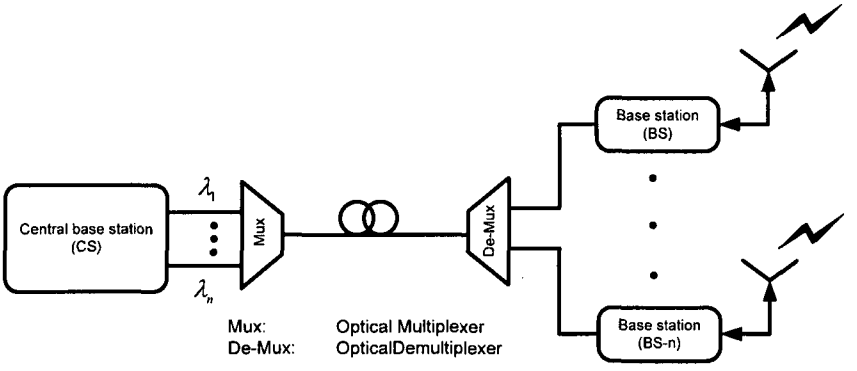

Figure 1.13 Block diagram for the combination of DWDM and RoF, known as RoF-WDM architecture.

1.6 Nonlinearity Issue in the Optical Modulator

RoF is relatively new and promising technology that will allow the merging of many different telecommunications and broadcasting services. The technology will allow the transparent simultaneous relaying of different millimeter and microwave wave transmissions despite the modulation formats and bit rates. The nonlinear transfer function of the optical modulator was not a great issue when used for digital optical communications, but has become a limiting factor for analog optical communications. The reason is for digital communications the objective was the recovery of data bits, while in analog communication the objective is the recovery of continuous waveforms, which can now be severely degraded by nonlinear distortion.

The nonlinearity issue in RoF mainly arises from the optical modulator and chromatic dispersion in the SMF. Figure 1.14 shows the normalized power transfer function for the two popular external electro-optical modulators, i.e. the electro-absorption and Mach-Zehnder modulator.

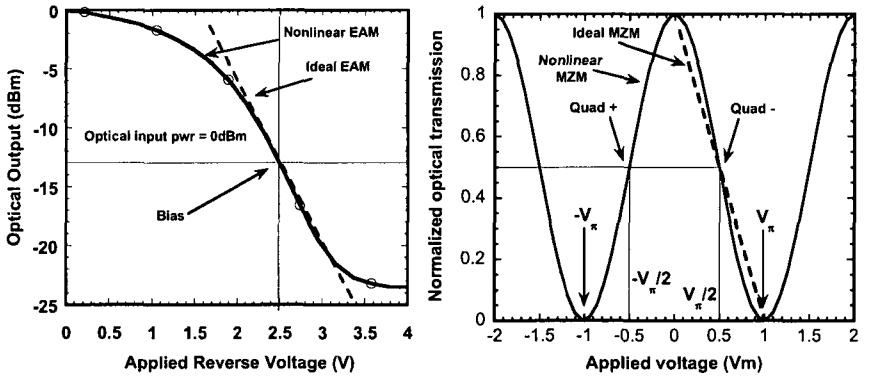

(a) (b)

Figure 1.14 Normalized optical transmission versus applied voltage for the (a) electro-absorption and (b) Mach-Zehnder modulator.

The electro-absorption modulator shown in Fig. 1.14(a) exhibits second and third nonlinearities depending on the device's DC biasing, because of the exponential optical power output transfer function shown (1.1). But it is possible to bias the device so that either second or third order nulls are obtained, which will shown in Chapter 2.

$$P_{out}(v(t)) = P_{in}e^{-f(V(t))}, \tag{1.1}$$

P_{in} is the average constant wave laser input power, $f(\ )$ is the transfer characteristic of the EAM, $V(t) = V_b + v(t)$ is the applied DC bias and the modulating signal voltage or applied reverse voltage. Using the Taylor series expansion for exponentials on (1.1), the following is obtained

$$P_{out}(v(t)) = P_{in}\left[1 - f\left(V(t)\right) + \frac{f^2\left(V(t)\right)}{2!} - \frac{f^3\left(V(t)\right)}{3!} + \ldots\right], \tag{1.2}$$

where it is seen from (1.2) that both second and third order nonlinearities are present.

In the case of the Mach-Zehnder modulator, the transfer function is seen in Fig. 1.14(b), where unlike the electro-absorption modulator this device has only a second order distortion null provided the device's biasing is set to quadrature, this will be shown later in this section. Also noted from Fig. 1.14(b) is that the linearity improves if the modulation index is small, but this will also give rise to a smaller carrier to noise ratio, which will degrade the overall RoF system performance [5]. The output optical electric field is defined below,

$$E_{out}(v_{m1}, v_{m2}) = E_{in}e^{-j\omega t}\left[e^{-j\frac{\pi}{V_\pi}(V_1 f(v_{m1}) + v_{b1})} + e^{-j\frac{\pi}{V_\pi}(V_2 f(v_{m2}) + v_{b2})}\right] \tag{1.3}$$

where E_{in} is the average electric field injected into the dual electrode Mach-Zehnder modulator, V_1 and V_2 are the modulating signal amplitudes, $f(\ )$ modulating signal, v_m is the modulating signal voltage and v_b is the applied DC bias. The optical power output is represented by,

$$P_{out}(v_{m1}, v_{m2}) = E_{out}(v_{m1}, v_{m2}) * E^*_{out}(v_{m1}, v_{m2})$$

$$= P_{in,ave} \cos^2\left[\frac{\pi}{2V_\pi}\left(V_1 f(v_{m1}) - V_2 f(v_{m2}) + v_{b1} - v_{b2}\right)\right] \tag{1.4}$$

and by setting the Mach-Zehnder modulator to a quadrature bias, a second order nonlinearity null will be induced. By defining the following parameters as $V_1 = V_2 = V_0$, $f(v_{m2}) = -f(v_{m1}) = f(v_m)$, $v_{b2} = -v_{b1} = \frac{V_\pi}{2}$ and defining the modulation index as $m = \frac{\pi V_0}{V_\pi}$, the optical power transfer function is obtained for the dual electrode Mach-Zehnder modulator as,

$$P_{out}(v_m) = P_{in}\left[1 + \sin\left(\frac{\pi}{2V_\pi}\left(2V_0 f(v_m) + V_\pi\right)\right)\right] = P_{in}\left[1 + \sin\left(mf(v_m)\right)\right]. \tag{1.5}$$

Using the Taylor series expansion on (1.5) the following expression (1.6) is obtained and it is seen that only odd order distortion exists, along with the DC and fundamental components. Unfortunately, because of chromatic dispersion in SMF, second order distortion will reemerge due to optical beating between the optical carrier and third order distortion.

$$P_{out}(v_m) \approx P_{in,ave}\left[1 + mf(v_m) - \frac{m^3 f^3(v_m)}{3!} + \frac{m^5 f^5(v_m)}{5!} - \ldots\right] \tag{1.6}$$

In order to measure this nonlinearity in an analog fiber link, a two tone (Ω_1, Ω_2) distortion measurement is commonly used. The nonlinearities are in the form of harmonic distortion (HD) and intermodulation distortion (IMD). Generally, second and third order harmonic and intermodulation products are of the most concern in analog access systems, because higher order terms usually have smaller amplitudes or usually lie outside the composite signal passband. Second and third order harmonic distortions will be generated due to the optical subcarrier and occur at $2\Omega_1$ and $3\Omega_2$. Second order IMD is also generated in the sum and subtraction of the optical subcarrier frequencies in the channel passband, i.e. $(\Omega_1 \pm \Omega_2)$. Due to third order IMD (3IMD), spurious subcarriers at ($2\Omega_1 \pm \Omega_2$), $(\Omega_1 \pm 2\Omega_2)$ are also generated, falling within the channel passband.

For the simulated optical spectrum in Fig. 1.15 the tones are set to 10 and 12 GHz and the Mach-Zehnder modulator was set to transmission zero, which will allow the second order distortion to be seen. Furthermore, a 0 dBm CW laser with a wavelength of 1553nm was used. All simulations in this thesis was done with a commercially available software packaged from VPI Photonics Inc called © VPI Transmission Maker 7.6, where it will be described in Section 1.7. It is seen that the 3IMD frequency components at 8 and 14 GHz are relatively close to optical subcarriers and are most detrimental to the RoF system.

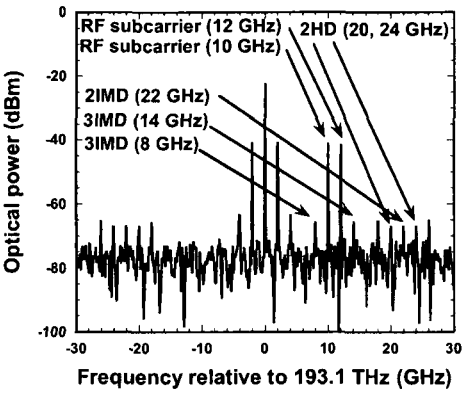

Figure 1.15 Simulated optical spectrum of a dual electrode Mach-Zehnder modulator with tones set to 10 and 12 GHz.

1.7 VPI Transmission Maker Simulation Tool Described

VPI Transmission maker is a sampling based optical simulation tool developed by VPI Photonics Inc. The simulation tool is composed of components, e.g. laser, optical modulator, fiber, wavelength multiplexers/demultiplexers and photodetectors that are placed on a worksheet in the desired configuration and independently configured with parameters to model true off the shelf components and components being tested before fabrication. Some of the adjustable parameters include thermal noise, shot noise, dispersion, etc. The samples may be processed by each component in the design by independent samples or blocks of samples. The sample window may be adjust according to allow for greater resolution at the expense of extra processing time. Included in the simulation package are visualizers, such as universal bit error rate analyzers, optical spectrum analyzers, electrical spectrum analyzers, oscilliscopes etc. Design parameters may be swept dynamical to study the performance and stability of a design. The

simulation tool has the ability to track transit time and custom variables. The package has the ability to run co-simulations with such 3rd party packages as © Matlab and © Python [32].

1.8 Motivation and Research Problem

The objective is to look at the linearization problem as a whole and to develop linearization techniques that address the performance of the entire RoF system. The designs should not only linearize the optical modulator, but also the fiber and receiver. The RoF systems should make use of optical single sideband transmission, so that nonlinear distortion induced by chromatic dispersion in the single mode fiber and power fading is minimized, which will be explained in Chapter 2. This will also make the RoF system spectrally efficient and economical. Furthermore, the proposed designs will only make use of external optical modulators, so that frequency chirp and clipping are not an issue.

1.9 Scope and Organization of the Thesis

The objective of this research work is to develop new linearization modulators or systems that improve upon existing ones, so as to help make RoF systems an economical alternative to existing wireless, broadband and passive optical networks. Based on this research, four proposed linearization techniques are developed and exhaustively investigated for performance verification. The final presented linearized modulator will

also be experimentally verified with the possibility of a complete modular design being kept for future work. This thesis is organized as follows.

The first chapter of the thesis has provided the reader with a background history of broadband networks being used today and explained the motivation for the research topic. The nonlinearity issue and how it affects the future of wireless broadband services has been described. This was accomplished by providing an example of the cable company's broadband solution and an explanation for the reason that it is required to have a lower distortion transmission. Also discussed are the differences between RoF and the popular DWDM being used today along with the cost advantages of RoF technology.

Chapter 2 will discuss the optical power fading issue and provide the theory for the phenomenon. The chapter will also discuss the principle of optical single sideband (OSSB) generation using the Hilbert transform and provide the mathematical formulations for it. Also introduced will be currently used and previously proposed linearization techniques. Some linearization techniques presented will be; the dual wavelength balanced RoF system, dual-parallel MZM, bidirectional MZM and the mixed-polarization phase MZM. Each will be proven to function mathematically, along with an explanation of their advantages and disadvantages.

Chapter 3 will introduce the proposed single wavelength balanced RoF system, which outperforms the dual-wavelength balanced RoF due to the fact that only one fiber and wavelength are used, so it will not be greatly affected by chromatic dispersion as in previous designs. The performance of the proposed design will be compared to the conventional balanced system (dual wavelength balanced RoF system) and conventional EAM system (no linearization used) through simulations, which will show greater second

order distortion suppression and bit error rate (BER) performance. Of course, it is well known that balanced systems may only suppress second order nonlinear distortion and common mode relative intensity noise, so this was the motivation that lead to the design of the tunable FBG balanced RoF system, which is able to suppress second and third order nonlinear distortion.

Chapter 4 introduces the proposed tunable FBG balanced RoF system, which is capable of suppressing both second and third order nonlinear distortion with the use of only one optical modulator and a tunable nonlinearly chirped fiber Bragg grating. It will be compared through simulation to the conventional RoF, through distortion suppression and BER results. Because third order distortion lies in close proximity to the optical RF signal subcarriers and are most detrimental, this is the motivational reason that leads to the final two proposed techniques, which will be presented in Chapters 5 and 6.

Chapter 5 describes the proposed asymmetric OSSB MZM, which makes use of the dual-parallel linearization method, but using only one optical modulator. Furthermore, OSSB can be generated as well as suppressing third order nonlinear distortion. The theoretical development for the expression of spurious free dynamic range is included for this design. The proposed technique is compared to the dual-parallel MZM in spurious free dynamic range. Also shown is the sensitivity analysis to variations in voltage splitting ratio and differential phase delay between the two coupled branches.

Chapter 6 describes the proposed mixed-polarization MZM, which again also makes use of one optical modulator and optical single sideband modulation. The technique is greatly adapted for modular implementation, because of its simplicity. In this case, simulation and experimental results are shown that prove the performance improvement

over the nonlinearized optical modulator in spurious free dynamic range. Also again the theoretical development for the expression of spurious dynamic range is included along with the sensitivity analysis to a dimensionless modulation index ratio and polarization angle deviations from the optimal.

Chapter 7 will conclude the thesis with the amount of progress that was accomplished and potential implication to knowledge, theory and practice. Also discussed is future work that remains and over all insights.

Chapter 2

2 Background Theory and Linearization Techniques Reviewed

2.1 Introduction

The objective of this chapter is to provide a brief introduction to optical power fading phenomena, optical single sideband generation and previously proposed linearization techniques, so that the readers may become familiarized, so as to follow the remainder of the thesis. The linearization techniques that will be discussed will be described with examples from published literature. This will aid in the understanding of the proposed linearization techniques.

The chapter will be organized as follows; in Section 2.2 RF power fading phenomenon will be explained and shown mathematically, Section 2.3 will cover the generation of optical single sideband modulation using the Hilbert transform and the general implementation will be shown, Section 2.4 will provide a literature review of accomplished works in linearization techniques that are being used today along with their drawbacks, this material is relevant to the proposed linearization techniques presented in this thesis and finally Section 2.5 will provide concluding remarks.

2.2 RF Carrier Power Fading

It is well known that optical single sideband (OSSB) is not degraded by RF power fading when transmitted through dispersive fiber, while optical double sideband (ODSB) will experience periodic power fading that is dependent on fiber length, chromatic dispersion and RF carrier [33]. The power fades occur because of the use of SCM, which generates two optical sidebands that are at different frequencies and experience different propagation delays through dispersive fiber. This propagation delay will translate into a differential phase shift ($\Delta\phi$) between the two sidebands. When $\Delta\phi=(2n+1)\pi$, n = 0,1,... then destructive interference occurs and the RF signal is completely cancelled at the receiver. The propagation delay (ΔT) between the two sidebands is given by, $\Delta T = LD\Delta\lambda = LD\left(\frac{\lambda\Delta f}{f_\lambda}\right) = LDc\left(\frac{\Delta f}{f_\lambda^2}\right)$, where L is the fiber length, D is the chromatic dispersion of the fiber, c is the speed of light in a vacuum, f_λ is the optical frequency and Δf is the RF carrier frequency. At $\frac{\Delta T}{2}$ i.e. a half period delay, fading occurs because the two sidebands will be π radians out of phase from each another, so the above expression now becomes, $\Delta\phi = \Delta\omega\frac{\Delta T}{2} = \pi\Delta f\Delta T = \frac{\pi cLD}{2}\left(\frac{\Delta f}{f_\lambda}\right)^2$ and sideband cancellation occurs at periodic phase intervals, $\Delta\phi=(2n+1)\pi$, which leads to $(2n+1)\pi = \frac{\pi cLD}{2}\left(\frac{\Delta f}{f_\lambda}\right)^2$ and solving for fiber length, $L=\frac{(2n+1)}{2cD}\left(\frac{f_\lambda}{\Delta f}\right)^2$. If the latter is

written more descriptively, one obtains $L_{Period} = \frac{(2n+1)}{2cD}\left(\frac{f_\lambda}{\Delta f}\right)^2$, where L_{Period} is the periodic fiber fade length.

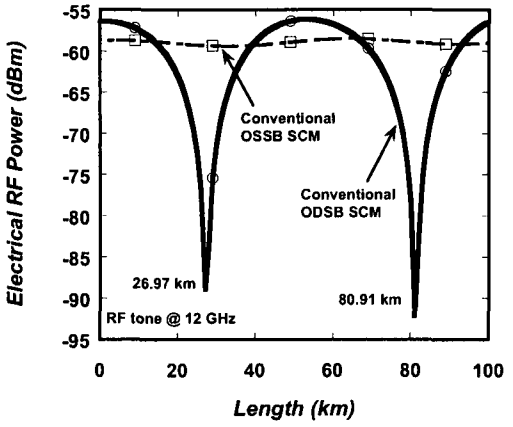

Figure 2.1 Simulated received RF power versus fiber length for a conventional OSSB and ODSB SCM transmissions with RF tone at 12 GHz, through 100 km of 16 $ps/(nm \cdot km)$ SMF. Here the fiber attenuation has been compensated.

Figure 2.1 shows the simulated RF power received at the photodiode for a conventional RoF system using ODSB and OSSB modulation, where the RF carrier is set to a frequency of 12 GHz and fiber attenuation is compensated. In the case of OSSB modulation there is almost no RF carrier power fade, but in the ODSB case there are two RF carrier power fades occurring at 26.97 and 80.91 km of the 100 km fiber length. This RF carrier power fade lengths would vary in time according to environmental conditions, such as heating, which will expand or contract the fiber line.

2.3 Optical Single Sideband Subcarrier Modulation

Before presenting the OSSB SCM, it would be beneficial to show the optical spectrum of an ODSB and OSSB modulation. A simple simulation was carried out, where a Mach-Zehnder modulator was fed with a 0 dBm CW laser light set to a wavelength of 1553 nm and 30 dBm sinusoidal RF signals with frequency set to 10 GHz. The simulated optical spectra using ODSB and OSSB are measured from the output of the Mach-Zehnder modulator and are shown in Figs. 2.2(a) and 2.2(b), respectively. In the ODSB case shown in Fig. 2.2(a) both optical RF signal subcarriers appear before and after the optical carrier, with a frequency separation of 20 GHz, while in Fig. 2.2(b) only the upper optical subcarrier appears after the optical carrier. In this case the simulation was setup up using the Hilbert transform as shown in Fig. 2.3, which will be further explained in this section. Note, in Fig. 2.2(b) the lower optical sideband is not completely suppressed, because of the finite extinction ratio of 35 dB for the Mach-Zehnder modulator.

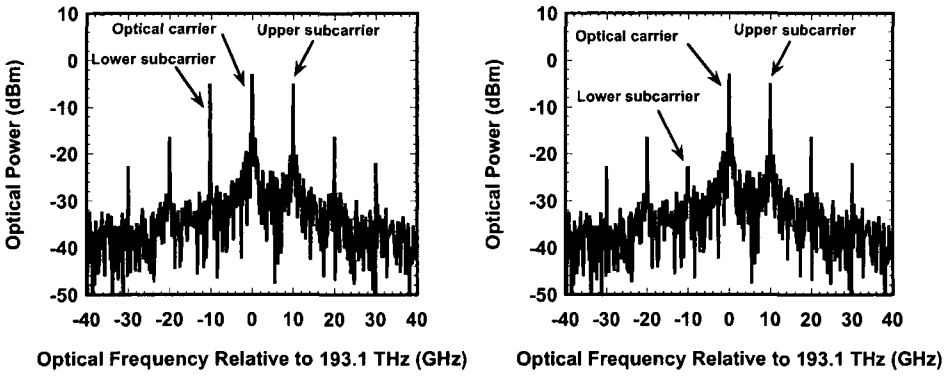

(a) (b)

Figure 2.2 Simulated optical spectra for a Mach-Zehnder modulator fed with a 30 dBm, 10 GHz sinusoidal RF signal (a) in a conventional (ODSB) and (b) a Hilbert transform (OSSB) configuration. The input 0 dBm CW laser light wavelength was set to 1553 nm.

Optical single sideband SCM was first proposed in [7] and the block diagram is seen in Fig. 2.3(a) and if implemented using a dual electrode Mach-Zehnder modulator, then it is represented by Fig. 2.3(b).

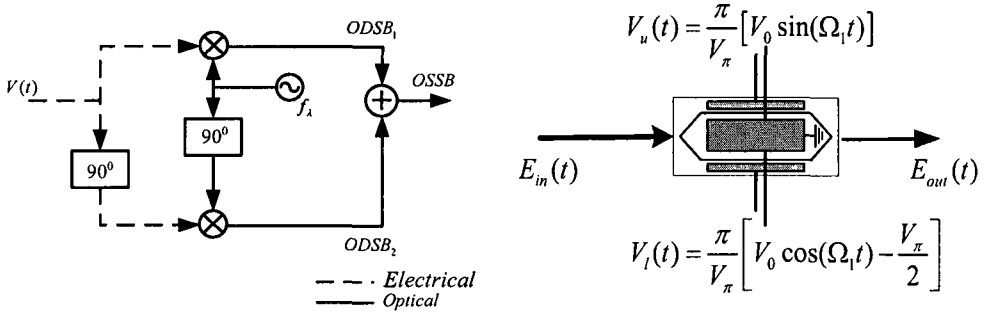

(a) (b)

Figure 2.3 Block diagram for the OSSB SCM (a) using the Hilbert transform and its implementation with (b) the Mach-Zehnder modulator.

It would be best to explain the OSSB SCM mathematically, if the modulation index is represented by $m = \frac{\pi V_0}{V_\pi}$, then the electric field exiting the Mach-Zehnder modulator is represented by

$$E_{out}(t) = \frac{E_{in}}{\sqrt{2}}\left(e^{jm\sin(\Omega t)} + e^{j\left(m\cos(\Omega t) - \frac{\pi}{2}\right)} \right) e^{j\omega t}, \tag{2.1}$$

where E_{in} is the input electric field, Ω is the RF carrier angular frequency and ω is the optical carrier angular frequency. Using the Jacobi-Auger expansions,

$e^{jx\sin(\Omega t)} = \sum_{n=-\infty}^{\infty} J_n(x)e^{jn\Omega t}$ and $e^{jx\cos(\Omega t)} = \sum_{n=-\infty}^{\infty} j^n J_n(x)e^{jn\Omega t}$ on (2.1) the expression can be approximately written using Bessel function of the first kind as,

$$\begin{aligned} E_{out}(t) &\approx \frac{E_{in}}{2}\left(2J_0(m) + \left[J_1(m) + J_1(m)\right]e^{j\Omega t} + \left[-J_1(m) + J_1(m)\right]e^{-j\Omega t} + \ldots\right)e^{j\omega t} \\ &= \frac{E_{in}}{2}\left(2J_0(m) + 2J_1(m)e^{j\Omega t} + \ldots\right)e^{j\omega t} \end{aligned} \tag{2.2}$$

Analyzing (2.2) only up to the first order, it is seen that the first term in the bracket represents the optical carrier of the exiting electric field and the second term represents the upper optical subcarrier and lower optical subcarrier is cancelled, so OSSB is obtained. This principle will be incorporated in the last two proposed designs presented in Chapters 5 and Chapter 6 as a complete linearization solution.

2.4 Linearization Techniques Reviewed

2.4.1 Literature Survey of Techniques for Nonlinear Distortion Suppression

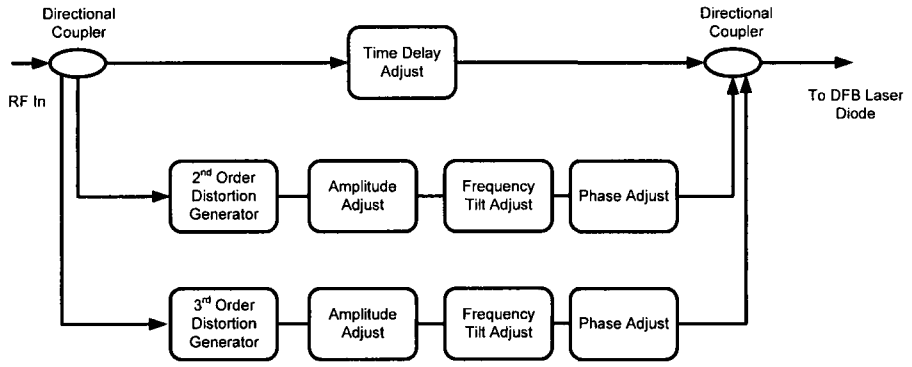

Figure 2.4 Electrical block diagram for the pre-distortion circuit that minimizes the effects of 2nd and 3rd order nonlinear distortions for DFB laser transmitters [34].

To meet the minimum picture quality requirement, cable companies implement a variety of pre-distortion, feed-forward and distortion cancellation circuits. Nonlinear distortion generated by the semiconductor laser is often too high to meet the CATV network CNR requirements. Therefore, cable companies employ pre-distortion circuits before the DM-DFB lasers to suppress second and third order nonlinear distortions [34-38], which is shown in Fig. 2.4. The input RF signal is split into three paths before feeding the DFB laser diode, where the first is delayed in order to compensate for delays through the secondary paths. The pre-distortion circuit in the secondary path generates second and third order distortions with equal amplitude, but with opposite phases at that operating point. This will have the effect of making the output laser power linear as shown in Fig. 2.5, where the RF input signal is passed through an arcsine pre-distortion circuit before

feeding the optical modulator [39]. This technique operates well when the nonlinear distortions are static, but when the distortion is dynamic a feedback system is required to change the characteristics of the arcsine pre-distortion circuit.

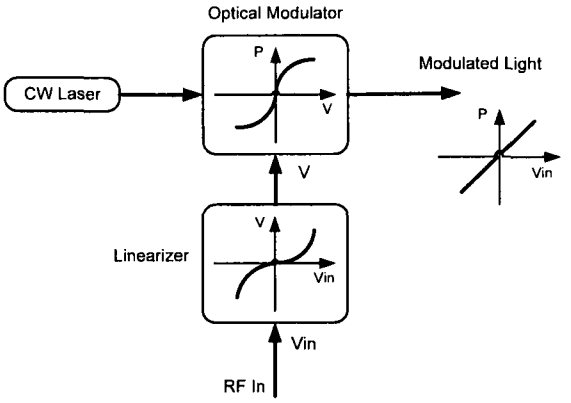

Figure 2.5 Operation principles for the electronic pre-distortion linearization method [34-38].

Feed-forward linearization method is yet another technique used by cable companies to achieve the required CNR, which is shown in Fig. 2.6. One may see from the figure that because the linearization method attempts to compensate for nonlinearity dynamically, it is much more complicated than the pre-distortion method. Referring to Fig. 2.6 below, the RF signal is split before the modulator and delayed and amplified relative to the applied RF signal. A small fraction of the output power of each arm of the MZM is split and detected using a photodiode. The RF error signal, which is generated by comparing the delayed and the photodetected RF signals with the use of a broadband 180^0 RF hybrid comparator, is applied to an auxiliary DFB laser. The DFB laser must be tuned close to the source, but not allowed to have the same wavelength in order to prevent coherent interference. The output of both auxiliary DFB laser must be combined with a balanced bridge interferometer (BBI) modulator in order to cancel the nonlinear

distortions. To properly compensate for the modulator nonlinearity, the feed-forward linearization method requires flattening and gain matching at the auxiliary photodiode, DFB laser and driving circuitry. Also when combining two optical signals with different wavelengths, a differential time delay is generated because of chromatic dispersion that needs to be compensated for proper operation [40, 41].

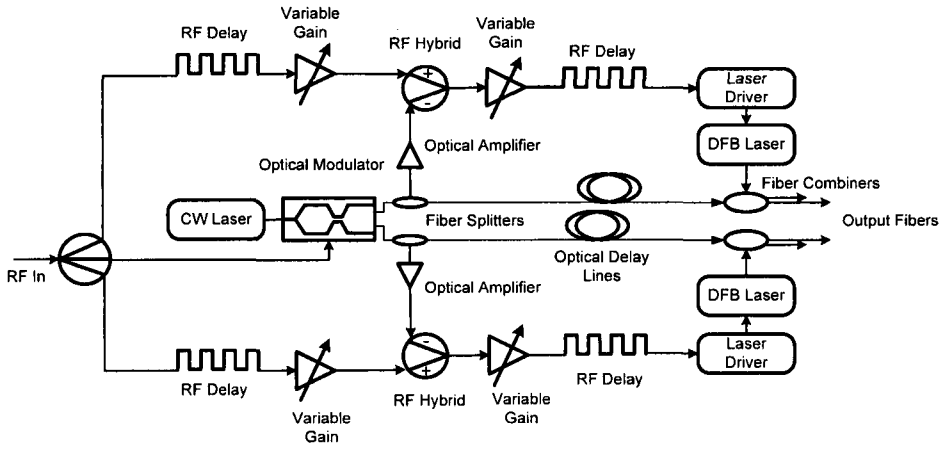

Figure 2.6 Block diagram for the feed-forward linearization method with the balanced bridge interferometer modulator [42, 43].

The two previous techniques, the pre-distortion and feed-forward only combat the nonlinear distortion problem electrically, by referring to or manipulating the input RF signal. Optical dual-parallel and dual-cascade linearization methods are two cancellation methods that combat the nonlinear distortion optically. The dual-parallel MZM linearization method is schematically shown in Fig. 2.7, where the top (primary) and bottom (secondary) Mach-Zehnder interferometer (MZI) modulators are biased 180^0 out of phase at the operating point. When the two emitted optical signals are combined at the output, third order distortion is cancelled [44]. Because the optical power ratio between

the two MZI modulators must be accurately maintained for satisfactory performance and with the use of two MZI modulators makes this method expensive and impractical.

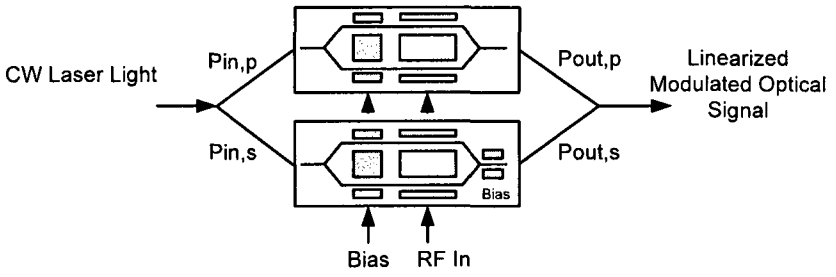

Figure 2.7 Dual-parallel linearized MZI [44, 45].

The optical dual-cascaded MZI linearization method also makes use of two MZI modulators and is seen in Fig. 2.8. The two cascade MZI modulators are fed by the same RF signal but phase shift from each other by 58^0 to 65^0 and biased independently. This method can cancel second and third order nonlinear harmonic distortions [46]. The two main disadvantages for this linearization method is first that asymmetric losses between the upper and lower branches of each of the directional couplers make it difficult to obtain the same linearization for both optical outputs simultaneously compared with a single optimized output. As a consequence only one linearized optical output is typically being implemented. Secondly, this method has double the insertion loss compared to a single linearized stage modulator, which can limit the maximum optical output power.

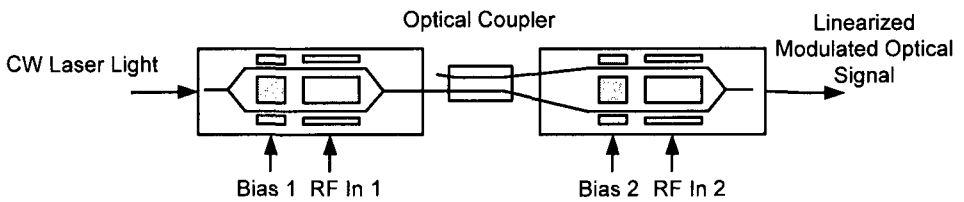

Figure 2.8 Dual-cascaded linearized MZM [46].

2.4.2 Electrical Balanced Receivers Used in Practice

The balanced or push-pull receivers are grouped with the distortion cancellation methods and are only able to cancel second order distortions. Figure 2.9 shows a typical block diagram of a cable TV receiver using a balanced preamplifier, which is generally used in today's OTUs. The balanced preamplifier is not only capable of suppressing second order nonlinear distortion, but also common mode RIN as well, thereby improving CNR.

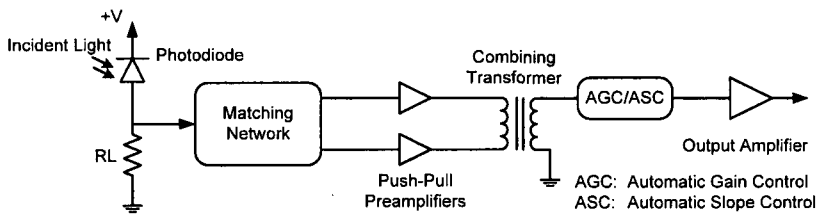

Figure 2.9 Simplified block diagram of a CATV receiver using push-pull preamplifiers.

The configuration works as follows, by referring to (2.3), which provides the matching network branch voltage, where fourth and higher order distortions are neglected and the voltages are 180^0 out of phase from each other, namely $V_2^{out} = -V_1^{out}$. When the branch voltages are combined all second order products subtract and odd order products add to result in just the transmitted signal $2b_1V_{1,in}$. Because this scheme cancels second order distortion electrically, there is the disadvantage of increase layout, multiple power supply voltages, bandwidth limitations and circuit complexity [47, 48].

$$V_1^{out} = b_1V_{1,in} + b_2V_1^2{}_{,in} + OV_1^3{}_{,in}$$

$$V_2^{out} = -b_1V_{1,in} + b_2V_1^2{}_{,in} - OV_1^3{}_{,in} \qquad (2.3)$$

In order to reduce cost and circuit complexity of the OTU, other optical balanced links have been devised and function using the same methodology. These optical balanced systems use two optical modulators and photodetectors. The two optical

modulators transmit two RF signals that are 180^0 out of phase from each other and they are received by two photodetectors, and the received signals are subtracted. The balanced systems may use one wavelength and two fibers [49-56], two wavelengths and one fiber [57] and the newly proposed balanced system that uses one wavelength and fiber [58].

2.4.3 Dual Fiber Balanced Receiver

The balanced system that makes use of one wavelength and two fibers in Fig. 2.10 per channel, does simplify the OTU circuit complexity, but at the expense of increasing costs for the MHE and fiber distribution network (video trunking system) [53, 54]. This is currently being used by cable companies today. The cost increase is due to the fact that two fibers and complex control methods are used to maintain balance between the two transmission paths. The main issue with this method is that because two independent fibers are used then it becomes difficult to maintain power and phase alignment in the two optical transmission paths due to chromatic dispersion and different fiber lengths. Also because ODSB is used the transmission will experience power fading at periodic fiber lengths, which will require an automatic gain control at the receiver and more cost for the RoF system.

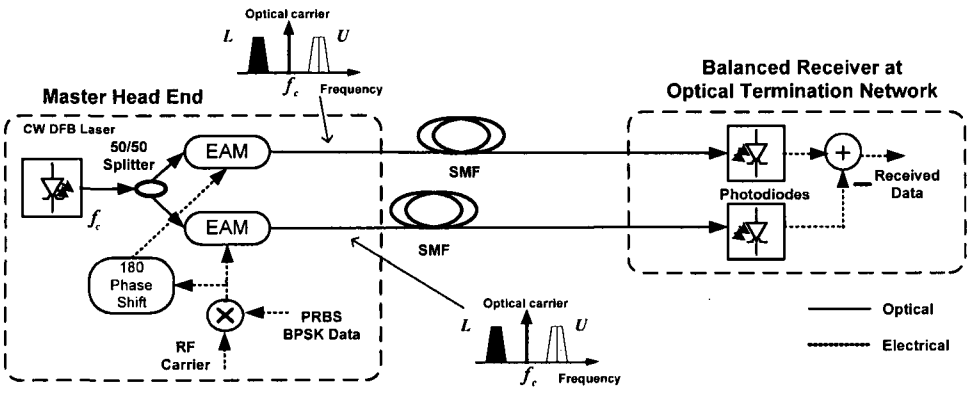

Figure 2.10 Single wavelength dual fiber balanced system [53, 54].

2.4.4 Dual Wavelength Balanced RoF System

Balanced RoF systems are only capable of cancelling second order distortion, which will be proven mathematically further in this section. The dual wavelength balanced (conventional balanced) RoF system has further improved performance over the dual fiber balanced RoF system presented in Section 2.4.3, by using two wavelengths and one fiber per channel as seen in Fig. 2.11. In this case phase and power matching are improved, but still difficult to maintain. The reason is that two wavelengths with fiber dispersion will experience different propagation delays for each wavelength and the system's ability to cancel out second order distortion is degraded. Furthermore, the technique uses ODSB modulation, which is not spectrally efficient and because of the two wavelengths it will experience power fading at the receiver. This technique will also require an automatic gain control to stabilize power fluctuations at the receiver, which will incur added system expense.

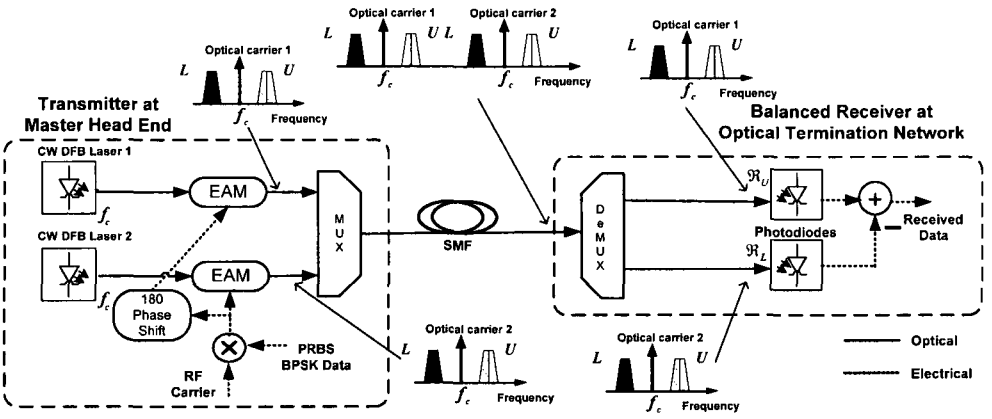

Figure 2.11 Dual wavelength single fiber balanced RoF system (conventional balanced RoF system) [57].

As seen in Fig. 2.11, there are two lasers used and each is connected to their respective EAM. Both EAMs are driven by the same RF signal, but the lower EAM's applied RF signal is 180^0 phase shifted from the one applied to the upper EAM. Then the output modulated lights are combined with an optical multiplexer. After fiber transmission two optical carriers with their optical subcarriers are separated using an optical demultiplexer. Then each of the two optical carriers and its optical subcarriers are fed to separate photodetectors. The two generated photocurrents are combined together, so that the RF carriers are added and second-order distortion is cancelled.

The theoretical analysis for the balanced system will be considered, by first presenting the optical power transfer characteristic of the EAM as a polynomial by defining the output electric field, $E_{out}(t)$ to the input electric field, E_{in} as,

$$E_{out}(t) = T(V(t))E_{in}, \tag{2.4}$$

where $T(V(t)) = |T(V(t))| e^{j\phi_{Radians}(V(t))}$ is the complex field amplitude transfer function that is different for each manufactured EAM and dependent on the applied electric field or RF signal, $V(t)$. The optical output power is represented by

$$P_{out}(t) = T(V(t))E_{in} \times T(V(t))E_{in}^{*} = |T(V(t))|^2 P_{in} \tag{2.5}$$

The optical power transfer may be represented in magnitude by $|T(V(t))|^2 = T_0 + T_1 V(t) + T_2 V^2(t) + T_3 V^3(t) + \ldots$, where T_i, $i = 0,1,2\ldots$ are the magnitude transmission polynomial coefficients or in decibel $T_{dBm}(t) = 10\log(|T(V(t))|^2)$, which leads to the following expression

$$T_{dBm}(V(t)) = T_{dBm,0} + T_{dBm,1} V(t) + T_{dBm,2} V^2(t) + T_{dBm,3} V^3(t) + \ldots \tag{2.6}$$

Therefore the upper and lower received photocurrents as shown in Fig. 2.11 are represented by $I_{Upper}(t) = \frac{1}{2}\Re_U \left[T_0 + T_1 V(t) + T_2 V^2(t) + T_3 V^3(t) + \ldots \right]$ and $I_{Lower}(t) = \frac{1}{2}\Re_L \left[T_0 - T_1 V(t, \Delta\phi) + T_2 V^2(t, \Delta\phi) - T_3 V^3(t, \Delta\phi) + \ldots \right]$, where $\Re_U$ and $\Re_L$ are the responsitivity for the upper and lower photodiodes, respectively, $\Delta\phi$ is the electrical phase difference between the upper and lower photodiodes and $V(t)$ is the desired RF signal, i.e. $V(t) = V_0 \sin(\Omega t - \Delta\phi)$. Finally, the received signal is represented by

$$I(t) = I_{Upper}(t) - I_{Lower}(t) = \frac{1}{2}\begin{Bmatrix} \Re_U \left[T_0 + T_1 V(t) + T_2 V^2(t) + T_3 V^3(t) + \ldots \right] - \\ \Re_L \left[T_0 - T_1 V(t, \Delta\phi) + T_2 V^2(t, \Delta\phi) - T_3 V^3(t, \Delta\phi) + \ldots \right] \end{Bmatrix}. \tag{2.7}$$

Assume the responsitivity $\Re_U = \Re_L = \Re$ and $\Delta\phi = 0$, thus the following expression for the received photocurrent is obtained, $I(t) = \Re\left\{ T_1 V(t) + T_3 V^3(t) + T_5 V^5(t) \ldots \right\}$. Note, only

the desired RF signal and odd order nonlinear distortions remain. In other words, the second or even order nonlinear distortions are removed. However, the third or odd order distortions still exist. In order to have both odd and even order distortions removed, it is required to bias the EAM in a third order null to suppress third order distortion, making the system linearized.

The analysis above has neglected to consider the phase of the optical signal at the output of the EAM, which leads to phase modulation. This is an undesirable effect that leads to chirp of the optical output signal and is characterized by the alpha factor. The optical phase with respect to the modulating voltage is represented by

$$\phi_{Radians}(V(t)) = \frac{\ln(10)}{20}\int_0^{V(t)} \alpha(V(t))\frac{dT_{dBm}(V(t))}{dV}dV \quad \text{or}$$

$\phi_{Radians}(V(t)) = \frac{2\pi}{360}\left(\phi_0 + \phi_1 V(t) + \phi_2 V^2(t) + \phi_3 V^3(t) + ...\right)$, where α is the alpha factor, which depends on the modulating voltage $V(t)$ and ϕ_i, $i = 0,1,2...$ are the phase polynomial coefficients [59, 60]. If the alpha factor α is not greatly dependent on modulating voltage, which is what was considered in the above analysis, then it can be represented by a constant. The performance sensitivity of the balanced RoF system is mainly dependent on the phase difference between two transmitted data signals and not the individual phases. The reason for this is that the balanced photodetector uses square-law detection and cannot discriminate phase information.

2.4.5 Dual-Parallel MZM Linearization Technique

The dual-parallel MZM linearization technique is shown in Fig. 2.12 and basically functions by summing the upper and lower modulated lights emitted by the two Mach-

Zehnder modulators. If the upper and lower Mach-Zehnder modulator were driven by the same RF signal, but phase shifted by π radians, then the transmitted optical subcarriers would be completely cancelled. For this case if the lower Mach-Zehnder modulator was driven with more RF power, as compared to the upper modulator, then the lower modulator would generate more third order distortion and the upper would generate less third order distortion. As a result, greater RF power will result in greater modulation depth, which will lead to increased optical subcarrier power.

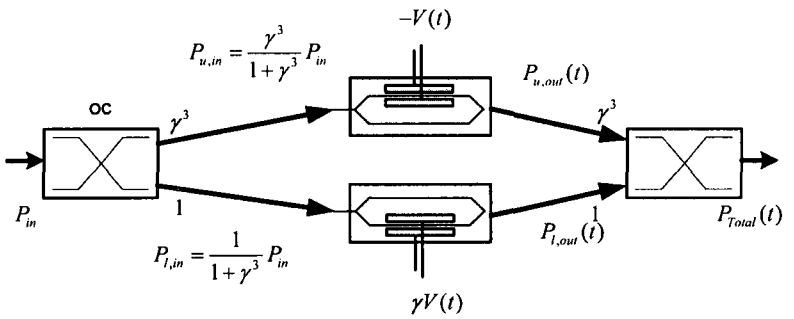

Figure 2.12 Dual-parallel Mach-Zehnder linearization modulator [44].

The two parallel MZMs are connected by an asymmetrical optical splitter and combiner. The splitter and combiner have an optical power splitting/combining ratio of γ^3 : 1. The two MZMs are driven in push-pull with driving voltage set to $-V(t)$ and $\gamma V(t)$ for the upper and lower MZM, respectively. The modulated optical output power for the upper and lower Mach-Zehnder modulators are represented by,

$$P_{u,out}(t) = P_{u,in}\left[1-\sin\left(\frac{\pi V_0 V(t)}{V_\pi}\right)\right] \tag{2.8}$$

and

$$P_{l,out}(t) = P_{l,in}\left[1+\sin\left(\frac{\pi V_0 \gamma V(t)}{V_\pi}\right)\right], \tag{2.9}$$

respectively, where $P_{u,in}$ and $P_{l,in}$ are the input optical power for the upper and lower Mach-Zehnder modulators, V_0 is the voltage amplitude of the RF signal, $V(t)$ is the RF modulating signal voltage and V_π is the half wave switching voltage of the Mach-Zehnder modulator. If the Talyor series expansion is used, and (2.8) and (2.9) are added together, then total modulated optical power is obtained as,

$$P_{Total}(t) = P_{u,in}\left[1-mV(t)+\frac{(mV(t))^3}{3!}-\ldots\right]+P_{l,in}\left[1+m\gamma V(t)-\frac{(m\gamma V(t))^3}{3!}-\ldots\right]. \tag{2.10}$$

The condition for third order distortion cancellation becomes $P_{u,in}-\gamma^3 P_{l,in}=0$ or $\frac{P_{u,in}}{P_{l,in}}=\gamma^3$. Also it is seen that there is a cancellation of some RF signal power by a factor of $\frac{\gamma(\gamma-1)}{1-\gamma+\gamma^2}$ [44]. In other words, the unequal distortion created by one optical modulator is optically coupled to cancel the distortion created by the other. Because the dual-parallel MZM linearization requires the use of two optical modulators, each with its unique optical frequency response and separate optical travel paths, it may be difficult in practice to optically combine them to achieve satisfactory linearization performance.

2.4.6 Bidirectional MZM Linearization Technique

The bidirectional linearization technique is based on the dual-parallel MZM linearization technique, but makes use of only one optical MZM, thereby offering a possible solution in the practical implementation of the dual-parallel MZM linearization technique [61, 62]. The bidirectional MZM linearization technique is shown in Fig. 2.13.

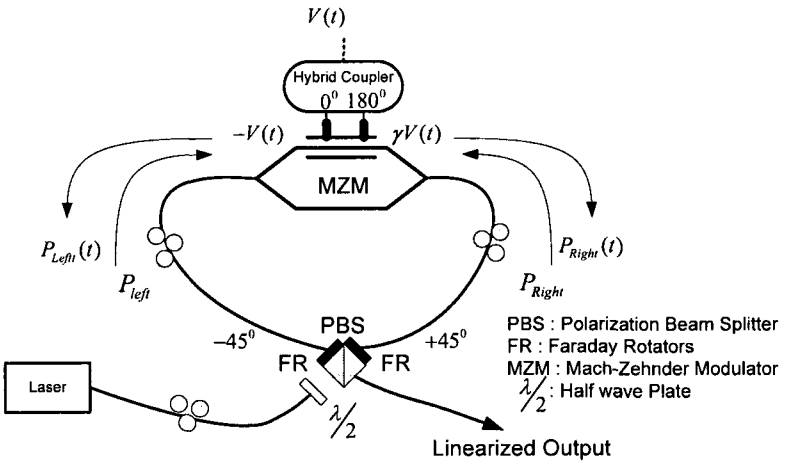

Figure 2.13 Bidirectional Mach-Zehnder linearization modulator [61].

The bidirectional MZM technique is comprised of one standard Mach-Zehnder modulator with electrodes that are not internally terminated, hybrid RF coupler, two oppositely oriented 45^0 Faraday rotators (FR) and a polarization beam splitter (PBS). The CW light is fed into a half wave plate that rotates the light by a given angle, before being fed to the polarization beam splitter, which breaks the light into p- and s- orthogonally polarized lights. The two oppositely oriented 45^0 Faraday rotators rotate the output lights so that they enter the polarization maintaining fibers (PMF) at -45^0 and 45^0, respectively. The optical signals now bidirectionally feed the Mach-Zehnder modulator, where a RF signal is provided through a 180^0 hybrid coupler, which not only provides a 180^0 phase

shift between the two RF signals, but also an amplitude difference of γ. This allows one branch to carry greater optical power than the other due to the angle set by the half wave plate. Because there is weak coupling to the counter propagating wave for RF of greater than 2 GHz, crosstalk between the two counter propagating optical signals is not considered. Now each PMF branch will carry the same optically modulated signal with a phase shift of 180^0, but with different RF carrier power and third order distortion. The signals are then optically combined through the PBS to cancel third order nonlinear distortion just as with the dual-parallel MZM linearization method mentioned in Section 2.4.5.

To show the cancellation of third order intermodulation distortion (3IMD), the combined optical power after the second PBS is observed. The optical power emitted from the left side optical port of the MZM just before reaching the left Faraday rotator is

$$P_{Left}(t) = P_{Right}\left[1-\sin\left(\frac{\pi V(t)}{V_\pi}\right)\right]\Big/2, \tag{2.11}$$

and optical power emitted from the right side optical port of the MZM just before reaching the right Faraday rotator is

$$P_{Right}(t) = P_{Left}\left[1+\sin\left(\frac{\pi\gamma V(t)}{V_\pi}\right)\right]\Big/2. \tag{2.12}$$

The total combined optical power is given by, $P_{Out}(t) = P_{Left}(t) + P_{Right}(t)$. Considering the above, one obtains the output optical power as

$$P_{Out}(t) = \frac{1}{2}\left[P_{Left}\left[1-\sin\left(\frac{\pi V(t)}{V_\pi}\right)\right] + P_{Right}\left[1+\sin\left(\frac{\pi\gamma V(t)}{V_\pi}\right)\right]\right]. \tag{2.13}$$

Using the Taylor series approximation until the third order, one now obtains the output optical power given by,

$$P_{Out}(t) \approx \frac{1}{2}\left[P_{Left}\left(1+\frac{\pi V(t)}{V_\pi}-\frac{1}{6}\left(\frac{\pi V(t)}{V_\pi}\right)^3\right)+P_{Right}\left(1-\frac{\pi\gamma V(t)}{V_\pi}+\frac{1}{6}\left(\frac{\pi\gamma V(t)}{V_\pi}\right)^3\right)\right]. \quad (2.14)$$

By simple mathematical manipulation, the output optical power is simplified into

$$P_{Out}(t) \approx \frac{1}{2}\left[P_{Left}+P_{Right}+\frac{\pi V(t)}{V_\pi}\left(P_{Left}-\gamma P_{Right}\right)-\frac{1}{6}\left(\frac{\pi V(t)}{V_\pi}\right)^3\left(P_{Left}-\gamma^3 P_{Right}\right)\right], \quad (2.15)$$

where the fourth term in (2.15) is related to the third order nonlinear distortion, which can be approximately cancelled if the condition of $P_{Left}/P_{Right}=\gamma^3$ is satisfied, where P_{Left} and P_{Right} are the unmodulated optical power applied to the left and right optical ports of the MZM, respectively. Considering the condition of $P_{Right}=P_{Left}/\gamma^3$, the following is obtained

$$P_{Out}(t) \approx \frac{1}{2}P_{Left}\left[\left(1+\frac{1}{\gamma^3}\right)+\frac{\pi V(t)}{V_\pi}\left(1-\frac{1}{\gamma^2}\right)\right], \quad (2.16)$$

where the average optical power for the transmitted optical carrier is

$$P_{carrier}=\frac{P_{Left}}{2}\left(1+\frac{1}{\gamma^3}\right) \quad (2.17)$$

and the optical subcarrier power for the RF signal is

$$P_{RFsub}=\frac{P_{Left}}{2}\frac{\pi V_0}{V_\pi}\left(1-\frac{1}{\gamma^2}\right), \quad (2.18)$$

where V_0 is the RF signal amplitude. This leads to a linearized modulation index of

$$m_{lin} = \frac{P_{RFsub}}{P_{carrier}} = \frac{\frac{P_{Left}}{2}\frac{\pi V_0}{V_\pi}\left(1-\frac{1}{\gamma^2}\right)}{\frac{P_{Left}}{2}\left(1+\frac{1}{\gamma^3}\right)} = m\frac{\gamma(\gamma-1)}{1-\gamma+\gamma^2}. \tag{2.19}$$

The relationship for the linearized modulation index normalized with unlinearized modulation index is given by,

$$\frac{m_{lin}}{m} = \frac{\gamma(\gamma-1)}{1-\gamma+\gamma^2}. \tag{2.20}$$

So it is seen from (2.20) that due to linearization there is a loss of modulation depth or RF carrier power as compared to a nonlinearized modulator by a factor of $\frac{\gamma(\gamma-1)}{1-\gamma+\gamma^2}$.

As seen from the optical response in [62], the co-propagating signal has a higher response than the counter-propagating signal provided the RF is greater than 2 GHz. Also shown is that there are ripples in the modulator response. These ripples are due to port reflections from non-ideal impedance matching and can be controlled by introducing a differential delay between the electrical RF driving signals. These port impedance mismatches need to be addressed so that optimal third order nonlinear distortion suppression is achieved. Also the polarization beam splitter, Faraday rotator and half wave plate will introduce large optical power losses, which will need to be compensated as well as for its complexity. Furthermore, this linearized modulator produces an ODSB signal, which is susceptible to RF power fading.

2.4.7 Mixed-Polarization Phase Modulation Linearization Technique

The mixed-polarization phase modulator is yet another proposed linearization method that is used to suppress third order nonlinear distortion [63]. The mixed-polarization

phase modulation is shown in Fig. 2.14, which consists of a linear polarizer adjusted to an angle of α, a z-cut $LiNbO_3$ phase modulator and a second linear polarizer adjusted to an angle of β. It is well known that z-cut $LiNbO_3$ phase modulator exhibits an electro-optic coefficient r_{31} along the x-(TE) axis, which is approximately 1/3 of r_{33} coefficient of the z- (TM) axis. This anisotropy will allow the RF signal to simultaneously modulate the light in both orthogonal polarized states by different amounts.

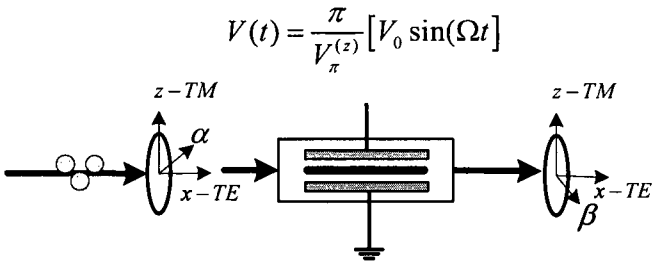

Figure 2.14 Mixed-polarization linearized phase modulator [63].

The mixed-polarization linearized phase modulator will be theoretically described to show how it functions. The optical signal entering the modulator passes through a linear polarizer set to an angle α with respect to the z-axis, this will excite a superposition of TE and TM modes that will be modulated to different modulation depths. In other words, the z-(TM) axis will carry more 3IMD, while the x-(TE) axis will carry less. The optical signal is then passed through a second linear polarizer that is set to angle β with respect to the z-axis. The two angles are related to each other, so they will be selected in such a fashion as to maximize the optical RF signal subcarriers and suppress 3IMD, which will be further described in Chapter 6. By carefully selecting α and β of the two linear polarizers, the combined 3IMD exiting the final polarizer can be cancelled.

For simplicity of analysis, a single RF tone is applied to the z-cut $LiNbO_3$ phase modulator electrodes. The normalized voltages applied to the electrode is represented by $V(t) = m\sin(\Omega t)$, where $m = \pi V_0 / V_\pi^{(z)}$, is the modulation depth for the z-polarized component of the electric field. The electric field exiting the first linear polarizer and entering the z-cut $LiNbO_3$ phase modulator electrode is represented by the vector $\bar{\mathbf{E}}_{in}(t) = E_0\left(\hat{z}\cos(\alpha) + \hat{x}\sin(\alpha)\right)e^{j\omega t}$, if birefringence is neglected. Thus, the electric field vector components of the light, which is modulated by electrode is represented by,

$$\bar{\mathbf{E}}_\alpha(t) = E_0\left(\hat{z}\cos(\alpha)e^{jm\sin(\Omega t)} + \hat{x}\sin(\alpha)e^{jm\gamma\sin(\Omega t)}\right)e^{j\omega t}/\sqrt{2}\,, \tag{2.21}$$

where γ is a dimensionless ratio, less than one that describes the electro-optic modulation ratio in the x-axis to that of the z-axis and ω is the optical angular frequency. By using the Jacobi-Auger expansion $e^{jx\sin(\Omega t)} = \sum_{n=-\infty}^{\infty} J_n(x)e^{jn\Omega t}$ on (2.21), one obtains the total electric field exiting the z-cut $LiNbO_3$ phase modulator just before the second linear polarizer. By ignoring the optical carrier component, the following is obtained,

$$\bar{\mathbf{E}}_{out,\alpha}(t) = \frac{E_0}{2}\left(\hat{z}\cos(\alpha)\left\{J_1(m)e^{j\Omega t} + J_1(m)e^{-j\Omega t}\right\} + \hat{x}\sin(\alpha)\left\{J_1(\gamma m)e^{j\Omega t} + J_1(\gamma m)e^{-j\Omega t}\right\} + \ldots\right)e^{j\omega t} \tag{2.22}$$

After the second linear polarizer, which is set to the angle of β with respect to the z-axis, the electric field component exiting the second linear polarizer is given by

$$E_{out,\beta}(t) = \frac{E_0}{2}\left(\cos(\alpha)\cos(\beta)\left\{J_1(m)e^{j\Omega t} + J_1(m)e^{-j\Omega t}\right\} + \sin(\alpha)\sin(\beta)\left\{J_1(\gamma m)e^{j\Omega t} + J_1(\gamma m)e^{-j\Omega t}\right\} + \ldots\right)e^{j\omega t} \tag{2.23}$$

Using the Bessel series expansion on (2.23), the output electric field becomes,

$$E_{out,\beta}(t)=\frac{E_0}{4}\left(\cos(\alpha)\cos(\beta)\left\{\begin{bmatrix}m-\frac{1}{8}m^3\end{bmatrix}e^{j\Omega t}+\\ \begin{bmatrix}-m+\frac{1}{8}m^3\end{bmatrix}e^{-j\Omega t}\end{bmatrix}+\sin(\alpha)\sin(\beta)\left\{\begin{bmatrix}\gamma m-\frac{1}{8}\gamma^3 m^3\end{bmatrix}e^{j\Omega t}+\\ \begin{bmatrix}-\gamma m+\frac{1}{8}\gamma^3 m^3+\end{bmatrix}e^{-j\Omega t}+\end{bmatrix}+\ldots\right)e^{j\omega t} \quad (2.24)$$

From (2.24) it can be seen that the terms proportional to m^3 is the 3IMD and they can be eliminated with the following condition,

$$\cos(\alpha)\cos(\beta)+\gamma^3\sin(\alpha)\sin(\beta)=0\,. \quad (2.25)$$

It may be seen that (2.25) does not have a unique solution and that 3IMD cancellation mostly depends on the polarization angles, so it would be ideal to choose a solution that maximizes the optical RF signal subcarriers, which are proportional to m and cancel the components which are proportional to m^3, which yields $\alpha=-\beta=\pm\tan^{-1}(\gamma^{-3/2})\approx\pm 79^0$ for $\gamma=1/3$. Also seen from (2.25), 3IMD suppression will not be greatly degraded if the two RF tones feeding each electrode have different electrical power. The linearization induces a decrease of optical RF signal subcarrier power by a factor of $\gamma(1-\gamma^2)/1+\gamma^3$, i.e. an 11 dB decrease for $\gamma=1/3$ [63].

Unfortunately, because only one phase modulator is used, it is required that one uses coherent homodyne or heterodyne detection at the receiver in order to recover the original transmission. This will lead to sinusoidal nonlinearities and will require a fast phase-locked loop or post detection digital signal processing [63]. A summary table of reviewed linearization techniques is shown in Table 2.1.

Table 2.1 Reviewed Linearization Techniques and Comment.

Linearization Techniques	Improvements	Drawbacks	Complexity	Cost
Pre-distortion / Adaptive pre-distortion	▪ 2^{nd} and 3^{rd} order suppression	▪ Bandwidth limited	Medium	Medium
Feed-forward	▪ 2^{nd} and 3^{rd} order suppression	▪ Bandwidth limited ▪ Independent aging DFB laser hinder linearization ▪ Difficult to combining 4 optical signals	High	High
Dual-parallel MZI	▪ 3^{rd} order suppression	▪ Two MZM used ▪ Independent optical MZM characteristics ▪ Power ratio between MZI must be accurately maintained	Low	Medium
Dual-cascaded MZI	▪ 2^{nd} and 3^{rd} order harmonic suppression	▪ Double insertion loss ▪ Independent DC biasing	Low	Medium
Electrical balanced system	▪ 2^{nd} order suppression ▪ Common mode RIN suppression	▪ Bandwidth limited	Low	Low
Dual fiber balanced system	▪ 2^{nd} order suppression ▪ Common mode RIN suppression	▪ Expensive, two SMF and optical modulators ▪ Difficult to operate, independent fiber and optical modulator characteristics	Medium	High
Dual wavelength balanced system	▪ 2^{nd} order suppression ▪ Common mode RIN suppression	▪ Expensive, two lasers and optical modulators ▪ Difficult to operate, independent laser and optical modulator characteristics	High	High

Bidirectional MZM	▪ 3rd order suppression ▪ Biased to reduce 2nd order distortion	▪ RF signal needs to be greater than 2 GHz ▪ Polarization beams splitter, Faraday rotator and half wave plate introduce large losses	Medium	Low
Mixed-polarization phase modulator	▪ 3rd order suppression	▪ Required homodyne or heterodyne detection ▪ Requires a PLL at receiver ▪ Sinusoidal nonlinearities	Low	Medium

2.5 Conclusion

This chapter has presented a comprehensive overview of the theoretical concepts needed to understand the proposed techniques that will be presented in this thesis. It has also at the same time provided a review of recent relevant techniques, where their theoretical operation and deficiencies are described. The chapter first presented the issue of RF power fading and the theory for why it occurs. Also described is the use of the Hilbert transform to generate OSSB modulation, which will become important in the performance improvements applied to the final two proposed linearized modulators presented in Chapters 5 and 6. Next, the balanced RoF systems currently being used were described and shown how they theoretically function, which will become essential and motivational for the proposed balanced RoF systems described in Chapters 3 and 4. Finally, linearization techniques and their deficiencies were discussed, along with relevant examples, such as the conventional balanced RoF system, dual-parallel MZM, bidirectional MZM and mixed-polarization phase modulator.

Chapter 3

3 Proposed Single Wavelength Balanced RoF System to Suppress Second Order Distortion

3.1 Introduction

As previously stated in Chapter 1, SCM used in RoF systems introduces the issue of nonlinearity, such as second order distortion mainly due to the optical modulator's transfer response and chromatic dispersion of the optical fiber, leading to lower receiver sensitivity. If this nonlinearity is not addressed, then fewer subscriber channels and shorter transmission distances may be supported by the RoF network, leading to inefficient RoF networks, which will ultimately increase broadband network costs. The issue of optical power fading, the generation of OSSB transmission and recent techniques that suppress nonlinear distortion were described in Chapter 2.

The proposed single wavelength balanced RoF system is presented, which further improves the balanced linearization performance [58], by using a single wavelength and fiber, thus reducing the balancing errors caused by independent fiber nonlinearities and chromatic dispersion. This balanced system does not seriously suffer from fiber dispersion, because only one wavelength is utilized and as a direct result the proposed balanced system outperforms the conventional balanced system noted in Chapter 2.

This chapter is organized as follows; Section 3.2 will introduce and describe the proposed single wavelength balanced RoF system, Section 3.3 will provide a comparison of the simulated second order suppression to the nonlinearized conventional system, referred to as the conventional system and dual wavelength balanced system referred to as conventional balanced system. It will be shown that the proposed balanced system improves second order suppression and receiver sensitivity, which as a direct result leads to improved BER over the conventional balanced systems and in Section 3.4 some conclusions will be drawn.

3.2 Proposed Single Wavelength Balanced RoF System

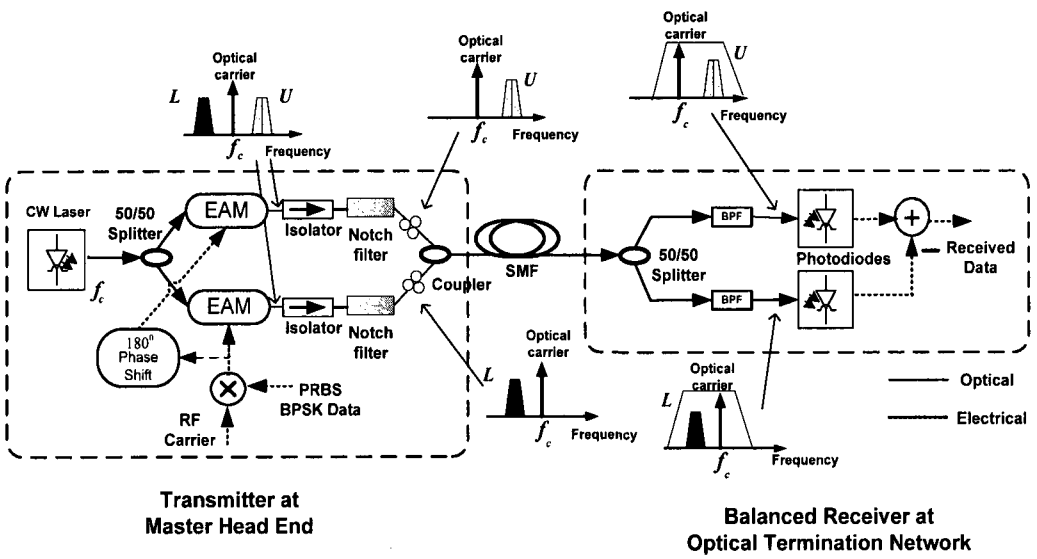

Figure 3.1 Proposed single wavelength balanced RoF system.

The proposed single wavelength balanced RoF system is schematically shown in Fig. 3.1. A CW laser at 1553 nm with laser linewidth of 800 KHz and RIN of -150 dB/Hz is split into two branches by the use of a 50/50 optical splitter and fed into two EAMs. The two EAMs are biased at a third order null to reduce third order distortion and are driven by a BPSK RF signal with the lower branch being phased shifted by 180^0. Due to SCM, two ODSB modulations will be obtained, each with its set of optical subcarriers and optical carriers after the EAMs. Following the optical notch filters, which will be described later in this section, only one of the subcarrier sideband will remain. The upper branch will carry only the upper subcarrier sideband (USB) and the lower branch the lower subcarrier sideband (LSB). The optical coupler will then combine them, and recreate the ODSB transmission with its two sidebands carrying the same modulation information, but phase shifted by 180^0. After fiber transmission, an optical 50/50 optical splitter at the receiver splits the received optical power in half and feeds them to the optical receiver, where they are fed to an optical bandpass filter (BPF), so that the respective sidebands are recovered.

The USB is fed to the upper photodiode and the LSB is fed to the lower photodiode. The received electrical RF signals are then subtracted to give the linearized received signal. The optical BPFs may be implemented using fiber Bragg grating base Fabry-Perot filter (FBG-FP), where highly reflective FBGs of identical wavelength form a resonator that allow for multiple reflections between them to create multiple resonate peaks in the stop band of a single FBG. The FBG-FP needs to be between 15 to 30 mm in length for convenient packaging. The bandwidth is determined by the spacing of the resonant peaks and the reflectivity of the FBGs. It was demonstrated with two identical 12 mm FBGs separated by 4 mm, that a stop band of -20 to -40 dB with bandwidth of less than 1 pm

can be easily achieved, where 1 pm bandwidth is approximately 125 MHz in the wavelength region of 1550 nm [64]. The single wavelength balanced RoF system shown in Fig. 3.1 uses a Gaussian notch filter centered at the sideband frequency that one wants to eliminate with stopband of 30 dB and bandwidth of 2.5 GHz. The Gaussian BPFs just before the balanced receiver in the upper and lower branches is centered at 193.1 THz ± the desired RF carrier frequency, both with bandwidth of 25 GHz and stopband of 30 dB.

3.3 Analysis and Simulation Results

3.3.1 Received RF Power

Figure 3.2 shows the transfer response of the OKI Electric Industry Co., Ltd. Type # OM5642M-30B EAM, which only has a small linear region between 2.25 and 2.75V. Composite RF signals that are fed to this EAM, if they fall outside this linear region, will be corrupted by nonlinear distortion. The response was obtained experimentally by feeding the optical modulator with a 0 dBm CW light set to a wavelength of 1553 nm and sweeping the RF input port with a reverse DC signal from 0 to 4V, while the optical output power was recorded.

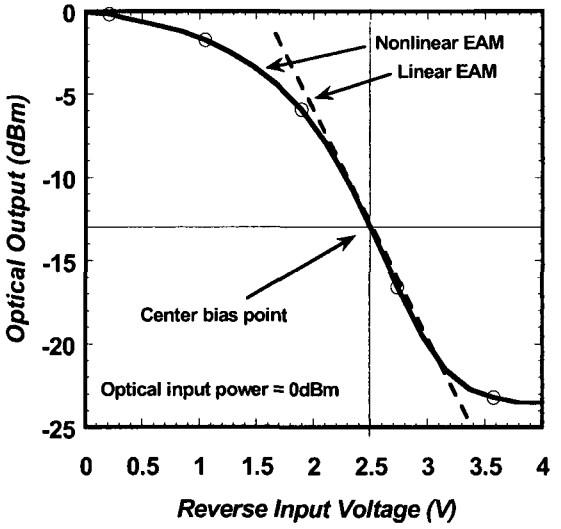

Figure 3.2 Measured optical response for the OKI Electric Industry Co., Ltd. Type # OM5642M-30B EAM.

An "ideal" EAM was first considered that has a linear response. If a linear EAM is simulated and fed with a 0 dBm CW light set to a wavelength of 1553 nm, while the RF input port was fed with a 12 GHz sinusoidal signal, the received power will be different for the back-to-back and through 25 km of SMF. Figure 3.3 shows the simulated optical RF tone power (i.e. optical subcarrier power), second order harmonic (2HD) and third order intermodulation (3IMD) powers for the back-to-back and through 25 km of fiber transmission considering the "ideal" EAM. Figure 3.3(a) shows a linear response for all signal components at 12 GHz, 14 GHz and 24 GHz, which is the RF signal, 3IMD and 2HD, respectively. On the contrary, for the case with 25 km of fiber transmission, Fig. 3.3(b) shows a nonlinear response despite the fact that the EAM response is linear. The reason for this is that chromatic dispersion induces nonlinearity in the RoF system.

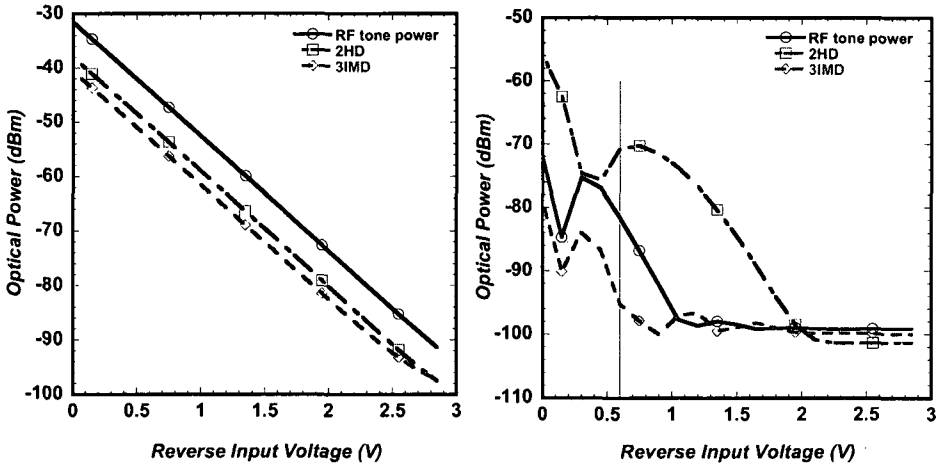

(a) (b)

Figure 3.3 Optical received power versus biasing for the linear EAM in (a) a back-to-back case and (b) through 25 km SMF.

The power transmission response that is used for all proceeding nonlinear EAM simulations is modeled after the OKI Electric Industry Co., Ltd. Type # OM5642M-30B EAM polynomial, where it was experimentally determined and given by,

$$T_{dBm}(V(t)) = -0.08254 + 1.7043V(t) - 17.125V^2(t) + 42.588V^3(t) - 55.748V^4(t) + 40.196V^5(t) - 16.15V^6(t) + 3.2113V^7(t) - 0.1374V^8(t) - 0.048066V^9(t) + 0.0055029V^{10}(t) \quad (3.1)$$

Figure 3.4 shows the received RF power if using the nonlinear EAM in a back-to-back and through 25 km of SMF systems. For both of these simulations the composite two tones powers at 10 and 12 GHz were adjusted to be 29.9 dBm with the EAM having a 6 dB insertion loss. The CW laser is set to 1553 nm with linewidth of 800 KHz and RIN of -150 dB/Hz as mentioned above. The optical transmission is through 25 km of SMF with an attenuation of 0.2 dB/km and chromatic dispersion of $16\,ps/(nm \cdot km)$. The final component of the link is the PIN photodiode detector with responsivity of 1.0 A/W and

thermal noise of 10^{-12} A/√Hz. It may be seen from Fig. 3.4 that the EAM has both second and third order nulls unlike the MZM, where it only has second order nulls as mentioned in Chapter 1. The bias setting for the EAM will be different depending on the amount of chromatic dispersion encountered by the optical signal. It is required to choose a third order null with maximum RF tone power. In Fig. 3.4(a) the EAM bias will need to be 2.25V in the back-to-back case and from Fig. 3.4(b) it will need to be 1.6V for the 25 km of SMF case.

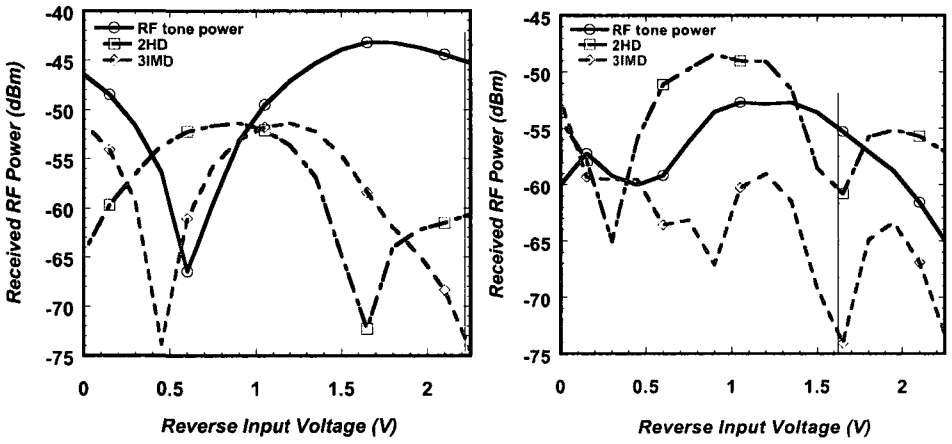

(a) (b)

Figure 3.4 Received RF power versus biasing for the nonlinear EAM in (a) back-to-back and (b) through 25 km SMF.

Now the proposed balanced system is considered. Using the same simulation setup, received RF power, 2HD and 3IMD power with the EAM bias voltage are displayed in Fig. 3.5 for the back-to-back and 25 km of fiber transmission. Note that the proposed single wavelength balanced system has the EAM bias set to 1 V in both the back-to-back and through 25 km of SMF cases. Also noted is that the second order distortion is suppressed below -95 dBm, despite the same bias being used.

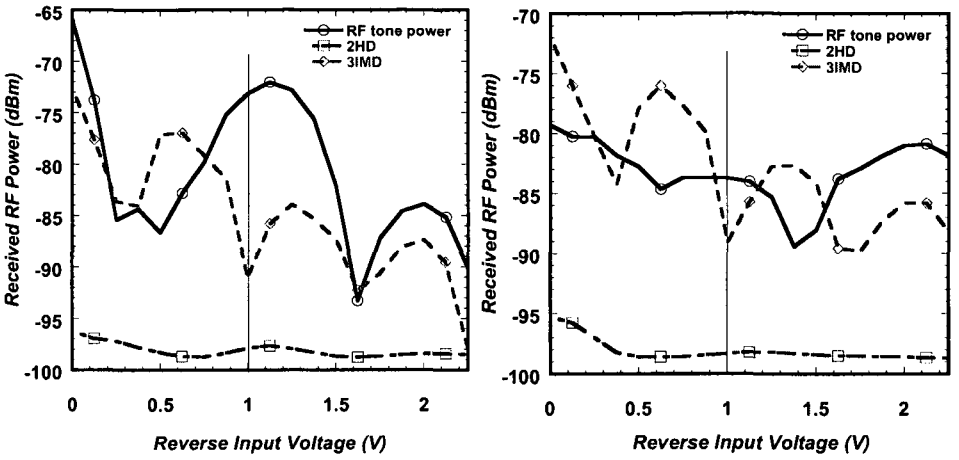

Figure 3.5 Received RF power versus biasing for the proposed balanced RoF system in (a) back-to-back and (b) through 25 km SMF cases.

Two systems are compared with the use of simulation; one is ODSB RoF system that uses the nonlinear EAM, and the other is the proposed balanced system shown in Fig. 3.1. In both cases the optimum bias of 2.5V was used, which places the RF signal in the center of the linear region of the nonlinear EAM as shown in Fig. 3.2 and the fiber attenuation was compensated, but not the chromatic dispersion, which is set to 16 $ps/(nm \cdot km)$. Figure 3.6 shows the received RF power versus fiber length for the above two systems. It is seen from Fig. 3.6(b) that there are nulls in both the RF carrier and third order distortion due to chromatic dispersion, which causes power fading. It is also noted that the second order distortion is suppressed below -95 dBm despite the fiber length, unlike the nonlinear EAM in Fig. 3.6(a), where the second and third order distortions have almost equal power as the RF carrier.

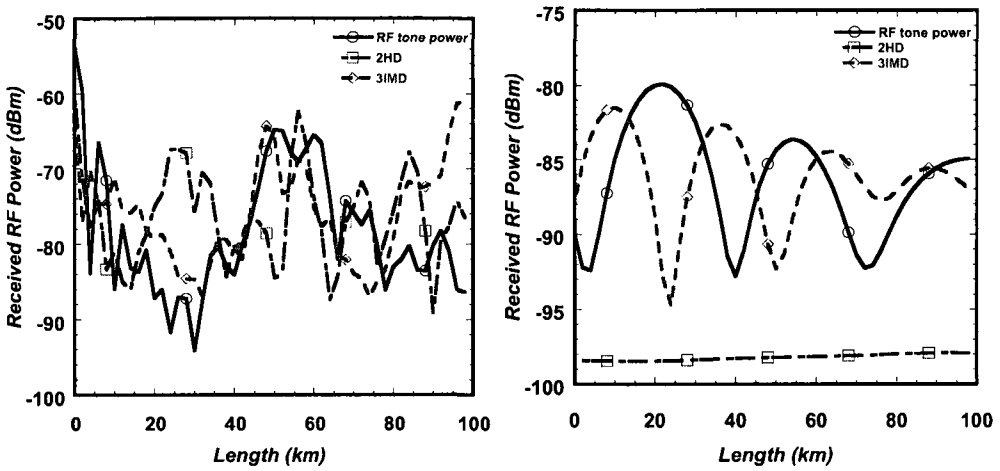

(a) (b)

Figure 3.6 Received RF power versus fiber length for (a) the ODSB RoF system using nonlinear EAM and (b) the proposed balanced system.

Phase delay sensitivity between the two photodetector branches is now investigated for the proposed balanced and conventional balanced (dual wavelength balanced) systems. In both cases the optical transmission is through 25 km of SMF and the bias is adjusted to 2.5V for both modulators to be optimum, meaning that a third order null with maximum optical RF signal subcarrier power is obtained. Figure 3.7 shows simulated RF power output versus phase difference. It is noted from Fig. 3.7 that the optimized phase difference is at the angle of 0^0, where the third order distortion is at the lowest point and the RF carrier power is at a maximum. It is seen that the proposed balanced system is less sensitive to phase differences at the receiver, because it uses the same wavelength for both channels. Figure 3.7 shows that even at a phase difference of $\pm 20^0$ only a 5 dB power increase in third order distortion is observed and relatively no change in RF carrier and second order distortion power.

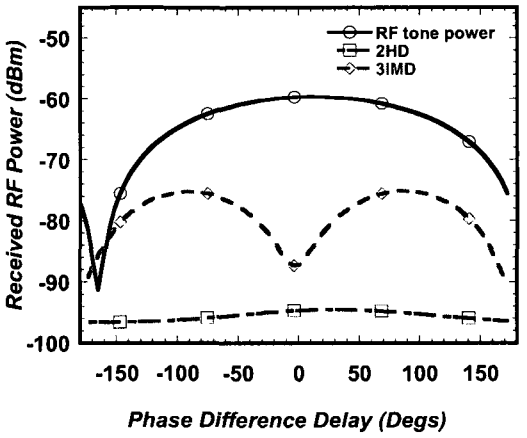

Figure 3.7 Received RF power versus phase difference for the proposed balanced system.

On the other hand with the same simulation conducted, Fig. 3.8 shows received RF power versus phase difference for the conventional balanced system. Figure 3.8 was obtained using frequencies of 193.1 and 193.2 THz though 25 km of SMF. It is seen that the conventional balanced system is more susceptible to phase differences between the photodetector branches, because two separate wavelengths are used, thus a phase difference of $\pm 20^0$ produces a 9 dB power increase in third order distortion and a 9 dB increase in second order distortion power. Also noted is that the RF carrier power remains relatively unchanged in the observation range.

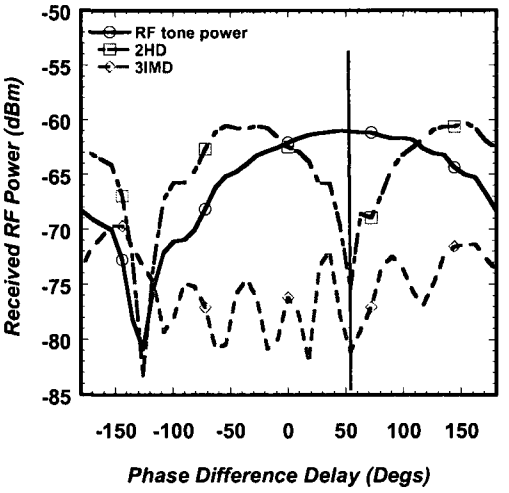

Figure 3.8 Received RF power versus phase difference for the conventional balanced system with frequency separation of 100 GHz.

A performance comparison for the proposed balanced and the conventional balanced system through 25 km of SMF with compensated attenuation is performed. Again the bias of 2.5V was used, which puts the RF signal in the center of the EAM's linear region. Figures 3.9(a) and (b) shows the simulated received RF power versus input RF power through 25 km of SMF for both the proposed and conventional balanced systems with compensation only for fiber attenuation, respectively. It is seen from Fig. 3.9(a) that the proposed balanced system suppresses second order distortion despite the input RF carrier power, unlike the conventional balanced system, where there is a steady increase in second order distortion as input RF power is increased as seen in Fig. 3.9(b). This is due to the dual wavelength spectral separation in the conventional balanced system, which is more susceptible to phase difference errors and periodic fading caused by the chromatic dispersion as discussed in Chapter 2.

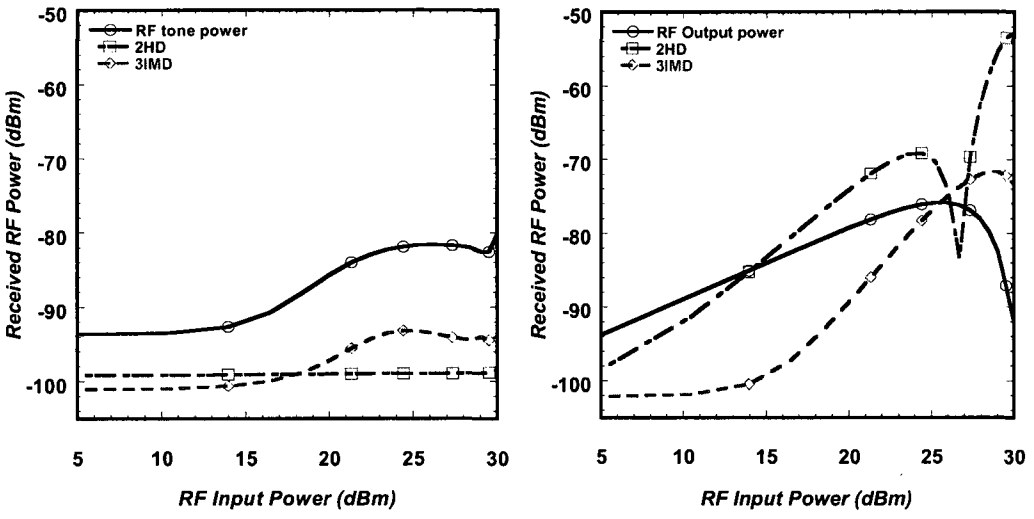

(a) (b)

Figure 3.9 Received RF power versus input RF power for the (a) proposed balanced and (b) the conventional balanced system through 25 km of SMF with compensated attenuation.

3.3.2 BER Analysis

In the BER analysis, a BPSK information signal is considered with a bit rate of 16x155 Mb/s =2.48 Gb/s and RF carrier frequencies of 10 and 35 GHz. In the simulations it is assumed that the two Gaussian bandpass filters have a channel spacing of 10 (35) GHz and each filter has a bandwidth of 10 (35) GHz, respectively. Furthermore, the bandpass filters have a stopband of 30 dB. A SMF of 25 km was used with attenuation of 0.2 dB/km and chromatic dispersion of 16 $ps/(nm \cdot km)$. The PIN diode in optical receiver is modeled with a responsivity of 1.0 A/W, thermal noise density of 10^{-12} A/$\sqrt{Hz}$ and shot noise. After the photodetection a bandpass filter with a bandwidth of 3 GHz is used. For the conventional balanced system two non-phase locked lasers with wavelengths of 1552 and 1553 nm separated by 1.0 nm are used. In order for later analysis of nonlinear

distortion reduction, both an "ideal" EAM, i.e. having a linear response characteristic and nonlinear EAM, i.e. having a nonlinear response characteristics are assumed and shown in Fig. 3.2.

The detailed comparison of harmonic distortion suppression impact is shown in Fig. 3.10, which shows the comparison of simulated BER with received optical power for four RoF systems. The four compared systems are noted as follows; the conventional nonlinear EAM (C-NEAM), the proposed balanced system with two nonlinear EAMs (B-NEAM) shown in Fig. 3.2, the conventional balanced system with two nonlinear EAMs (CB-NEAM) and finally, the proposed balanced system with linear EAMs shown in Fig. 3.2 (B-LEAM) for RF = 10 and 35 GHz, respectively. In order to keep the comparison fair the same optical input power and modulation depth are maintained, so any improvements found will be a direct result of a more linearized system. For RF=10 GHz as shown in Fig. 3.10(a), it is seen that the B-NEAM has almost perfect suppression of 2HD when compared to the B-LEAM, as shown in Fig. 3.10(b), in which 2HD is almost suppressed to the noise floor. The small residual power penalty induced by the B-NEAM is due to residual 2HD and 3HD. A comparison of the B-NEAM with CB-NEAM / C-NEAM shows that a 0.8/3.0 dB improvement of receiver sensitivity due to less 2HD is obtained by using the B-NEAM at BER=10^{-9}. Figures 3.10(a) and (b) shows a comparison of the BER versus received optical power at RF=35 GHz. The B-NEAM is slightly better than CB-NEAM for this case. Because for the back-to-back systems, HD2 suppression in CB-NEAM is dependent on the initial optical phase difference due to phase noise between the two lasers, B-NEAM may be slightly or significantly better than CB-NEAM depending on the initial optical phase difference in B-NEAM. Moreover, a ~2 dB improvement of receiver sensitivity with B-NEAM is obtained compared to C-

NEAM. Because different optical signal subcarrier frequencies lead to increases or decreases in 3HD generation for the same bias, it is observed that an optical modulation depth of ~1 dB larger for RF=35 than for 10 GHz is due to different optimal biases used to better null 3HD, resulting in better performance at RF=35 GHz as shown in Fig. 3.10(b) [5].

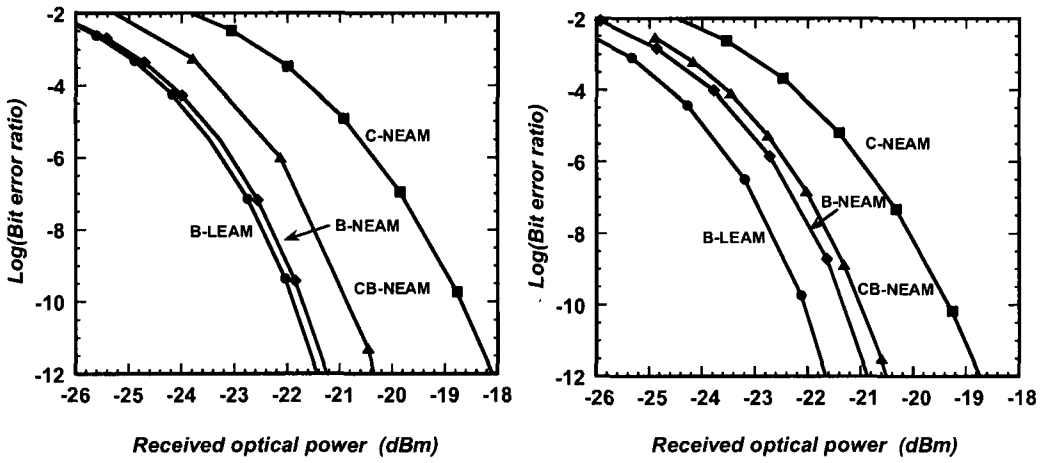

Figure 3.10 Simulated BER versus received optical power for B-LEAM (black circle), B-NEAM (black diamond), CB-NEAM (black triangle) and C-NEAM (black square) for (a) RF=10 GHz and (b) RF= 35 GHz in a back-to-back configuration.

A comparison of the above four systems are considered, but with transmission through 25 km SMF, which is a typical fiber segment length for a RoF network. As shown in Fig. 3.11(a) for RF=10 GHz the B-NEAM still provides a large advantage over C-NEAM and CB-NEAM, even though the B-NEAM is equivalent to a double sideband RoF system, which may be sensitive to chromatic dispersion. Also, as shown in Fig. 3.11(b) for RF=35 GHz the B-NEAM is still much better than C-NEAM in which OSSB modulation was used and is hardly degraded by chromatic dispersion. On the contrary, CB-NEAM is worse than C-NEAM in performance, resulting in balanced detection being

non-beneficial. This is because chromatic dispersion introduces additional relative phase difference in CB-NEAM due to larger separation between the two branch optical signal subcarriers. Furthermore, ~3 dB RIN suppression is observed in the simulations by using the B-NEAM system.

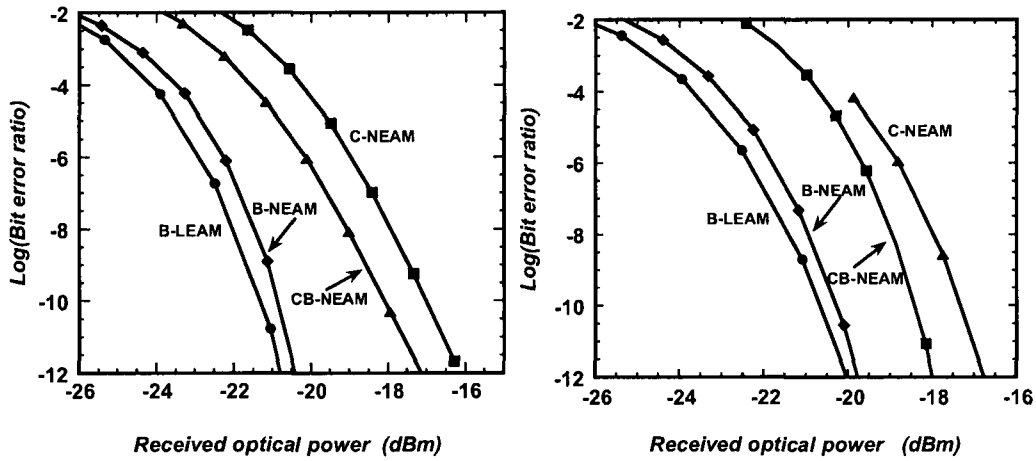

(a) (b)

Figure 3.11 Corresponding to Fig. 3.10, but all four systems with 25 km SMF transmission instead of back-to-back.

3.3.3 Analysis of Second Order Intermodulation Suppression

Next it is briefly shown that 2IMD can be better suppressed as well by using the B-NEAM compared to CB-NEAM. Figures 3.12(a), (b) and (c) show electrical spectra obtained from C-NEAM, B-NEAM and CB-NEAM with two optical signal subcarriers at 10 and 15 GHz through 25 km SMF transmission. 3IMD, i.e. third order IMD, is located at 5, 20, 35 and 40 GHz, and the EAM biases have been optimized to better suppress 3IMD at 5 and 25 GHz in all three systems, in which the EAM bias is set the same. It is seen that 2IMD at 5 GHz is dominating in C-NEAM as shown in Fig. 3.12(a). By using

the B-NEAM, suppression of 32 dB in 2IMD is obtained, which is shown in Fig. 3.12(b) compared to C-NEAM. On the contrary, balanced detection in CB-NEAM cannot suppress 2IMD (5 GHz) as shown in Fig. 3.12(c). The balanced detection current for 2HD and 2IMD is given by

$$\begin{aligned} I_2(t) \propto P_{U,2}\{\cos(2\omega_1 t)+\cos(2\omega_2 t)+\cos[(\omega_1-\omega_2)t]+\cos[(\omega_1+\omega_2)t]\}- \\ P_{L,2}\{\cos(2\omega_1 t-2\omega_1\tau-2\psi)+\cos(2\omega_2 t-2\omega_2\tau-2\psi)+\cos[(\omega_1-\omega_2)t-(\omega_1-\omega_2)\tau-\psi] \\ +\cos[(\omega_1+\omega_2)t-(\omega_1+\omega_2)\tau-\psi]\} \end{aligned} \tag{3.2}$$

where $P_{U,2}$ ($P_{L,2}$) is the optical power of the second-order nonlinear distortion in the upper (lower) branch, ω_1 and ω_2 are optical subcarrier angular frequencies, τ is relative time delay induced by chromatic dispersion between the two branches, and ψ is the initial optical phase difference between the two branches. To obtain perfect suppression of 2HD/2IMD, $P_{U,2}$ must be equal to $P_{L,2}$, and optical time delay τ and initial phase difference ψ must be zero. However, because in CB-NEAM two non-phase locked lasers were used, the initial optical phase difference ψ will not be zero and is random. Also because of the use of two wavelengths in CB-NEAM, a larger time delay τ is introduced and thus CB-NEAM is always worse than B-NEAM. In addition, it is found that the critical fiber length due to chromatic dispersion for B-NEAM is ~34/29 km for RF = 10/35 GHz at which point a BER of 10^{-9} cannot be achieved. However, this critical length can be changed by detuning the relative modulating RF carrier phase away from 180^0. Note, that RF signal carriers as shown in Fig. 3.12(b) are suppressed as well due to

destructive interaction in B-NEAM compared to increased RF signal carriers due to constructive interaction in CB-NEAM as shown in Fig. 3.12(c).

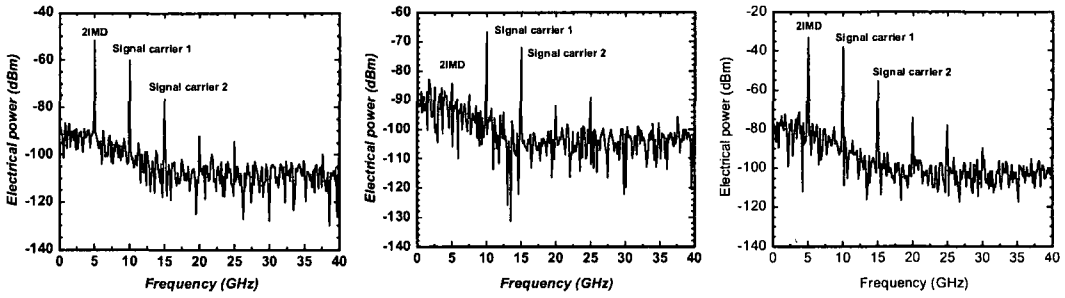

Figure 3.12 Electrical spectra obtained from (a) C-NEAM, (b) B-NEAM, and (c) CB-NEAM after 25 km SMF transmission. For all three systems, the nonlinear EAM is shown in Fig. 3.2 with the same bias used for SCM at RF=10 and 15 GHz.

3.4 Conclusion

In this chapter, a proposed balanced RoF system using a single wavelength and one fiber is presented, instead of two wavelengths and one fiber or one wavelength and two fibers as previously described in Chapter 2. With the use of simulations it has been shown that the proposed balanced RoF system outperforms the conventional ODSB and conventional balanced RoF system. It has been found that better suppression of 2HD and 2IMD can be achieved by using this proposed balanced system compared to the conventional balanced system. Specifically, there is an improvement of 32 dB in 2IMD suppression obtained with the proposed single wavelength balanced RoF system over the conventional ODSB RoF system through 25 km of SMF. Also there is an improvement of 6.6 dB over the proposed single wavelength balanced over conventional balanced RoF system when 25

km of SMF is used. Moreover, the proposed balanced system is immune to laser phase noise and RIN can be suppressed. In the next chapter it will be shown by simulation that there is a 3 dB suppression in common mode RIN. The two notch filters used to eliminate the unneeded sidebands does introduce complexity and cost to the proposed balanced system. A possible remedy is to use two MZMs instead EAMs, in an OSSB SCM configuration as shown in Chapter 2 to generate the two need sidebands. This will reduce complexity and cost, while improving stability and performance.

Chapter 4

4 Proposed Tunable FBG Balanced RoF System to Suppress both Second and Third Order Distortions

4.1 Introduction

The proposed single wavelength balanced RoF system presented in Chapter 3 is only capable of suppressing second order distortion, the EAMs that are used need to be biased at a third order null in order to achieve overall performance improvement. Because there is a limitation in choosing the bias this way, some optical RF signal subcarrier power will be sacrificed, which will then need to be compensated for by using an optical amplifier. Furthermore, the proposed single wavelength balanced system requires the use of two optical modulators, which will increase cost for the RoF system. So this is the motivation for the next proposed design to alleviate the biasing restriction, suppress both second and third order nonlinear distortions and reduce system cost by implementing one optical modulator.

Presented is the proposed tunable FBG balanced RoF system, which makes use of only one EAM and two cascaded tunable nonlinearly chirped fiber Bragg gratings (FBGs), which are tuned with a piezoelectric stretcher [65]. It will be shown that the proposed tunable FBG balanced system will perform as well in reducing nonlinear distortion as the single wavelength balanced system presented in Chapter 3, but will have

the bias limitation removed, which will reduce the optical RF signal subcarrier power penalty due to freedom of bias selection, suppress both second and third order distortions and will be cost effective because only one EAM is used.

The following chapter will be organized as follows; Section 4.2 will introduce and describe the proposed tunable FBG balanced RoF system, Section 4.3 will provide simulation results for the nonlinear distortion suppression, BER improvement and RIN suppression, where the proposed tunable FBG balanced system is compared against the conventional OSSB system, and Section 4.4 will draw some conclusions.

4.2 Proposed Tunable FBG Balanced RoF System

Presented is the proposed tunable FBG balanced RoF system that uses only one wavelength, optical modulator and fiber. In this balanced system the upper and lower sidebands produced by SCM along with its optical carrier are separated before balanced photodetection. Optical time delays are introduced to one of the sidebands by means of two cascaded tunable nonlinearly chirped FBGs. The first nonlinearly chirped FBG produces relative time delay that has the following relationship $\tau_{delay} \propto 1/2f$, where f is the RF carrier frequency, while the second produces a relative time delay of $\tau_{delay} \propto 1/f$. The first nonlinearly chirped fiber Bragg grating will have a large bandwidth and group velocity dispersion to introduce a relative time delay for the optical subcarrier and second order distortion components, while the second will have the bandwidth and group velocity dispersion to introduce a different relative time delay for the third order

distortion. The net effect of the relative time delays is to provide a phase shift of π for the subcarrier and second order distortion components and a phase shift of 2π for the third order distortion components.

Figure 4.1 schematically shows the proposed tunable FBG balanced system. A CW laser at 1553 nm with linewidth of 800 KHz and relative intensity noise (RIN) of -150 dB/Hz is injected into an EAM with nonlinear response characteristic shown in Fig. 3.2 from Chapter 3. By SCM, the optical carrier and double sideband subcarriers are generated and transmitted through SMF, which has chromatic dispersion of 16 $ps/(nm \cdot km)$. After fiber transmission, the two optical subcarriers are filtered out along with half the optical carrier power using a 50/50% optical splitter. Two notch filters composed of fiber Bragg gratings (FBGs) are used to remove the unwanted optical subcarrier components, i.e. USB (U) in the upper branch and LSB (L) in the lower branch as shown in Fig. 4.1. In the upper branch the optical carrier and USB subcarrier are fed into one photodiode of the balanced optical receiver. In the lower branch an optical time delay line is inserted, which is realized using an optical circulator and tunable nonlinearly chirped FBG [65, 66], before being fed to the other photodiode of the balanced optical receiver. Three polarization maintaining fibers are required, one in each fiber branch and one at the first output of the circulator. This will minimize polarization mismatches at the balanced photodetector.

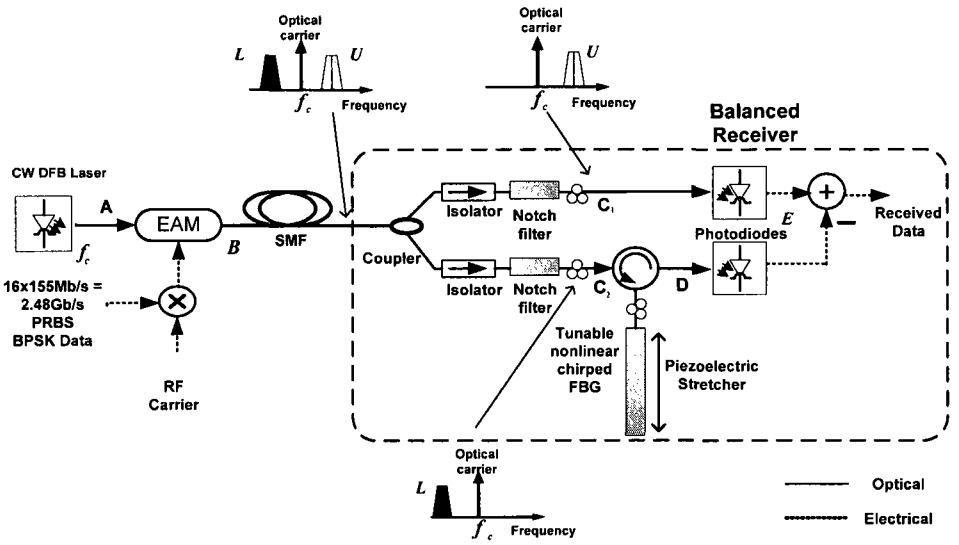

Figure 4.1 Proposed RoF balanced system using single wavelength, single optical modulator and cascaded nonlinearly chirped FBGs [67].

The introduced relative time delay in the lower branch causes a relative phase shift in the detected current. This detected current may be expressed as $I_d = \left[I_1^U + I_2^U + I_3^U\right] - \left[I_1^L \cos\theta_1 + I_2^L \cos^2\theta_2 + I_3^L \cos^3\theta_3\right]$, where I_1, I_2, and I_3 are the currents of signal carrier, second and third order nonlinear distortions, respectively from the upper and lower branches and θ_1, θ_2 and θ_3 are relative phases of the corresponding currents between the two branches. If θ_1 and θ_2 equal to π, obtained by tuning the chromatic dispersion of the nonlinearly chirped FBG, then the currents of signal carrier add up and the currents of the second nonlinear distortion subtract. For the second cascaded FBG θ_3 can be set equal to 2π and thus the third order nonlinear distortion current will subtract. Including chromatic dispersion and phase noise, the second and third order nonlinear distortions for two RF subcarriers carried by one optical carrier can be further expressed by

$$I_2(t) \propto P_{U,2}\{\cos(2\omega_1 t)+\cos(2\omega_2 t)+\cos[(\omega_1 \mp \omega_2)t]+\cos[(\omega_2 \pm \omega_1)t]\} \quad (4.1)$$
$$-P_{L,2}\{\cos[2\omega_1 t-2\omega_1\tau-2\psi]+\cos[2\omega_2 t-2\omega_2\tau-2\psi]$$
$$+\cos[(\omega_1 \mp \omega_2)t-(\omega_1 \mp \omega_2)\tau-\psi]+\cos[(\omega_2 \pm \omega_1)t-(\omega_2 \pm \omega_1)\tau-\psi]\}$$

$$I_3(t) \propto P_{U,3}\{\cos 3\omega_1 t+\cos 3\omega_2 t+\cos[(2\omega_1 \pm \omega_2)t]+\cos[(2\omega_2 \mp \omega_1)t]\} \quad (4.2)$$
$$-P_{L,3}\{\cos[3\omega_1(t-\tau)-3\psi]+\cos[3\omega_2(t-\tau)-3\psi]$$
$$+\cos[(2\omega_1 \pm \omega_2)(t-\tau)-\psi]+\cos[(2\omega_2 \mp \omega_1)(t-\tau)-\psi]\}$$

where $P_{U,2}$ ($P_{L,2}$), and $P_{U,3}(P_{L,3})$ are the electrical powers of the second order and third order nonlinear distortions in the upper (lower) branches, respectively, ω_1 and ω_2 are two optical subcarrier angular frequencies, τ is time delay difference between the two optical branch signals and ψ is the optical phase difference in the two branches, which is random due to different laser phase and shot noise. In order to achieve better cancellation of second and third order nonlinear distortions, it is required to have $\theta_2 = \pi$ and $\theta_3 = 2\pi$, i.e. the different time delays τ required in (4.1) for the reduction of 2HD, 3HD and IMDs. Also ψ needs to be zero, $P_{U,2}$ is equal to $P_{L,2}$ and $P_{U,3}$ is equal to $P_{L,3}$. However, ψ cannot be zero due to polarization changes at the tunable FBG. But ψ will be negligible because the tunable FBG is incorporated in the receiver and interconnecting polarization maintaining fibers are very short in length.

It is well known that for a RoF system with double sideband subcarriers, the received electrical power after photodetection is given by, $P_{elec.,f} \propto \cos^2\left(\frac{\varphi_1+\varphi_2}{2}\right) = \cos^2\left[\pi cLD\left(\frac{f}{f_c}\right)^2\right]$, where φ_1 and φ_2 are the phases of the modulated double sidebands relative to the optical

carrier, c is the speed of light in a vacuum, L is transmission fiber length, D is chromatic dispersion, f is the subcarrier frequency and f_c is the optical carrier frequency. It is seen that the received electrical power $P_{elec,f}$ is dependent on fiber length and chromatic dispersion with periodic power oscillations. However, for the proposed RoF balanced system in Fig. 4.1 electrical power fading does not occur because the relative time delay between the two optical subcarriers can be optimized by tuning the relative delay in the lower branch of the RoF system using the nonlinearly chirped FBG. The variable relative time delays provided by the nonlinearly chirped FBGs may be achieved by stretching them with a piezoelectric stretcher as shown in Fig. 4.2, which results in changes of relative time delay and group velocity dispersion (GVD) slope [66, 67]. Note that the actual relative time delay versus frequency is made up of several discrete components as seen in Fig. 4.2, this is due to discrete etching of the FBG. The PIN diodes in optical balanced receiver are modeled with a responsivity of 1.0 A/W, thermal noise density of 10^{-12} A/$\sqrt{\text{Hz}}$ and shot noise. After the photodetection a bandpass filter with a bandwidth of 3 GHz is used.

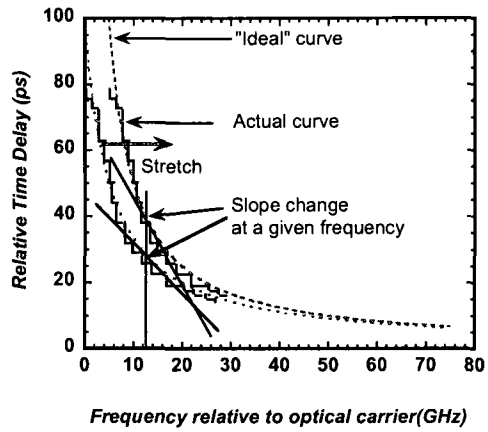

Figure 4.2"Ideal" and actual relative time delays versus frequency for the tunable nonlinearly chirped FBG, $\tau_{rel} \propto 1/2f$, where τ_{rel} is the relative time delay and f is the optical subcarrier frequency with respect to the optical carrier.

4.3 Simulation Results and Analysis

A back-to-back RoF system as shown in Fig. 4.1 is first considered, driven by a sinusoidal RF tone. If only photodetection from the upper branch is considered, i.e. conventional OSSB RoF system, the electrical spectrum is shown in Fig. 4.3(a) for an optical subcarrier at 10 GHz. Correspondingly, the electrical spectrum using the proposed RoF balanced system as shown in Fig. 4.1 is shown in Fig. 4.3(b). A nonlinear EAM, which has stronger second order nonlinearity, was used and its bias was adjusted to minimize third order HD (3HD). Two cascaded chirped FBGs are used, the first one has GVD of -625, -156, and -140 ps/nm with respect to the optical carrier at frequencies of 10, 20 and 30 GHz, respectively, with bandwidth of 25 GHz, and the second one only covers the 3HD at 30 GHz with GVD of -156 ps/nm at 30 GHz and bandwidth of 25 GHz. Insertion loss of all optical components and polarization angles are ignored. The

tunable FBG balanced RoF system shown in Fig. 4.1 uses a Gaussian notch filter centered at the sideband frequency that one wants to eliminate with stopband of 30 dB and bandwidth of 2.5 GHz.

By comparing both figures, it is obvious that the 2HD using the proposed RoF balanced system is reduced by 25.4 dB and the 3HD by 2.6 dB. The unreduced 2HD and 3HD are mainly due to independent shot noise of the two PIN diodes in the balanced receiver and random laser phase noise, i.e. $\psi \neq 0$. If an EAM has a stronger third nonlinearity, a better suppression of the third order nonlinear distortion can also be achieved by tuning the time delays of the two nonlinearly chirped FBGs.

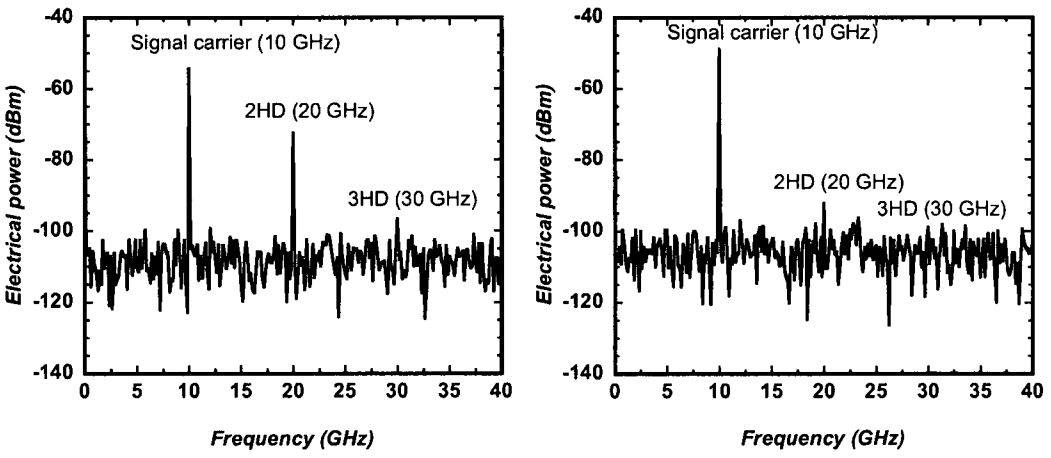

Figure 4.3 Electrical spectra of a back-to-back (a) conventional OSSB RoF system (i.e. upper branch only) and (b) the proposed RoF balanced system, both with an optical subcarrier frequency of 10 GHz.

The suppression of second and third order IMD (2IMD and 3IMD) using the proposed balanced system will now be shown. Two RF sinusoidal tones at 10 and 19

GHz are considered, which simultaneously drive the nonlinear EAM in a back-to-back system. For the conventional OSSB RoF system i.e. upper branch only, the electrical spectrum is shown in Fig. 4.4(a). For this case, two 2IMDs occur at 9 and 29 GHz and the 2IMD at 9 GHz is most detrimental because of its proximity to the RF carrier at 10 GHz. Also there is a 3IMD occurring at 28 GHz, which, as an example, can be reduced with another cascaded nonlinearly chirped FBG. When using the proposed RoF balanced system with one FBG, which has GVD of -772, -625 and -173 ps/nm at frequency of 9, 10 and 19 GHz, respectively, with bandwidth of 50 GHz, the electrical spectrum is shown in Fig. 4.4(b). With the two cascaded chirped FBGs, the second of which has GVD of -159 ps/nm at frequency of 28 GHz with bandwidth of 1.5 GHz, the electrical spectrum is shown in Fig. 4.4(c). The first nonlinearly chirped FBG provides a phase shift of π for the complete spectrum and the second chirped FBG only introduces an additional π phase shift for the 3IMD at 28 GHz to make it 2π. With the above time delay of both FBGs, the 2IMD at 9 GHz is suppressed by 33 dB and the 3IMD at 28 GHz is suppressed by 20 dB using the proposed RoF balanced system compared to the conventional OSSB RoF system in Fig. 4.4(a).

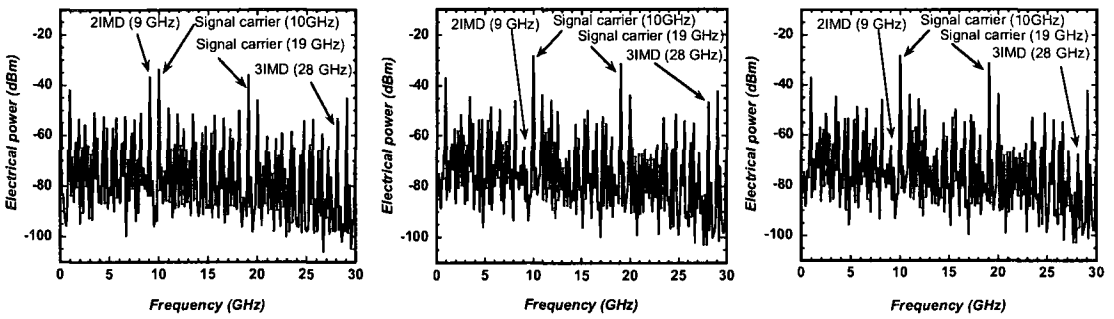

Figure 4.4 Electrical spectra for a back-to-back (a) conventional OSSB RoF system (i.e. upper branch only), (b) proposed RoF balanced system with one FBG, and (c) the same as (b) but using two cascaded chirped FBGs.

4.3.1 BER Analysis

In order to show system performance benefit by using the proposed RoF balanced system, the simulated BER at 10^{-9} are compared among the three systems described below to show receiver sensitivity improvement due to the reduced second order nonlinear distortion and reduced RIN. 3HD suppression will not be considered with nonlinearly chirped FBG in the BER simulations, because the EAM used has larger second order nonlinearity. The three systems considered for comparison are; the "ideal" RoF balanced system, i.e. the proposed RoF balanced system with a linear EAM, in which nonlinear distortion is not introduced and a 3 dB RIN reduction is achieved due to balanced detection, the proposed RoF balanced system with a nonlinear EAM, where nonlinear distortion is introduced and 3 dB RIN reduction is achieved; and the conventional OSSB RoF system with a nonlinear EAM, where nonlinear distortion is introduced, but 3 dB RIN reduction is not obtained because of single photodiode

detection. The EAM is driven with 2.5 Gb/s BPSK data. Comparison of the three back-to-back RoF systems with optical subcarriers at 10 and 35 GHz are shown in Fig. 4.5(a) and Fig. 4.5(b), respectively. Only one nonlinearly chirped FGB is used with GVD of -625 and -156 ps/nm at frequency of 10 and 20 GHz with bandwidth of 50 GHz for the optical subcarrier at 10 GHz. For the optical subcarrier at 35 GHz, GVD is -52 and -13 ps/nm at frequency of 35 and 70 GHz with bandwidth of 100 GHz. As seen in Fig. 4.5, the conventional OSSB RoF system is degraded in receiver sensitivity by a power penalty of 4.1 (2.05) dB for optical subcarrier at 10 (35) GHz compared to proposed RoF balanced system with a linear EAM. However, the proposed RoF balanced system with subcarrier at 10 (35) GHz improves receiver sensitivity by 1.5 (1.7) dB compared to the conventional OSSB RoF system.

The residual power penalty in the proposed balanced system is due to 3HD and $\psi \neq 0$, and because of independent shot noise in the balanced detector and laser phase noise. Note, because different optical signal subcarrier frequencies lead to increases or decreases in 3HD generation for the same bias, it is observed that an optical modulation depth of ~1 dB greater for optical subcarrier at 35 GHz than for 10 GHz due to different settings of optimal biases to better suppress 3HD. Also a better reduction of the 2HD and 3HD for the optical subcarrier at 35 GHz is achieved due to further separation from the optical carrier. This results in a better BER performance at 35 GHz.

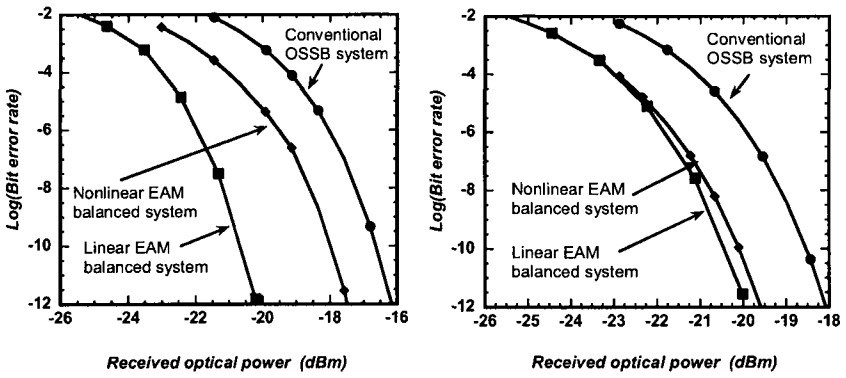

(a) (b)

Figure 4.5 Simulated back-to-back BER versus received optical power for OSSB RoF system (black circle), proposed balanced RoF system with a nonlinear EAM (black diamond) and proposed balanced RoF system with a linear EAM (black square) with subcarrier frequencies at (a) 10 GHz and (b) 35 GHz. Only one FBG is used in the lower branch.

Next the three systems with 25 km of SMF are compared. Note that a larger GVD of the nonlinearly chirped FBG is required to compensate for fiber dispersion besides phase shift. For the optical subcarrier at 10 GHz, the nonlinearly chirped FGB used has GVD of -1025 and -556 ps/nm with respect to the optical carrier at frequency of 10 and 20 GHz with bandwidth of 50 GHz. For the optical subcarrier at 35 GHz, GVD becomes -452 and -413 ps/nm at frequency of 35 and 70 GHz and bandwidth of 100 GHz. As seen in Fig. 4.6, the conventional OSSB RoF system is degraded in receiver sensitivity by a power penalty of 3.1 (2.1) dB for the optical subcarrier at 10 (35) GHz compared to the proposed balanced RoF system with the linear EAM. However, the proposed balanced RoF system with the optical subcarrier at 10 (35) GHz using the nonlinear EAM improves receiver sensitivity by 1.2 (1.3) dB at 10 (35) GHz as compared to the conventional OSSB RoF system. Moreover, by comparing Fig. 4.6 with Fig. 4.5 it is found that the proposed balanced system is degraded by chromatic dispersion from the

transmission fiber. The reason is that fiber dispersion also contributes to harmonic and intermodulation distortions. The EAM bias remains fixed between the back-to-back and through 25 km of fiber transmission, so there is slightly reduced performance in the case of 25 km fiber transmission.

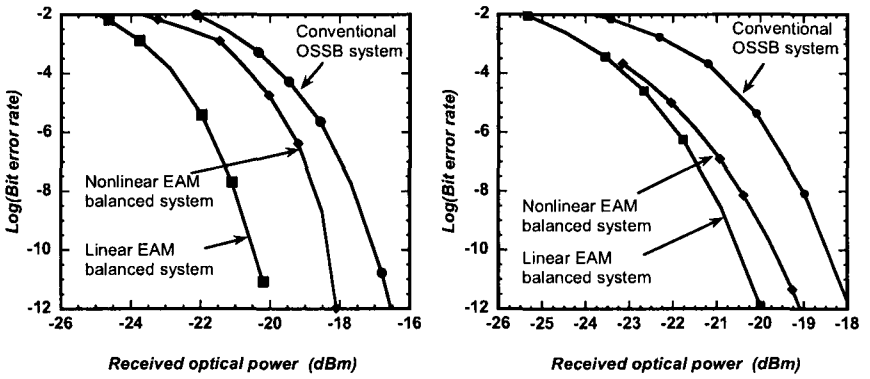

(a) (b)

Figure 4.6 Corresponding to Fig. 4.5, but with 25 km of SMF used instead of a back-to-back system.

4.3.2 Relative Intensity Noise Analysis

Figure 4.7 below shows the performance of a conventional OSSB versus the tunable FBG balanced system pertaining to RIN reduction. Usually the RIN has a resonant peak at the same frequency as the carrier-photon resonance of the laser. A low RIN is critical in high speed and analog systems. This is usually achieved by increasing the output power of the laser, which leads to increases in nonlinear distortions or in this case using balanced detection to reduce nonlinear distortion. The simulation used optical subcarrier frequency tone of 10 GHz, SMF length of 25 km and laser linewidth of 800 KHz. The results show

for frequency component of 10 GHz the RIN reduction is approximately 3 dB. The simulation parameters are the same as those described in section 4.3.

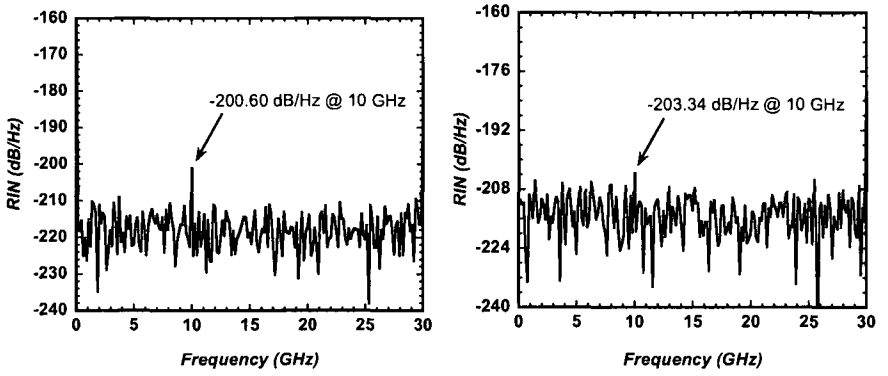

(a) (b)

Figure 4.7 Relative intensity noise with the use of 25 km of SMF and subcarrier frequency of 10 GHz for (a) conventional OSSB RoF system and (b) proposed tunable FBG balanced system.

4.4 Conclusion

The proposed tunable FBG balanced system has been presented in this chapter, where it is capable of suppressing both second and third order nonlinear distortion, yet there are minimal restrictions on the EAM bias used. This allows the selection of a bias that optimizes the optical RF signal subcarrier power. The proposed balanced system is cost effective because of the use of only one optical modulator. It was shown by simulation that the proposed balanced system is effective in the reduction of 2HD, 2IMD, 3HD, 3IMD and RIN. Furthermore, the proposed balanced system makes use of double sideband transmission and yet is only minimally affected by periodic power fading. The suppressed nonlinear distortions allow for improved receiver sensitivity and reduced

multi-subcarrier interference. As a result, more communication channels may be added to a given optical carrier making the RoF system more efficient. Simulated results show a suppression of second and third order harmonic distortion of 25.4 dB and 2.6 dB, respectively and for the case of second and third intermodulation distortion suppression of 33 dB and 20 dB, respectively have been reported. Simulation also shows that the receiver sensitivity improvement is approximately 2.5 dB at BER of 10^{-9} for optical subcarrier at 10 and 35 GHz and RIN is suppressed by 3 dB.

Unfortunately, the proposed balanced system still makes use of ODSB transmission, which is not spectrally efficient as OSSB transmission.

Chapter 5

5 Proposed Asymmetric OSSB Mach-Zehnder Modulator

5.1 Introduction

The motivation for the following linearized modulator is to develop a linearized modulator that not only suppresses nonlinear distortion, but also makes use of OSSB modulation. In published literature [68-69], authors mainly addressed the linearity issue and neglected to consider power fading and spectral efficiency described in Chapter 2. Also, third order nonlinear distortion components lie closest to the optical subcarrier and are more difficult to filter out. Because of this the preceding linearization technique will work at suppressing third order distortion, which will improve SFDR and BER.

Presented in this chapter is the proposed asymmetric OSSB Mach-Zehnder modulator, which is capable of suppressing third order distortion and provide OSSB modulation and as a direct result SFDR is improved. The proposed linearized modulator is compared to the dual-parallel MZM and the conventional MZM in terms of SFDR and BER performance.

This chapter is organized as follows; Section 5.2 will introduce and describe the proposed asymmetric OSSB Mach-Zehnder modulator, Section 5.3 will compare simulated RF spectra to show that the proposed technique indeed suppresses third order distortion. Also shown is the sensitivity analysis to the voltage splitting ratio and optical

phase mismatch before optical coupling, Section 5.4 will compare SFDR and BER between the proposed, dual-parallel and conventional MZM and in Section 5.5 some conclusions will be drawn.

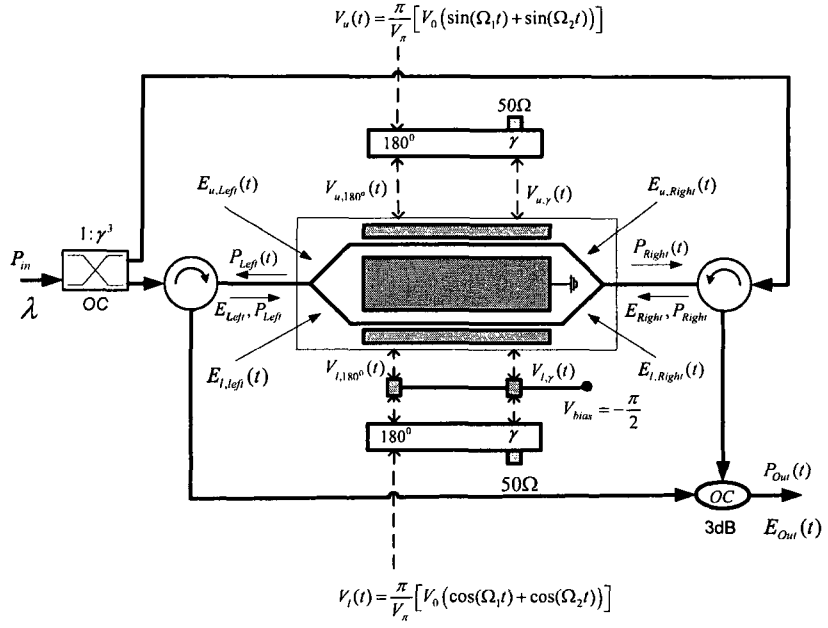

Figure 5.1 The proposed asymmetric OSSB Mach-Zehnder modulator using a dual-electrode MZM, which is optically bidirectionally fed [70].

The proposed asymmetric OSSB MZM is shown in Fig. 5.1, which is comprised mainly of a dual-electrode MZM, two optical circulators and a 3 dB optical combiner. It is seen that a CW light is injected bidirectionally into the two optical ports with a power splitting ratio of $1:\gamma^3$, $\gamma>1$. The two lights travels through the MZM bidirectionally and then the two outputs via optical circulators are combined with a 3 dB optical combiner. Transmitted RF signals are first divided into two parts and relatively phase shift by $\pi/2$ from each other, then each passes through a 180^0 hybrid electrical coupler (HEC) and the two outputs of each hybrid coupler are inputs to the two RF input ports with a voltage

splitting ratio of $1:\gamma$. The MZM is biased at quadrature, in order to facilitate the generation of OSSB modulation. It is obvious that optical field in each direction experiences two co- and two counter- propagating electric fields induced by the RF signals. When the optical field co-propagates with the RF signal, optical modulation occurs just like in a normal MZM. However, it was shown that modulation efficiency is severely reduced by greater that 20 dBc, when the optical field counter-propagates with the RF signal induced electric field for RF greater than 2 GHz [71]. Therefore, the counter-modulation response of a MZM can be neglected for RFs beyond 2 GHz. Suppose that two RF signals with frequencies of Ω_1 and Ω_2, both larger than 2 GHz, drive the two HECs simultaneously. The two driving voltages for the upper and lower HECs can be written, in a normalized form, as $V_u(t) = \pi\left[V_0\left(\sin(\Omega_1 t)+\sin(\Omega_2 t)\right)\right]/V_\pi$ and $V_l(t) = \pi\left[V_0\left(\cos(\Omega_1 t)+\cos(\Omega_2 t)\right)\right]/V_\pi$, where V_0 is the RF signal voltage magnitude and V_π is the half wave switching voltage of the MZM. So the RF signals appearing at the two output ports are $V_{u,180^0}(t) = -m(\sin(\Omega_1 t)+\sin(\Omega_2 t))$ and $V_{u,\gamma}(t) = \gamma m(\sin(\Omega_1 t)+\sin(\Omega_2 t))$ for the upper HEC and $V_{l,180^0}(t) = -m(\cos(\Omega_1 t)+\cos(\Omega_2 t))-\pi/2$, and $V_{l,\gamma}(t) = \gamma m(\cos(\Omega_1 t)+\cos(\Omega_2 t))-\pi/2$ for the lower HEC as shown in Fig. 5.1, where $m = \pi V_0/V_\pi$ is the modulation index.

The output electric fields emitting from the left side optical port of the MZM just before reaching the MZM's optical coupler is $E_{u,Left}(t) = E_{Right}\left[e^{j\gamma m(\sin(\Omega_1 t)+\sin(\Omega_2 t))}\right]e^{j\omega t}/\sqrt{2}$ for the upper branch and $E_{l,Left}(t) = E_{Right}\left[e^{j(\gamma m(\cos(\Omega_1 t)+\cos(\Omega_2 t))-\pi/2)}\right]e^{j\omega t}/\sqrt{2}$ for the lower branch, where ω is the optical angular frequency. Similarly, the output electric fields emitting from the right side optical port are given by $E_{u,Right}(t) = E_{left}\left[e^{-jm(\sin(\Omega_1 t)+\sin(\Omega_2 t))}\right]e^{j\omega t}/\sqrt{2}$ for the

upper branch and $E_{l,Right}(t) = E_{left}\left[e^{-j\{m(\cos(\Omega_1 t)+\cos(\Omega_2 t))+\pi/2\}}\right]e^{j\omega t}/\sqrt{2}$ for the lower branch. E_{Left} and E_{Right} are the output electric field amplitudes for the optical light applied to the left and right side optical ports of the MZM. The total output electric field at the output of the optical combiner is then given by,

$$E_{Out}(t) = \frac{1}{\sqrt{2}}\begin{bmatrix} E_{left}\left[e^{-jm(\sin(\Omega_1 t)+\sin(\Omega_2 t))} - je^{-jm(\cos(\Omega_1 t)+\cos(\Omega_2 t))}\right]+ \\ E_{Right}\left[e^{j\gamma m(\sin(\Omega_1 t)+\sin(\Omega_2 t))} - je^{j\gamma m(\cos(\Omega_1 t)+\cos(\Omega_2 t))}\right] \end{bmatrix} e^{j\omega t}. \quad (5.1)$$

Using the Jacobi-Auger expansion and considering first-order terms only, (5.1) can be expressed by,

$$E_{Out}(t) \approx \frac{1}{\sqrt{2}}\begin{bmatrix} E_{left}\begin{bmatrix} J_1(m)\left(e^{-j\Omega_1 t}+e^{-j\Omega_2 t}\right) - J_1(m)\left(e^{j\Omega_1 t}+e^{j\Omega_2 t}\right)- \\ J_1(m)\left(e^{j\Omega_1 t}+e^{j\Omega_2 t}\right) - J_1(m)\left(e^{-j\Omega_1 t}+e^{-j\Omega_2 t}\right) \end{bmatrix} \\ +E_{Right}\begin{bmatrix} J_1(\gamma m)\left(e^{j\Omega_1 t}+e^{j\Omega_2 t}\right) + J_1(\gamma m)\left(e^{j\Omega_1 t}+e^{j\Omega_2 t}\right)- \\ J_1(m)\left(e^{-j\Omega_1 t}+e^{-j\Omega_2 t}\right) + J_1(m)\left(e^{-j\Omega_1 t}+e^{-j\Omega_2 t}\right) \end{bmatrix} \end{bmatrix} e^{j\omega t}$$

$$\approx \frac{2}{\sqrt{2}}\left[-E_{left}\left(J_1(m)\right) + E_{Right}\left(J_1(\gamma m)\right)\right]\left(e^{j(\omega+\Omega_1)t}+e^{j(\omega+\Omega_2)t}\right), \quad (5.2)$$

where $J_1(\ )$ is the first order Bessel function. Note, that only the upper sideband exists as seen by the term $\left(e^{j(\omega+\Omega_1)t}+e^{j(\omega+\Omega_2)t}\right)$ in (5.2), hence one obtains OSSB modulation.

5.2 Analysis of Suppression of Third Order Distortion

To verify the above theory, a RoF system was modeled using such a modulator driven by two sinusoidal RF signals at 10 and 12 GHz. The simulated output optical spectrum is shown in Fig. 5.2 for a RoF system using the proposed modulator with γ=1.9 for (a) and γ=2.8 for (b). Furthermore, this linearization technique induces an ~ 10 dB RF subcarrier power loss that will be discussed later in this Chapter. Therefore, the RF power level was increased by ~ 10 dB for the proposed modulator with optimally set voltage splitting ratio, so that constant detected RF subcarrier power was received in both cases, allowing for a fair comparison. It is observed that only the upper sideband of the two optical subcarrier components at 10 and 12 GHz exists, i.e. OSSB modulation, in addition to other distortion components. Also it is seen that two IMDs at 8 and 14 GHz in Fig. 5.2(a) are close to the two optical subcarriers. Thus, the two IMDs are detrimental to both the optical subcarriers. Therefore it is desirable that these IMDs be suppressed. Figure 5.2(a) with a non-optimal value of voltage splitting ratio $\gamma = 1.9$ shows a carrier to triple beat (CTB) of -20.4 dBc and Fig. 5.2(b) with an optimal value $\gamma = 2.8$ shows a CTB of -39.2 dBc. This shows that an improvement in CTB of approximately 19 dB is obtained.

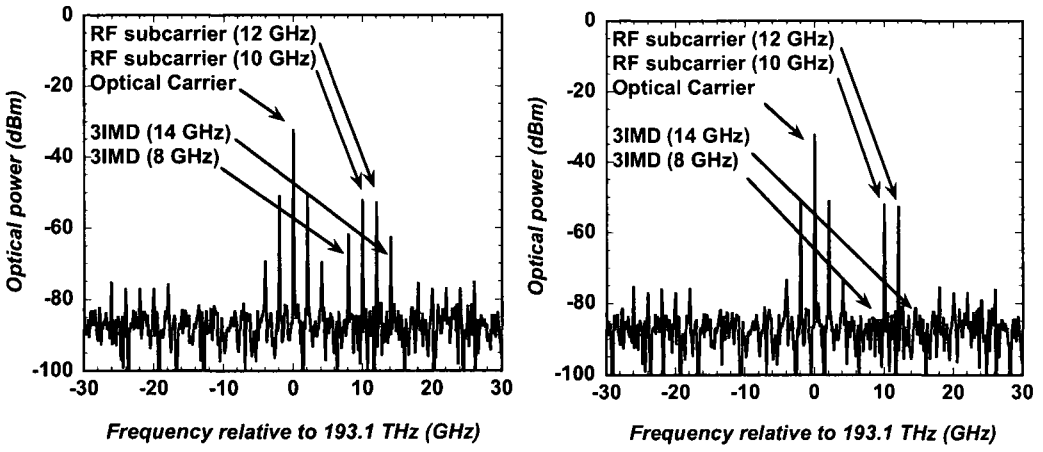

Figure 5.2 Optical spectra for the proposed asymmetric OSSB MZM with (a) RF voltage ratio $\gamma = 1.9$, i.e. not optimally set; and (b) $\gamma = 2.8$, i.e. optimally set for the suppression of nonlinear distortion.

To show the cancellation of 3IMD, the combined optical power was investigated. The optical power emitted from the left side optical port of the MZM just before reaching the left optical circulator is $P_{Left}(t) = P_{Right}\left[1 - \sin\left(\frac{\pi\gamma(V_u(t) - V_l(t))}{V_\pi}\right)\right]/2$ and optical power emitted from the right side optical port of the MZM just before reaching the right optical circulator is $P_{Right}(t) = P_{Left}\left[1 + \sin\left(\frac{\pi(V_u(t) - V_l(t))}{V_\pi}\right)\right]/2$. The total combined optical power is given by $P_{Out}(t) = \left[P_{Left}(t) + P_{Right}(t)\right]/2$. Considering the above, the output optical power is obtained in detail as $P_{Out}(t) = \frac{1}{2}\left[P_{Left}\left[1 + \sin\left(\frac{\pi(V_u(t) - V_l(t))}{V_\pi}\right)\right] + P_{Right}\left[1 - \sin\left(\frac{\pi\gamma(V_u(t) - V_l(t))}{V_\pi}\right)\right]\right]$. Using the Taylor series approximation until the third term, the output optical power is obtained and given

by, $P_{Out}(t) \approx \frac{1}{2}\left[\begin{array}{l} P_{Left}\left(1+\frac{\pi\left(V_u(t)-V_l(t)\right)}{V_\pi}-\frac{1}{6}\left(\frac{\pi\left(V_u(t)-V_l(t)\right)}{V_\pi}\right)^3\right) \\ +P_{Right}\left(1-\frac{\pi\gamma\left(V_u(t)-V_l(t)\right)}{V_\pi}+\frac{1}{6}\left(\frac{\pi\gamma\left(V_u(t)-V_l(t)\right)}{V_\pi}\right)^3\right)\end{array}\right]$. By simple mathematical manipulation, the expression for the output optical power is simplified into

$$P_{Out}(t) \approx \frac{1}{2}\left[P_{Left}+P_{Right}+\frac{\pi\left(V_u(t)-V_l(t)\right)}{V_\pi}\left(P_{Left}-\gamma P_{Right}\right)-\frac{1}{6}\left(\frac{\pi\left(V_u(t)-V_l(t)\right)}{V_\pi}\right)^3\left(P_{Left}-\gamma^3 P_{Right}\right)\right], \quad (5.3)$$

where the fourth term is related to the third order nonlinear distortion, which can be approximately cancelled if the condition of $P_{Left}/P_{Right}=\gamma^3$ is satisfied, where P_{Left} and P_{Right} are the unmodulated optical power applied to the left and right optical ports of the MZM, respectively. Considering the condition of $P_{Right}=P_{Left}/\gamma^3$, the following is obtained $P_{Out}(t) \approx \frac{1}{2}P_{Left}\left[\left(1+\frac{1}{\gamma^3}\right)+\frac{\pi\left(V_u(t)-V_l(t)\right)}{V_\pi}\left(1-\frac{1}{\gamma^2}\right)\right]$, where the average optical power for the optical carrier is $P_{carrier}=\frac{P_{Left}}{2}\left(1+\frac{1}{\gamma^3}\right)$ and the optical subcarrier power for the RF signal is $P_{RFsub}=\frac{P_{Left}}{2}\frac{\pi V_0}{V_\pi}\left(1-\frac{1}{\gamma^2}\right)$. This leads to a linearized modulation index of $m_{lin}=\frac{P_{RFsub}}{P_{carrier}}=\frac{\frac{P_{Left}}{2}\frac{\pi V_0}{V_\pi}\left(1-\frac{1}{\gamma^2}\right)}{\frac{P_{Left}}{2}\left(1+\frac{1}{\gamma^3}\right)}=m\frac{\gamma(\gamma-1)}{1-\gamma+\gamma^2}$. The relationship for the linearized modulation index normalized with the unlinearized modulation index is given by

$$\frac{m_{lin}}{m}=\frac{\gamma(\gamma-1)}{1-\gamma+\gamma^2}. \quad (5.4)$$

5.3 Sensitivity Analysis

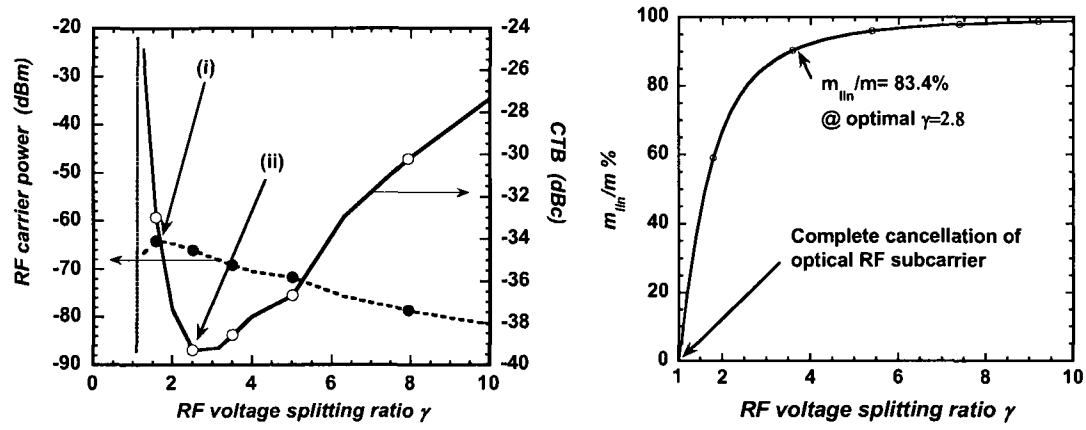

(a) (b)

Figure 5.3 (a) Simulated RF carrier power (dashed) and suppression of CTB (solid) versus RF voltage splitting ratio γ; and (b) m_{lin}/m calculated by (5.4) versus RF voltage splitting ratio γ. Note, (i) indicates maximum RF carrier power at γ=1.9, and (ii) optimum suppression of CTB at γ=2.8.

(5.4) shows that m_{lin}/m is always less than unity for $\gamma>1$. This suggests that the suppression of 3IMD will also lead to a decrease of optical modulation index. In other words, the optical subcarrier power for the RF signal is also suppressed with the suppression of 3IMD. Using the linearized optical modulation index to express the real optical modulation index, it is seen that the linearized optical modulation index is decreased by a factor of $\gamma(\gamma-1)/\left(1-\gamma+\gamma^2\right)$ due to linearization, which is the same as in the dual-parallel MZM [44]. Figure 5.3(a) shows the simulated RF carrier electrical power and suppression of CTB with RF splitting voltage ratio γ. It is seen that the maximum RF carrier power is obtained at $\gamma=1.9$ and the maximum suppression of CTB is obtained at $\gamma=2.8$. Thus, the maximum RF carrier power and linearization are not obtained

simultaneously. Figure 5.3(b) shows the ratio of m_{lin}/m in percentage versus γ. It is obvious that with the increase of γ, the linearized optical modulation index approaches the unlinearized optical modulation index. This suggests that the proposed linearized MZM in Fig. 5.1 is equivalent to the conventional MZM, if γ is very high, such as 10.

Only considering terms of up to the third order, (5.3) represents the summation of the left and right modulated optical powers emitted from the MZM, where it is assumed that an "ideal" MZM is used. If a non-ideal MZM is considered, then a phase difference of $\Delta\varphi$ between $P_{Left}(t)$ and $P_{Right}(t)$ exists before the 3 dB optical combiner, which leads to a phase imbalance between the bidirectional transmissions of the proposed linearized MZM. The optical output power after the optical coupler is now given by,

$$P_{Out}(t) \approx \frac{1}{2}\left[P_{Left} + P_{Right} + m_{lin}\left(P_{Left} - \left(\gamma + \frac{\Delta\varphi}{m_{lin}}\right) P_{Right} \right) - \frac{1}{6}(m_{lin})^3 \left(P_{Left} - \left(\gamma + \frac{\Delta\varphi}{m_{lin}}\right)^3 P_{Right} \right) \right], \quad (5.5)$$

where $m_{lin} = \pi(V_u(t) - V_l(t))/V_\pi$ is the linearized modulation index. Substituting the ideal condition for 3IMD cancellation of $P_{Right} = P_{Left}/\gamma^3$ and normalizing with respect to P_{Left} in (5.5), then the normalized optical output power is obtained as, $P_{Out,norm}(t) \approx \frac{1}{2}\left[\left(1 + \frac{1}{\gamma^3}\right) + m_{lin}\left(1 - \frac{1}{\gamma^3}\left(\gamma + \frac{\Delta\varphi}{m_{lin}}\right)\right) - \frac{1}{6}(m_{lin})^3 \left(1 - \frac{1}{\gamma^3}\left(\gamma + \frac{\Delta\varphi}{m_{lin}}\right)^3\right)\right]$, where the component proportional to m_{lin} is the optical subcarrier power, P_{RFsub} for the RF signal, the component proportional to m_{lin}^3 is the optical 3IMD power, P_{3IMD} and the final component is the optical carrier power, $P_{carrier}$. Considering square-law photodetection, the normalized electrical power for the RF signal is $P_{RF,elec,norm} \approx \left[\frac{1}{2} m_{lin}\left(1 - \frac{1}{\gamma^3}\left(\gamma + \frac{\Delta\varphi}{m_{lin}}\right)\right)\right]^2$ and electrical

power for the 3IMD is $P_{3IMD,elec,norm} \approx \left[-\frac{1}{12}(m_{lin})^3 \left(1 - \frac{1}{\gamma^3}\left(\gamma + \frac{\Delta\varphi}{m_{lin}} \right)^3 \right) \right]^2$. To obtain the expression of SFDR, it is required to solve the equation for $P_{3IMD,elec,norm}$ =noise floor, for m_{lin}. Then the SFDR is obtained by the difference between $P_{RF,elec,norm}$ and the noise floor, where it will become a function of $\Delta\varphi$. Utilizing © Mathematica 6.0 and solving $\left[-\frac{1}{12}(m_{lin})^3 \left(1 - \frac{1}{\gamma^3}\left(\gamma + \frac{\Delta\varphi}{m_{lin}} \right)^3 \right) \right]^2$ = noise floor, for m_{lin}, one real solution is obtained, i.e. $m_{lin} = \frac{\Delta\varphi}{\gamma\sqrt{3}}$, which leads to the expression of SFDR related to $\Delta\varphi$,

$$SFDR[dB] = -10\log\left[P_{Left} \frac{\left(6 + \sqrt{3} - \sqrt{3}\gamma^2\right)^2 \Delta\varphi^2}{36\gamma^6} \right]. \tag{5.6}$$

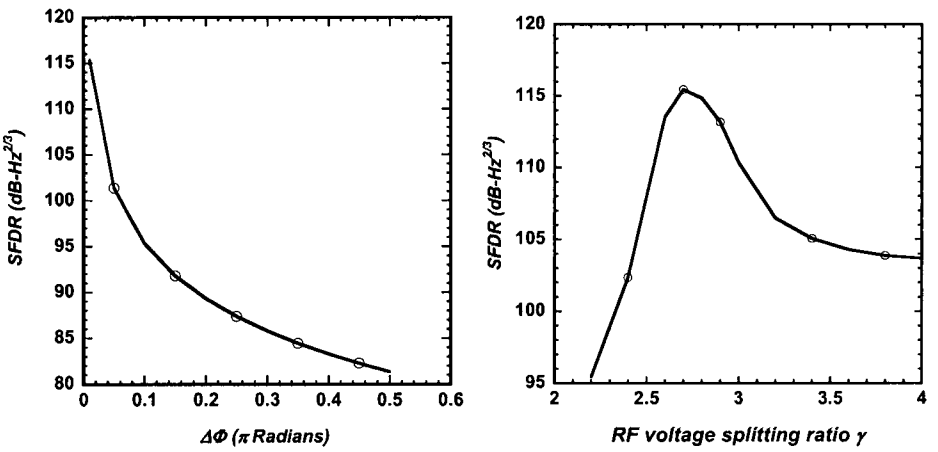

(a) (b)

Figure 5.4 (a) SFDR versus $\Delta\varphi$ with a voltage splitting ratio $\gamma = 2.8$ and (b) SFDR versus γ with a phase difference $\Delta\varphi = 0.05$ for the proposed asymmetric OSSB MZM, where P_{Left} = 19 mW.

If one lets $\gamma = 2.8$ and scales using $P_{Left} = 19$ mW in (5.6), then $SFDR\ [\text{dB}] = -10\log\left[2.352\times10^{-6}\Delta\varphi^{2}\right]$ is obtained. Figure 5.4(a) shows the SFDR versus $\Delta\varphi$ for the proposed asymmetric OSSB MZM. It is seen that SFDR decreases with the increase of $\Delta\varphi$. Note, in theory as $\Delta\varphi \to 0$ the best linearization is achieved and for $\Delta\varphi = \pi$, no linearization is obtained at all, i.e. as in the conventional MZM. If $\Delta\varphi \to 0$, the optical power from the bidirectional transmissions are added and 3IMD components are out of phase, such that the suppression of 3IMD is achieved. On the contrary, if the bidirectional optical transmissions have a phase shift of π from each other, then the components of 3IMD from the two transmissions are in phase and cannot be cancelled. Note Fig. 5.4(a) also applies to the dual-parallel MZM. Fig. 5.4(b) shows the SFDR versus γ for the proposed technique and it is seen that the maximum SFDR occurs approximately at a voltage splitting ratio of $\gamma = 2.8$ and drops off as it deviates from this optimal value. This suggests that the 3IMD suppression is sensitive to the phase imbalances between bidirectional transmissions and the voltage splitting ratio.

5.4 SFDR and BER Analysis

To analyze the effectiveness of the proposed modulator, RoF systems are simulated using a conventional OSSB MZM, dual-parallel OSSB MZM similar to [44] and the proposed asymmetric OSSB MZM with $\gamma = 2.8$. A CW laser set to 1550 nm with a linewidth of 800 KHz and relative intensity noise (RIN) of -150 dB/√Hz is used. The MZM has a half wave switching voltage of 5 V, 20 dB extinction ratio and an insertion loss of 6 dB for all the three modulators. The optical power injected into the modulator is kept the same at 19

dBm. The link will carry three RF subcarriers at 9, 10 and 12 GHz. The 3IMD at 11 GHz is most detrimental to the center channel of 10 GHz. Therefore, it will be considered in the measurement of 3IMD suppression for these comparisons. The PIN responsivity of 1.0 A/W and thermal noise of 10^{-12} A/√Hz are considered with a noise bandwidth of 3 GHz for each of the RF carriers. Two scenarios will be considered; a back-to-back system and a system with the use of 20 km of standard single mode fiber (SMF) to compare the proposed with the other two modulators. The SMF has an attenuation of 0.2 dB/km and chromatic dispersion of 16 $ps/(nm \cdot km)$. The simulated SFDR is shown in Fig. 5.5. Specifically, simulated SFDR in a back-to-back system using the proposed asymmetric MZM, the dual-parallel MZM, and conventional MZM is shown in Fig. 5(a); and correspondingly simulated SFDR in a system with the use of 20 km of SMF is shown in Fig. 5.5(b). The linearization losses have been compensated for by increasing the input RF signal power appropriately, so to allow for a fair comparison.

For the back-to-back case, the proposed asymmetric MZM, the dual-parallel MZM and the conventional MZM result in a SFDR of 98 $dB \cdot Hz^{4/5}$, 102 $dB \cdot Hz^{2/3}$ and 115 $dB \cdot Hz^{2/3}$ in Fig. 5.5(a), respectively. Thus, for the back-to-back system the proposed asymmetric MZM leads to a SFDR improvement of 13 dB and 17 dB over the dual-parallel and the conventional MZM, respectively. The physical reason for the 13 dB SFDR improvement in using this proposed MZM compared to the dual-parallel MZM is because the proposed MZM makes use of only one optical modulator. In other words, the proposed design does not have to deal with the different optical characteristics of two independent optical modulators. On the contrary, two different frequency responses for the two independent MZMs in the dual-parallel MZM degrade 3IMD suppression [44].

In the case where 20 km of SMF is used, the proposed MZM, the dual-parallel MZM and the conventional MZM result in a SFDR of 96 $dB{\cdot}Hz^{4/5}$, 100 $dB{\cdot}Hz^{2/3}$ and 113 $dB{\cdot}Hz^{2/3}$ in Fig. 5.5(b), respectively. Therefore, for this case the proposed MZM leads to a SFDR improvement of 13 and 17 dB over the dual-parallel and the conventional MZM, respectively. The two-tone test at RFs of 10 and 12 GHz was also simulated, where the linearized modulators showed a slight increase in SFDR of 1 and 1.5 dB for the back-to-back and 20 km of SMF cases, respectively. The conventional modulator showed an increase of 1.5 and 2.5 dB for the back-to-back and 20 km of SMF cases, respectively. Despite the increase in SFDR for the individual modulators, the relative improvement in SFDR remained basically the same for a light carrying two or three RF tones.

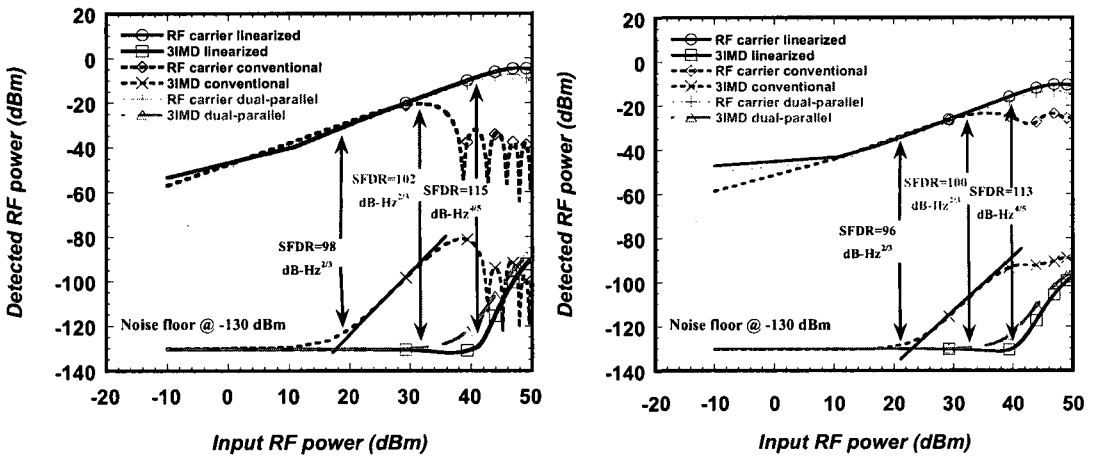

(a) (b)

Figure 5.5 Simulated spurious free dynamic range for a RoF system using the asymmetric OSSB MZM, dual-parallel OSSB MZM and conventional OSSB MZM for a (a) back-to-back and (b) through 20 km of SMF.

The suppression of IMD will also lead to an improvement of BER. Here an electrical ASK 2.48 Gb/s data signal carried by each RF carrier located 10 and 12 GHz was considered. Fig. 5.6 shows the simulated BER for the link using the three modulators. The injected optical power is kept the same for all three modulators in the simulation, so that the average optical power injected into the SMF is the same. Furthermore, RF driving power is adjusted, such that the modulation index is the same for all three cases and then kept constant. So the modulated light injected into the SMF would have similar BER after the photodetector, if no nonlinear distortion components are added by the respective modulators. An optical attenuator was inserted just before the photodetector to vary the received optical power at the photodetector in order to attain the BER measurements. The improvement in BER for the proposed technique is because of improved receiver sensitivity due to the suppression of 3IMD products. As shown in Fig. 5.6 it is found that the proposed MZM induces a receiver sensitivity improvement of 7 and 4.3 dB at a BER=10^{-9}, compared to the conventional MZM and the dual-parallel MZM, respectively.

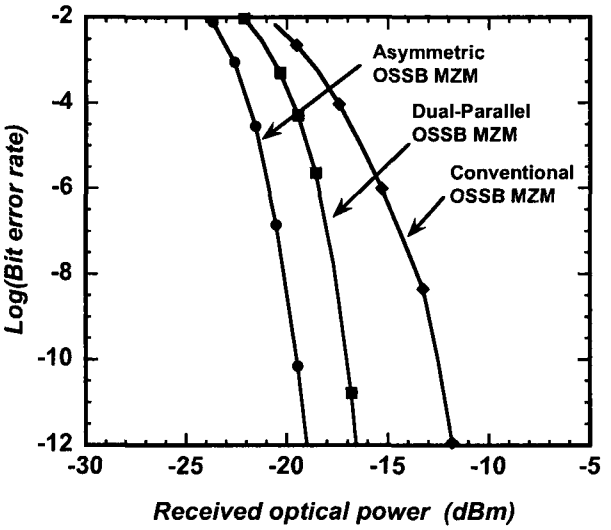

Figure 5.6 BER for a RoF system with 20 km SMF transmission using a conventional, dual-parallel and asymmetric OSSB MZM, respectively.

5.5 Conclusion

The proposed asymmetric OSSB Mach-Zehnder modulator suppresses third order nonlinear distortion and produces OSSB modulation. The proposed design outperformed the dual-parallel MZM and conventional MZM in SFDR and BER. It is found that a relative SFDR improvement of 13 and 17 dB is achieved in comparison to the dual-parallel MZM and the conventional MZM, respectively. Compared to the dual-parallel MZM, the advantage of this proposed modulator is that only one MZM is used and thus suppression of 3IMD is improved and cost is reduced. This is because the effects of two independent frequency responses due to the dual MZMs are removed and phase imbalances between the bidirectional transmissions can be maintained minimal for the proposed modulator. On the contrary it is very difficult to obtain a minimal phase

imbalance between two independent MZMs for the dual-parallel MZM. Furthermore, because of the linearization process, the RF carrier power is reduced.

Of course, this proposed asymmetric OSSB MZM does increase system complexity and RF of less than 2 GHz may not be used due to non-negligible crosstalk between the bidirectional transmissions. Also the modulation indices need to be maintained equal for optimal performance. This has become the motivation for the final proposed technique presented in Chapter 6, where the new proposed technique will not depend on modulation index and any RF may be used. Also there will be a reduction in design complexity.

Chapter 6

6 Proposed Mixed-Polarization OSSB Mach-Zehnder Modulator

6.1 Introduction

For the proposed asymmetric OSSB Mach-Zehnder modulator presented in Chapter 5, it was noted that the RF carrier frequency is required to be above 2 GHz to reduce the effects of crosstalk between the bidirectionally modulated optical signals. The modulation index needs to match for the upper and lower applied RF signals at the respective electrodes. Also there is a desire to reduce complexity so that the linearization modulator may be incorporated into one silicon substrate or module for practical purposes.

These motivational ideas lead to the final proposed mixed-polarization OSSB Mach-Zehnder modulator. Of course the proposed modulator needs to retain the use of OSSB transmission as described for the asymmetric OSSB Mach-Zehnder modulator in Chapter 5. The objective in this chapter is to design a linearized modulator whose performance does not depend on modulation index, the 2 GHz RF limitation is removed and complexity is reduced, so that it may be incorporated on one silicon substrate or module. The proposed mixed-polarization OSSB Mach-Zehnder modulator will be compared to the conventional MZM in terms of SFDR, 3IMD suppression and overall reduction of nonlinear distortion components.

This chapter is organized as follows; Section 6.2 will describe the proposed mixed-polarization OSSB Mach-Zehnder modulator, Section 6.3 will provide the equation development for the SFDR and report on the sensitivity analysis due to polarization angle and electro-optic coefficient ratio errors, Section 6.4 will provide simulated third order suppression results, SFDR results and a comparison analysis to the conventional MZM, Section 6.5 will explore experimental SFDR and a comparison analysis to the conventional MZM, and Section 6.6 will finally provide concluding remarks.

6.2 Proposed Mixed-Polarization OSSB Mach-Zehnder Modulator

In Chapter 2 a technique that suppresses IMD was proposed called the mixed-polarization phase modulator, which consists of two linear polarizers placed before and after an optical phase modulator. This linearized phase modulator uses a forward-feed loop with heterodyne detection [63]. However, this technique is limited to optical double sideband modulation. Also because this technique transmits phase modulated light, the use of coherent homodyne or heterodyne detection is required, which is subject to sinusoidal nonlinearities [63, 72]. Furthermore, it uses an acousto-optic frequency shifter for coherent heterodyne detection, which limits the RF bandwidth of the system and increases the cost and complexity. Also explained in Chapter 2 was that optical single sideband (OSSB) modulation is more preferable in analog RoF systems, because for optical double sideband transmission, fiber chromatic dispersion induces signal power fading at periodic intervals of fiber length.

However, when multiple RF tones are applied to the modulator and particularly with high modulation index, many harmonics and intermodulation products are generated due to optical modulation and may lead to dispersion induced power fading and crosstalk even for OSSB modulation. This is because higher order distortion components beat with one another and generated component products that may overlap with or land very close to RF carriers.

In this chapter a theoretical analysis of a RoF system, where a mixed-polarization OSSB MZM is driven by two RF sinusoidal tones is presented. The impact analysis of polarization angle detuning and the electro-optic coefficient ratio on SFDR are investigated. Also investigated is the impact of chromatic dispersion on the RF carrier power and SFDR for the case of two RF tones, which will then be compared to the conventional OSSB modulator. Finally, an experimental verification of the mixed-polarization MZM and measured SFDR is given for a RoF system in a back-to-back and through 20 km of SMF configuration, where this will be compared to the conventional OSSB MZM.

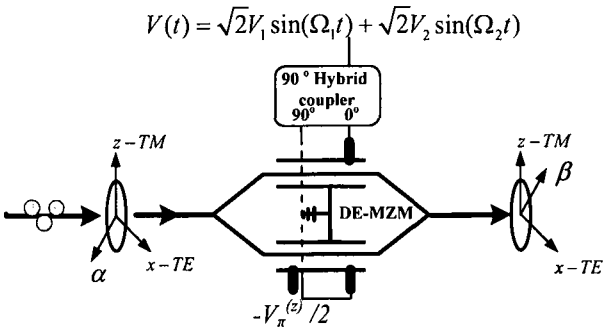

Figure 6.1 The proposed mixed-polarization OSSB MZM (DE-MZM denotes dual electrode MZM) [73].

Figure 6.1 shows the proposed mixed-polarization OSSB MZM, which consists of a linear polarizer adjusted to an angle of α, a z-cut $LiNbO_3$ dual-electrode MZM and a second linear polarizer adjusted to an angle of β. It is well known that the z-cut $LiNbO_3$ MZM exhibits an electro-optic coefficient r_{31} along the x-(TE) axis, which is approximately 1/3 of r_{33} coefficient of the z- (TM) axis [74]. The anisotropy will allow different amounts of modulation depth in the two polarized states. The optical signal entering the modulator passes through a linear polarizer set to an angle α with respect to the z-axis, this will excite a superposition of TE and TM modes that will be modulated to different modulation depths. This will have the effect of allowing the z-(TM) axis carry more IMD, while the x-(TE) axis will carry less IMD. The optical signal is then passed through a second linear polarizer that is angled to β with respect to the z-axis. The two angles are related to one another, but a unique solution does not exist, so they will be selected in such a fashion as to maximize the RF carriers and minimize IMD. By carefully selecting α and β of the two linear polarizers, the combined IMD from the two arms of the MZM can be suppressed.

Two RF sinusoidal tones are applied to the z-cut $LiNbO_3$ MZM electrodes, where the RF tones are phase shifted by 90^0 from each other. The MZM is biased at quadrature and for this case it is assumed that the quadrature biasing is on a downward slope of the MZM response. The normalized voltages applied to the two electrodes are represented by $V_u(t) = m_1 \sin(\Omega_1 t) + m_2 \sin(\Omega_2 t)$ and $V_l(t) = m_1 \cos(\Omega_1 t) + m_2 \cos(\Omega_2 t) - \pi/2$ for the upper and lower electrodes, respectively, where Ω_1 and Ω_2 are the angular frequencies of the two RF tones. Here $m_{1,2} = \frac{\pi}{V_\pi^{(z)}} V_{1,2}$ are the modulation indexes for the z-polarized component of the electric field, where $V_\pi^{(z)}$ is the half-wave switching voltage of the MZM in the z-(TM) axis. The electric field exiting the first linear polarizer and entering the z-cut $LiNbO_3$ MZM is represented by $\bar{\mathbf{E}}_{in}(t) = \sqrt{P_{in}} \left(\hat{z}\cos(\alpha) + \hat{x}\sin(\alpha) \right) e^{j\omega t}$, where P_{in} is the input optical power to the MZM. If birefringence is considered and defined as $\Delta\tau = d\,\Delta n/c$, the time delay between the two orthogonal polarization components, TE and TM, where d is the distance traveled by the light, c is the speed of light in a vacuum and Δn is the birefringence or the difference between the highest and lowest refractive indices in the MZM. Thus, the electric field vectors of the upper and lower electrodes are represented, respectively by

$$\bar{\mathbf{E}}_{u,\alpha}(t) = \sqrt{\frac{P_{in}}{1+\delta^2}} \begin{pmatrix} \hat{z}\cos(\alpha) e^{j\left(m_1 \sin\left[\Omega_1 (t+\Delta\tau)\right] + m_2 \sin\left[\Omega_2 (t+\Delta\tau)\right] \right)} e^{j\omega\Delta\tau} \\ +\hat{x}\sin(\alpha) e^{j\gamma\left(m_1 \sin(\Omega_1 t) + m_2 \sin(\Omega_2 t) \right)} \end{pmatrix} e^{j\omega t}$$

and

$$\bar{\mathbf{E}}_{I,\alpha}(t)=\sqrt{\frac{P_{in}}{1+\delta^2}}\begin{pmatrix}\hat{z}\cos(\alpha)\delta e^{j\left(m_1\cos\left[\Omega_1(t+\Delta\tau)\right]+m_2\cos\left[\Omega_2(t+\Delta\tau)\right]-\pi/2\right)}e^{j\omega\Delta\tau}\\+\hat{x}\sin(\alpha)\delta e^{j\left(\gamma\left(m_1\cos(\Omega_1 t)+m_2\cos(\Omega_2 t)\right)-\pi/2\right)}\end{pmatrix}e^{j\omega t},$$

where $\delta=(\sqrt{\varepsilon}-1)/(\sqrt{\varepsilon}+1)$, ε is extinction ratio of the dual electrode MZM, γ is a dimensionless ratio of less than one, which describes the electro-optic coefficient ratio in the x-axis to that of the z-axis and ω is the optical angular frequency. The total electric field exiting the dual electrode z-cut $LiNbO_3$ MZM with insertion loss t_{ff} is given by

$$\bar{\mathbf{E}}_{out,\alpha}(t)=\sqrt{\frac{P_{in}t_{ff}}{1+\delta^2}}\begin{pmatrix}\hat{z}\cos(\alpha)\begin{bmatrix}e^{j\left(m_1\sin\left[\Omega_1(t+\Delta\tau)\right]+m_2\sin\left[\Omega_2(t+\Delta\tau)\right]\right)}\\+\delta e^{j\left(m_1\cos\left[\Omega_1(t+\Delta\tau)\right]+m_2\cos\left[\Omega_2(t+\Delta\tau)\right]-\pi/2\right)}\end{bmatrix}e^{j\omega(t+\Delta\tau)}\\+\hat{x}\sin(\alpha)\begin{bmatrix}e^{j\gamma\left(m_1\sin(\Omega_1 t)+m_2\sin(\Omega_2 t)\right)}\\+\delta e^{j\left(\gamma\left(m_1\cos(\Omega_1 t)+m_2\cos(\Omega_2 t)\right)-\pi/2\right)}\end{bmatrix}e^{j\omega t}\end{pmatrix}. \quad (6.1)$$

By using the Jacobi-Auger expansion $e^{jx\sin(\Omega t)}=\sum_{n=-\infty}^{\infty}J_n(x)e^{jn\Omega t}$ and $e^{jx\cos(\Omega t)}=\sum_{n=-\infty}^{\infty}j^nJ_n(x)e^{jn\Omega t}$ on (6.1), one obtains the total electric field exiting the dual electrode z-cut $LiNbO_3$ MZM, just before the second linear polarizer as,

$$\begin{aligned}\bar{\mathbf{E}}_{out,\alpha}(t)=&\sqrt{\frac{P_{in}t_{ff}}{1+\delta^2}}\sum_{n=-\infty}^{\infty}\sum_{m=-\infty}^{\infty}\left(1-\delta j^{(n+m+1)}\right)\\&\times\begin{Bmatrix}\hat{z}\cos(\alpha)J_n(m_1)J_m(m_2)e^{j(n\Omega_1+m\Omega_2+\omega)\Delta\tau}\\+\hat{x}\sin(\alpha)J_n(\gamma m_1)J_m(\gamma m_2)\end{Bmatrix}\\&\times e^{j(n\Omega_1+m\Omega_2+\omega)t}\end{aligned} \quad (6.2)$$

It is seen that lower sidebands at frequencies of $-\Omega_1$ and $-\Omega_2$ are suppressed in (6.2) thus OSSB modulation is obtained.

After the second linear polarizer, which is set to the angle of β with respect to the z-axis, the electric field component exiting the second linear polarizer is given by,

$$E_{out,\beta}(t) = \sqrt{\frac{P_{in} t_{ff}}{1+\delta^2}} \sum_{n=-\infty}^{\infty} \sum_{m=-\infty}^{\infty} \left(1 - \delta j^{(n+m+1)}\right) \times \left\{ \begin{array}{l} \cos(\alpha)\cos(\beta) J_n(m_1) J_m(m_2) e^{j(n\Omega_1 + m\Omega_2 + \omega)\Delta\tau} \\ +\sin(\alpha)\sin(\beta) J_n(\gamma m_1) J_m(\gamma m_2) \end{array} \right\} \times e^{j(n\Omega_1 + m\Omega_2 + \omega)t} \quad (6.3)$$

Applying the Bessel series expansion, $J_n(x) \equiv \sum_{r=0}^{\infty} (-1)^r (x/2)^{2r+n} / (r!(n+r)!)$ on (6.3) the output electric field is simplified into,

$$\begin{aligned} E_{out,\beta}(t) = & \sqrt{\frac{P_{in} t_{ff}}{1+\delta^2}} (1-\delta j) \begin{pmatrix} \cos(\alpha)\cos(\beta) e^{j\omega\Delta\tau} + O(m_1^2) \\ \sin(\alpha)\sin(\beta) + O(m_2^2) \end{pmatrix} e^{j\omega t} \\ & + \frac{(1+\delta)}{2} \sqrt{\frac{P_{in} t_{ff}}{1+\delta^2}} \begin{pmatrix} \cos(\alpha)\cos(\beta)\left[m_1 - \frac{1}{8} m_1^3\right] e^{j(\omega+\Omega_1)\Delta\tau} + \\ \sin(\alpha)\sin(\beta)\left[\gamma m_1 - \frac{1}{8}\gamma^3 m_1^3\right] + O(m_1^5) \end{pmatrix} e^{j(\omega+\Omega_1)t} \\ & + \frac{(1+\delta)}{2} \sqrt{\frac{P_{in} t_{ff}}{1+\delta^2}} \begin{pmatrix} \cos(\alpha)\cos(\beta)\left[m_2 - \frac{1}{8} m_2^3\right] e^{j(\omega+\Omega_2)\Delta\tau} + \\ \sin(\alpha)\sin(\beta)\left[\gamma m_2 - \frac{1}{8}\gamma^3 m_2^3\right] + O(m_2^5) \end{pmatrix} e^{j(\omega+\Omega_2)t} \\ & - \frac{(1+\delta)}{2} \sqrt{\frac{P_{in} t_{ff}}{1+\delta^2}} \begin{pmatrix} \cos(\alpha)\cos(\beta)\frac{1}{8} m_1^2 m_2 e^{j(\omega+2\Omega_1-\Omega_2)\Delta\tau} + \\ \sin(\alpha)\sin(\beta)\frac{1}{8}\gamma^3 m_1^2 m_2 + O(m_1^4 m_2^3) \end{pmatrix} e^{j(\omega+2\Omega_1-\Omega_2)t} \\ & - \frac{(1+\delta)}{2} \sqrt{\frac{P_{in} t_{ff}}{1+\delta^2}} \begin{pmatrix} \cos(\alpha)\cos(\beta)\frac{1}{8} m_1 m_2^2 e^{j\omega\Delta\tau} + \\ \sin(\alpha)\sin(\beta)\frac{1}{8}\gamma^3 m_1 m_2^2 + O(m_1^3 m_2^4) \end{pmatrix} e^{j(\omega+2\Omega_2-\Omega_1)t} + \cdots \end{aligned} \quad (6.4)$$

From (6.4) it can be seen that $e^{j(\omega+\Omega_i)\Delta\tau}$, $i = 1,2$ is the differential phase delay between the two orthogonal polarization components for a given RF subcarrier. Third order IMD cannot be completely suppressed if this differential phase delay is not negligible.

However, if it is negligible, i.e. $e^{j(\omega+\Omega_i)\Delta\tau} \approx 1-\left((\omega+\Omega_i)\Delta\tau\right)^2/2$, for $\omega\Delta\tau<<1$, which is usually the case as stated in [63] the differential phase delay is small for the MZM, ~1 % and the condition for the complete suppression of third order IMD will depend on the differential group delay, as given in (6.5). It is seen from (6.4) that the intermodulation distortion due to the characteristic of the MZM can be removed by eliminating the IMD components or the terms proportional to $m_{1,2}^3$ in electric field, if the following condition of

$$\cos(\alpha)\cos(\beta)\left[1-\frac{(\omega\Delta\tau)^2}{2}\right]+\gamma^3\sin(\alpha)\sin(\beta)=0, \tag{6.5}$$

is satisfied, where the assumption of $\omega\Delta\tau<<1$ was used. We may see that (6.5) does not have a unique solution, so it would be ideal to choose a solution that maximizes the RF carriers that are proportional to $m_{1,2}$ in electric field. This yields $\alpha=-\beta=\pm\tan^{-1}\left(\gamma^{-3/2}\sqrt{1-(\omega\Delta\tau)^2/2}\right)$. Due to linearization, a decrease in optical RF signal subcarrier power is induced by a factor of $\frac{\gamma(1-\gamma^2)}{\left(1-(\omega\Delta\tau)^2/2+\gamma^3\right)}\left(1-(\omega\Delta\tau)^2/2\right)$, for $\omega\Delta\tau<<1$. If birefringence is neglected, i.e. $\omega\Delta\tau=0$ and $\gamma=1/3$ for a typical z-cut $LiNbO_3$ MZM, this leads to $\alpha=-\beta=\pm 79^0$ and the above factor yields an 11 dB loss, which is the same as [63]. It is also noted from (6.5) that the suppression of 3IMD is not dependent on individual modulation depths, so a costly DC bias controller is not required for this proposed design.

6.3 SFDR and Sensitivity Analysis

A development for the expression of SFDR for a RoF system, where the considered mixed-polarization OSSB MZM is used. The IMD output power includes residual IMD and its higher orders components. Assuming equal modulation index, i.e. $m_1 = m_2 = m$, using (6.4) to obtain the photo-current $\frac{1}{2}\Re G_{opt} L_{opt} E_{out,\beta}(t) E^{*}_{out,\beta}(t)$, where $\Re$ is the responsivity of the photodetector, G_{opt} is the gain of the optical amplifier and L_{opt} is insertion loss of optical filter. The RF carrier and 3IMD output power are expressed as

$$P_{RF} = \frac{\varepsilon}{4(1+\varepsilon)} a_0^2 a_1^2 \left(\Re P_{in} L_{opt} G_{opt} t_{ff}\right)^2 G_{RF} L_{RF} m^2 R_L \tag{6.6}$$

and

$$P_{3IMD} = \left(\frac{5}{384}\right)^2 \frac{\varepsilon}{1+\varepsilon} a_0^2 a_5^2 \left(\Re P_{in} L_{opt} G_{opt} t_{ff}\right)^2 G_{RF} L_{RF} m^{10} R_L, \tag{6.7}$$

respectively, where

$$a_n = \mathbf{cos}(\alpha)\mathbf{cos}(\beta) + \gamma^n \mathbf{sin}(\alpha)\mathbf{sin}(\beta),$$

(6.8) R_L is the receiver load, G_{RF} is the gain of the RF amplifier and L_{RF} is loss of RF connectors used after the photodetector. Similarly for the conventional MZM, the RF carrier and 3IMD output power can be computed similar to the above and also by setting $\alpha = \beta = 0$ in (6.4), and can be expressed as

$$P_{RF} = \frac{\varepsilon}{4(1+\varepsilon)} \left(\Re P_{in} L_{opt} G_{opt} t_{ff}\right)^2 G_{RF} L_{RF} m^2 R_L \tag{6.9}$$

and

$$P_{3IMD} = \frac{\varepsilon}{2^8(1+\varepsilon)}\left(\Re P_{in} L_{opt} G_{opt} t_{ff}\right)^2 G_{RF} L_{RF} m^6 R_L, \tag{6.10}$$

respectively.

To obtain the expression of SFDR, one must solve the equation of $P_{3IMD} = N_0$, where N_0 is the receiver noise floor power, for m and use this m in P_{RF} to obtain the electrical RF carrier power then the SFDR is obtained by dividing the electrical RF carrier power by the noise power floor N_0. The SFDR for using the linearized and conventional MZM can be easily computed, respectively as

$$SFDR = \left(\frac{3}{5}\right)^{2/5} \frac{a_0^{8/5} a_1^2}{a_5^{2/5}} \left(\frac{2\varepsilon}{1+\varepsilon}\left(\Re P_{in} L_{opt} G_{opt} t_{ff}\right)^2 G_{RF} L_{RF} R_L / N_0\right)^{4/5} \tag{6.11}$$

and

$$SFDR_c = \left(\frac{2\varepsilon}{1+\varepsilon}\left(\Re P_{in} L_{opt} G_{opt} t_{ff}\right)^2 G_{RF} L_{RF} R_L / N_0\right)^{2/3}. \tag{6.12}$$

Setting $\beta = -\alpha + \Delta\phi$, where $\Delta\phi$ is the angular detuning from the "ideal" angle of $\pm 79^0$ to understand the impact of $\Delta\phi$ and using (6.5) and (6.8), the SFDR considering the impact of $\Delta\phi$ is given after some mathematical manipulations by $a_n = \frac{\gamma^3 - \gamma^n}{1+\gamma^3}\cos(\Delta\phi)$ and substitute it into (6.11) to obtain the SFDR by using the linearized MZM considering the impact of $\Delta\phi$ and γ as

$$\begin{aligned} SFDR = {} & \left(\frac{3}{5}\right)^{2/5} \left(\frac{2\varepsilon}{1+\varepsilon}\left(\Re P_{in} L_{opt} G_{opt} t_{ff}\right)^2 G_{RF} L_{RF} R_L / N_0\right)^{4/5} \\ & \times \left[\sqrt{\gamma}\left(1-\gamma^2\right)\left(1-\gamma^3\right)\cos^2(\Delta\phi) / \left(1+\gamma^3\right)^2\right]^{8/5} \end{aligned} \tag{6.13}$$

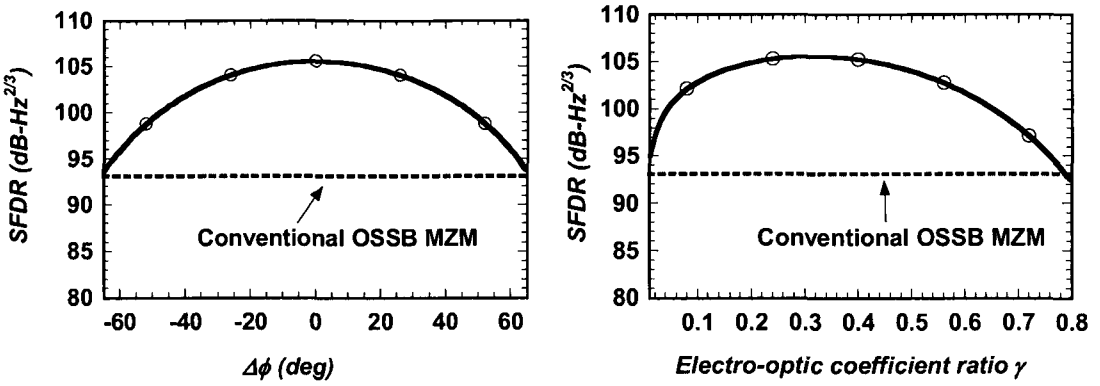

(a) (b)

Figure 6.2 (a) Theoretical SFDR versus angular detuning $\Delta\phi$ with electro-optic coefficient ratio of $\gamma = 1/3$ and (b) theoretical SFDR versus electro-optic coefficient ratio γ with $\Delta\phi = 0$ for the mixed-polarization OSSB MZM.

Figure 6.2 shows the theoretical SFDR versus angular detuning and electro-optic coefficient ratio using (6.13) for the mixed-polarization OSSB MZM and (6.12) using the conventional MZM. In Fig. 6.2(a), the electro-optic coefficient ratio was set to $\gamma = 1/3$ and the angular detuning was varied from the "ideal" angle of $\beta = -\alpha = -79°$. In Fig. 6.2(b) we set the phase difference to $\Delta\phi = 0$ and varied the electro-optic coefficient ratio. For the both figures, the same parameters were used as in the experiment in Section 6.5, for example N_0 = -130 dBm/Hz, ε = 20 dB, P_{in} = 4 mW, t_{ff} = -6 dB, G = 6 dB, L_{opt} = 3.5 dB, G_{RF} = 22 dB, L_{RF} = 3 dB, R_L = 50 Ω and $\Re$ = 0.62 A/W. It is seen from Fig. 6.2 that the SFDR peaks at $\Delta\phi = 0$ and $\gamma = 1/3$. The mixed-polarization OSSB MZM improves the SFDR if detuning angle from the optimum angle is within $-62° < \Delta\phi < 62°$ and electro-optic coefficient ratio is within $0.01 < \gamma < 0.75$. An improvement of SFDR of up to ~12 dB with less sensitivity to detuning angle and electro-optic coefficient ratio if within the range of $-26° < \Delta\phi < 26°$ and $0.15 < \gamma < 0.49$, respectively. This indicates

that the mixed-polarization OSSB MZM is, to some extent, robust to polarizer angle and electrode material electro-optic coefficient instabilities.

6.4 Simulation Results and Analysis

As shown in Fig. 6.1, two RF tones drive the electrodes of the z-cut $LiNbO_3$ MZM, but they are 90^0 phase shifted from each other and the MZM is biased at quadrature. The z-cut $LiNbO_3$ MZM has 6 dB insertion loss, 20 dB extinction ratio and a half wave switching voltage of 5 V. The CW laser is set to 1550 nm with linewidth of 800 KHz, optical power of 6 dBm and relative intensity noise (RIN) of -150 dB/Hz. The angles of α and β of the two linear polarizers are set to $\pm 79^0$, respectively. The optical transmission is through 20 km of single-mode fiber with an attenuation of 0.2 dB/km and chromatic dispersion of 16 $ps/(nm \cdot km)$. The fiber attenuation is compensated and an optical filter of 68 GHz bandwidth is used to filter the optical signal before being detected by a PIN photodetector with responsivity of 0.62 A/W and thermal noise of 10^{-12} A/$\sqrt{Hz}$. We consider an optical carrier transporting two RF tones at f_1 = 8 GHz and f_2 = 10 GHz as to match the tones used in the experimental analysis in Section 6.5.

Figures 6.3(a) and (b) show simulated optical spectra at input of the photodetector for a RoF system through 20 km of SMF using the conventional OSSB MZM and mixed-polarization OSSB MZM with the linear polarizer angles optimally set to $\pm 79^0$, respectively. The total RF input power for the two tones was set to 19 dBm in both the conventional and mixed-polarization OSSB MZM. It is verified that the mixed-polarization MZM leads to an OSSB modulation as shown in Fig. 6.3(b) (the residual RF

signal subcarriers at -8 and -10 GHz are due to finite extinction ratio of the MZM). Moreover, in the conventional MZM in Fig. 6.3(a), it is seen that two 3IMDs, which are located at frequencies of $2f_1 - f_2$=6 GHz and $2f_2 - f_1$=12 GHz, are close to the RF signal subcarriers and the most detrimental to them. Conversely, using the mixed-polarization MZM the 3IMD components at 6 and 12 GHz are suppressed by more than 32 dBc compared to using the conventional MZM. It is seen that there are many optical intermodulation components generated by using high RF input power. However, their power levels are considerably reduced when using the mixed-polarization MZM compared the conventional MZM as seen from Fig. 6.3(b). These intermodulation components will beat with one another at the photodetector, generating components that will overlap in frequency with the two RF carriers, so that power fading due to fiber chromatic dispersion and crosstalk may be caused. This suggests that intermodulation components related beats induced power fading and crosstalk will be significantly reduced by using the mixed-polarization MZM.

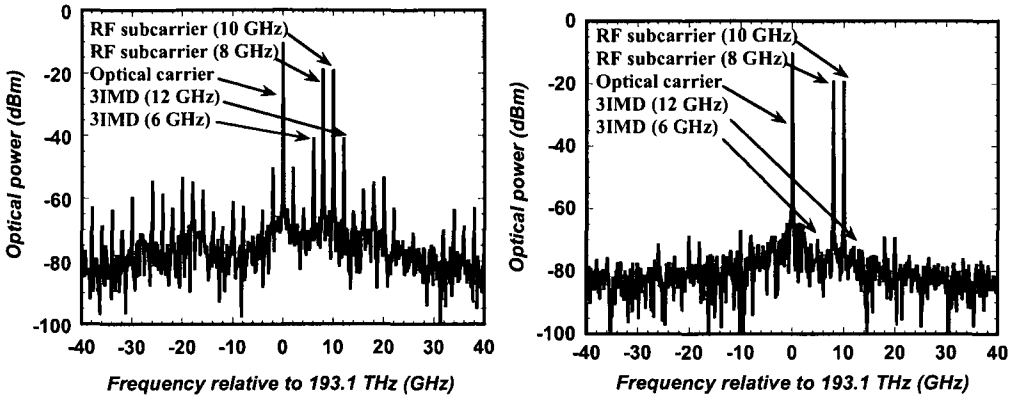

Figure 6.3 Simulated optical spectra at the input of the photodetector, for a RoF system through 20 km of SMF using (a) conventional OSSB MZM and (b) mixed-polarization OSSB MZM with polarizer angles optimally set to $\pm 79^0$.

Corresponding to Fig. 6.3, the RF output spectra are shown in Figs. 6.4(a) and (b). It is clearly shown that by using the conventional OSSB MZM the intermodulation distortion components are comparable to the two RF carriers (~1 dB difference between the RF carriers and 3IMD components) as show in Fig. 6.4(a). However, by using the mixed-polarization MZM, the magnitudes of distortion components are significantly reduced and 3IMD is suppressed by more than 30 dBc below the two RF carriers.

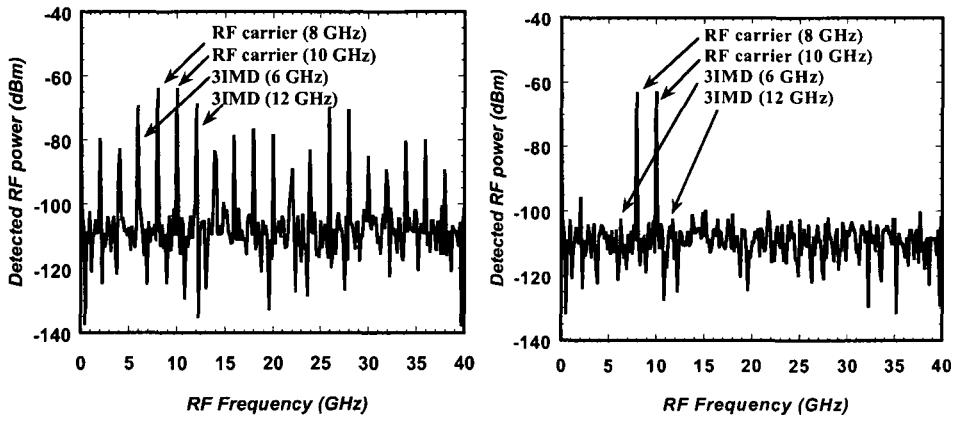

(a) (b)

Figure 6.4 Simulated RF spectra at the output of the photodetector for a back-to-back RoF system using (a) conventional OSSB MZM and (b) mixed-polarization OSSB MZM with polarizer angles optimally set to $\pm 79^0$, respectively.

It is known that OSSB is not greatly affected by power fading when transmitted through dispersive fiber [75]. In order to investigate the effect of chromatic dispersion when using the mixed-polarization MZM at high modulation index, we simulated and compared both conventional and mixed-polarization MZM with RF of 8 and 10 GHz, where the input RF power level was set to 19 dBm for both the conventional and mixed-polarization MZM.

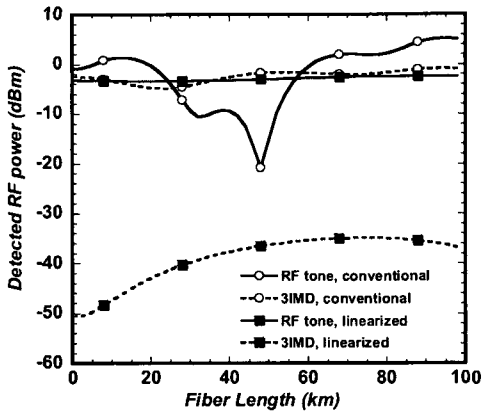

Figure 6.5 Simulated RF carrier power and 3IMD power versus fiber length for a RoF system using the conventional and mixed-polarization OSSB MZM, respectively with compensated fiber loss.

Figure 6.5 compares RF carrier and 3IMD power by using the conventional and mixed-polarization MZM. Fiber loss is compensated in order to emphasize the effects of chromatic dispersion on the RF signal. We can see that RF carrier power does not vary with the change of fiber length and thus there is no intermodulation components induced fading and crosstalk when using the mixed-polarization OSSB MZM, while the RF carrier power fluctuates with the change of fiber length and thus intermodulation components induced power fading and crosstalk must exist when using the conventional OSSB MZM. This is due to constructive and destructive interaction between many harmonic and intermodulation components by using the conventional MZM as shown in Fig. 6.4(a). Thus the beats are overlapped in frequency with the RF carriers, and then the beats interplay with the RF carriers. It is clearly shown that the mixed-polarization MZM is immune to power fading and crosstalk caused by the interaction of intermodulation and chromatic dispersion. It is shown that 3IMD is suppressed by more than 30 dB in power as shown in Fig. 6.4(b). Therefore, not only is the mixed-polarization OSSB transmission

immune to power fading and crosstalk, but it also provides a greater suppression of 3IMD, which leads to an improvement in SFDR.

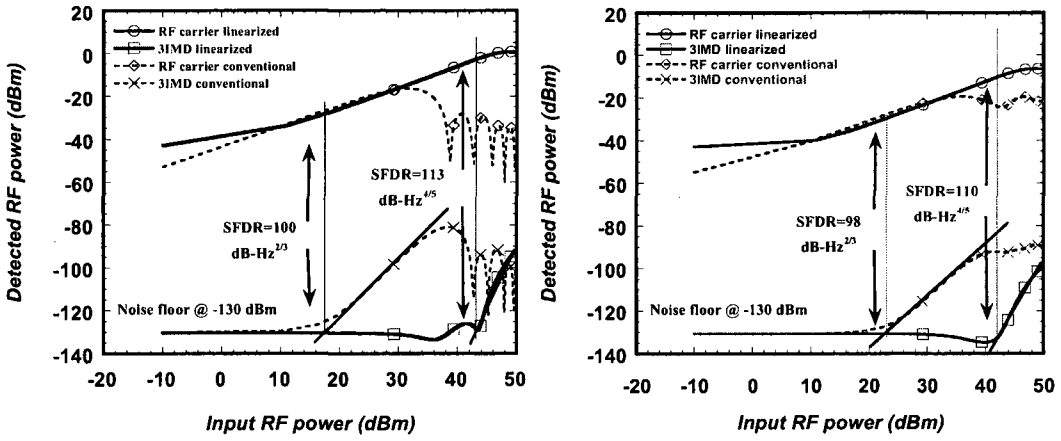

(a) (b)

Figure 6.6 Simulated spurious free dynamic range for a RoF system in a normalized 1 Hz noise bandwidth using the mixed-polarization and conventional OSSB MZM in (a) back-to-back and (b) through 20 km of single mode fiber.

In order to show the suppression of 3IMD by using the mixed-polarization OSSB MZM over the conventional OSSB MZM, we compared the simulated SFDR for a RoF system using a mixed-polarization and conventional OSSB MZM as shown in Figs. 6.6(a) and (b) for back-to-back and through 20 km of single-mode fiber, respectively. From Fig. 6.6 it is shown that nonlinear distortion is limited to 5^{th} order (see the slope of 3IMD power) for the RoF system using the mixed-polarization MZM. But for the conventional MZM, it is limited to 3^{rd} order nonlinear distortion as seen in Fig. 6.6. This shows that the 3IMD is cancelled by using the mixed-polarization MZM. Figure 6.6 shows that SFDR improvement of ~13 dB is obtained by using the mixed-polarization modulator for both back-to-back and 20 km fiber cases.

6.5 Experimental Results and Analysis

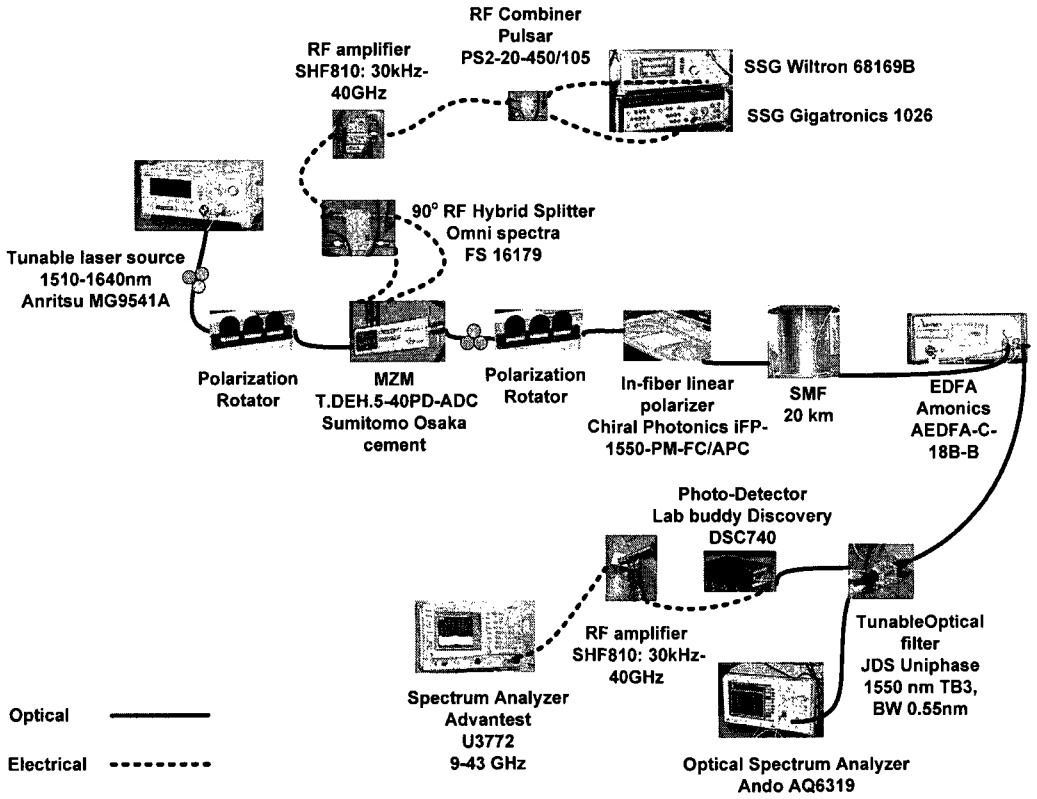

Figure 6.7 Experimental setup for a RoF system using the mixed-polarization OSSB MZM (SSG: Synthesized Sweep Generator, EDFA: Erbium doped fiber amplifier).

Figure 6.7 shows the experimental setup for a RoF system using the mixed-polarization MZM. Two RF synthesizers are used to generate two tones at 8 and 10 GHz with equal power. The combined RF tones are amplified by a low-noise amplifier (LNA) with 22 dB gain and drive a dual-electrode MZM for OSSB modulation using a 90^0 hybrid splitter. The photo-detected signal is amplified by another LNA of 22 dB gain. The RF power levels from the two synthesizers were varied from -20 to -5 dBm to operate the LNA in the linear regime. The tunable laser source delivers a linearly polarized light. One

polarization controller was used to manually adjust the polarization angle α of the input lightwave to the MZM. Another polarization controller with a Chiral Photonics in-fiber linear polarizer is used to manually adjust the polarization angle β of the output lightwave from the MZM. An optical amplifier was used to compensate for optical fiber loss and insertion loss of the MZM. An optical filter of bandwidth 0.55 nm and insertion loss of 3.5 dB is used before the photodetector to reduce the amplified spontaneous emission noise. Table 6.1 shows the parameter settings for the setup in Fig. 6.7.

Table 6.1 Physical parameters for the experiment.

Optical wavelength	λ	1549.8145 nm
Optical power	P_{in}	6 dBm
Optical amplifier gain	G	6 dB
RF_1 frequency	f_1	8 GHz
RF_2 frequency	f_2	10 GHz
Elec. spectrum analyzer's resolution	RBW	100 Hz
Elec. spectrum analyzer's noise floor density	N_0	-130 dBm/Hz
Mach-Zehnder V_π	$V\pi$	5 V
Mach-Zehnder insertion loss	t_{ff}	6 dB
Mach-Zehnder extinction ratio	ε	20 dB
Optical filter insertion loss	L_{opt}	3.5 dB
Photodetector responsitivity	$\Re$	0.62 A/W
LNA gain	G_{RF}	22 dB
RF connectors loss	L_{RF}	3 dB
Load resistance of the optical receiver	R_L	50 Ω

Figure 6.8 shows the measured optical spectra from the output of the conventional and mixed-polarization modulator. It is seen that OSSB modulation is obtained in both cases.

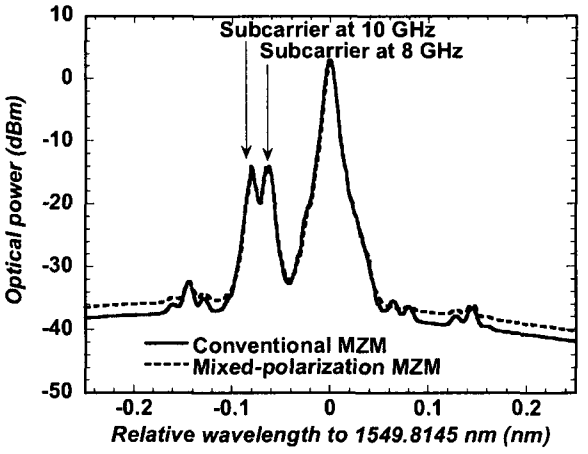

Figure 6.8 Measured optical spectrum using the conventional and mixed-polarization MZM.

Figure 6.9 shows the measured SFDR by using the conventional and mixed-polarization MZM. For fair comparison we have compensated for linearization loss in order to have the same RF tone output power, by increasing the optical power for the mixed-polarization MZM. It is seen that an improvement of ~12.5 dB in SFDR is obtained using the mixed-polarization over the conventional MZM, which matches exactly with theoretical prediction and simulation results. This is because in the experiment the birefringence is negligible in the MZM and the interconnection fiber between the MZM output and the second linear polarizer.

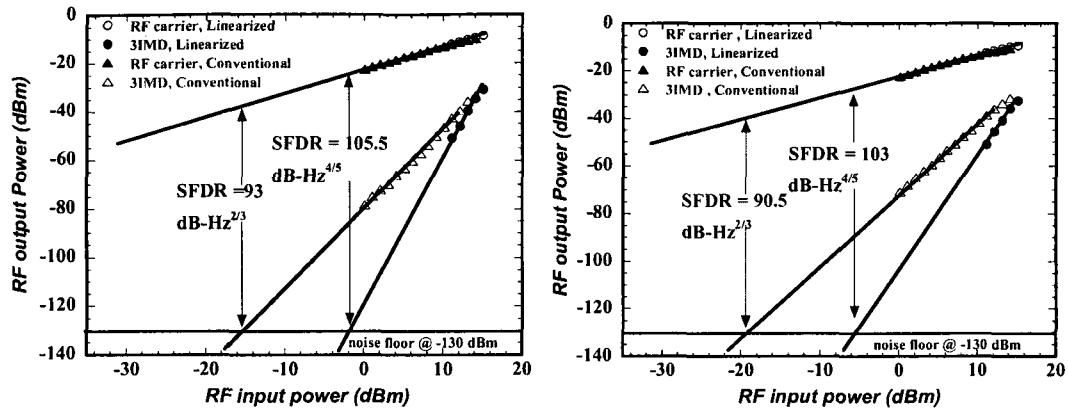

(a) (b)

Figure 6.9 Measured SFDR in a normalized 1 Hz noise bandwidth for (a) back-to-back and (b) 20 km RoF system using the conventional and mixed-polarization OSSB MZM.

6.6 Conclusion

This chapter presented the mixed-polarization OSSB Mach-Zehnder modulator, which alleviated most of the limitations incurred by the previous proposed linearization techniques. A comprehensive investigation was conducted for the mixed-polarization MZM in the suppression of intermodulation distortion in theory, simulation and experiment. The suppression of third order intermodulation distortion using the mixed-polarization MZM is independent of modulation index. Both theory and simulation predict a 13 dB improvement of SFDR for back-to-back and 20 km fiber RoF system using the mixed-polarization modulator. Moreover, power fading of the RF carrier and crosstalk due to intermodulation via fiber chromatic dispersion is significantly suppressed compared to using the conventional OSSB MZM.

We experimentally verified the mixed-polarization modulation technique. It was shown that an improvement of ~12.5 dB in SFDR using discrete optical components was

achieved and good agreement with theory and simulation is obtained. Again due to the linearization process a RF carrier power penalty is incurred, which will need to be compensated for with optical amplifiers or increasing the input optical power. It will remain as future research to find a way to improve upon this technique by reducing the power penalty.

Chapter 7

7 Conclusion

7.1 Concluding Remarks

We have proposed and investigated four linearization techniques for RoF systems, i.e. single wavelength balanced RoF system with ODSB subcarrier modulation, tunable chirped FBG with ODSB subcarrier modulation, bidirectional asymmetric Mach-Zehnder modulator with OSSB subcarrier modulation, and mixed-polarization Mach-Zehnder modulator with OSSB subcarrier modulation. Despite the fact that the first two designs use ODSB subcarrier modulation, all proposed linearization techniques can be immune to fiber chromatic dispersion.

We used simulation and theoretical analysis to comprehensively study the four linearization techniques in performance and stability. Moreover, we verified the proposed mixed-polarization Mach-Zehnder modulator experimentally. In addition we compared the four linearization techniques with the previously proposed linearization techniques described in literature and used in practice. We used the magnitude of nonlinear distortion, spurious free dynamic range, BER and receiver sensitivity to compare the performance of the linearization techniques with the previously proposed techniques.

The single wavelength balanced RoF system improves the existing balanced RoF system by providing more second order distortion suppression, which is due to the fact that only one wavelength is used, so it is not susceptible to phase error. Simulation shows

a second order harmonic suppression of 14.2 dB over the conventional OSSB RoF system and the improvement is 6.6 dB with the use of 25 km of single mode fiber. The main drawback of the proposed balanced system is that two optical modulators are required. The second order distortion suppression is not degraded by power variations and remains relatively constant.

The tunable FBG balanced system further improves the performance of the above balanced RoF system by providing suppression of both second and third order distortions. Simulation shows a second and third harmonic distortion suppression of 25.4 dB and 2.6 dB and second and third order intermodulation distortion suppression of 33 dB and 20 dB are obtained, respectively. Furthermore, the technique makes use of only one optical modulator, and still makes use of optical double side transmission. The ripple phase and polarization errors at the tunable nonlinearly chirp FBG needs to be addressed for optimal performance.

The asymmetric OSSB Mach-Zehnder modulator technique has improved spurious free dynamic range. It is found that a relative spurious free dynamic range improvement of 13 and 17 dB is achieved in comparison to the dual-parallel MZM and the conventional MZM in a back-to-back configuration and with 20 km of single mode fiber, the improvement was 13 and 17 dB, respectively. Also because the cancellation of third order distortion, there is also approximately 10 dB of RF carrier power that is reduced, this will need to be compensated. The MZM is bidirectionally fed, so it would be susceptible to crosstalk, thereby reducing performance. In order to prevent this, RF carriers should be above 2 GHz, so this limits some available bandwidth from the RoF system.

The mixed-polarization OSSB Mach-Zehnder modulator provides all the benefits of the asymmetric MZM, but with a very simple design that may be more easily integrated in a practical modular design. The technique also performs well with high modulation index. Also the linearization performance is independent of modulation index and only depends on polarizer angles, so there is no need to maintain a match between modulation indices for each electrode branch. The polarizer angles may also be adjusted to cancel other order distortions depending on the application requirements. Theory, simulation and experiment shows that for the mixed-polarization Mach-Zehnder modulator compared to the conventional MZM, an improvement of ~13 dB in spurious free dynamic range is obtained for the back-to-back and with 20 km of fiber.

Of course the linearization still leads to RF carrier power loss of about 10 dB. There are tradeoffs in any linearization method, where by cancelling nonlinear distortion some RF carrier power is also reduced. A properly designed linearized RoF system should incorporate the use of more than one linearization technique. Table 7.1 summarizes the contributions described in this thesis along with comments on each proposed technique.

Table 7.1 Contributions and Comment.

Contributions	Improvements	Drawbacks	Complexity	Cost
Single wavelength balanced RoF system	▪ Improved 2nd order suppression ▪ Less phase error at balanced detector	▪ Must be biased accordingly for 3rd order distortion suppression ▪ Only suppresses 2nd order distortion	Medium	Medium
Tunable FBG balanced RoF system	▪ 2nd and 3rd order suppression	▪ Ripple phase delay at the nonlinearly chirped FBG ▪ Polarization changes at the nonlinearly chirped FBG	Low	Low
Asymmetric MZM	▪ 3rd order suppression ▪ Improved SFDR ▪ Optical single sideband transmission	▪ RF power penalty ▪ RF carrier must be greater than 2GHz ▪ Must match modulation indices	Medium	Low
Mixed-polarization MZM	▪ 3rd order suppression ▪ Independent of individual modulation indexes ▪ Improved SFDR ▪ Optical single sideband transmission	▪ RF power penalty	Low	Low

7.2 Future Work and Direction

The research contributions presented in this thesis may be extended in several ways. The first is to investigate if there is a way to further improve the mixed-polarization OSSB Mach-Zehnder modulator by reducing or removing the RF carrier power penalty of ~10 dB. Also, since the mixed-polarization OSSB Mach-Zehnder modulator was realized with discrete optical components, the next important practical experiment to carry out would

be to incorporate the mixed-polarization OSSB Mach-Zehnder modulator on one silicon substrate or module to further investigate its performance.

It would be beneficial to experimentally demonstrate the tunable FBG balanced system by fabricating a tunable nonlinearly chirped FBG and experimentally test its performance and sensitivity to ripple phase and polarization changes. This device would be beneficial to cable access networks, because the electrical balanced device being used today is bandwidth limited, which is not the case with the proposed balanced systems described in Chapters 3 and 4. Also of interest would be to investigate if the proposed balanced systems discussed in this thesis can be improved by incorporating OSSB modulation.

As previously discussed in Chapter 5 the asymmetric OSSB Mach-Zehnder modulator is limited to RF signals of above 2 GHz, so it would be interesting to experimentally obtain the co- and counter- propagating optical response, so that performance conditions may be further studied in terms of response ripple due to RF port reflections and crosstalk. This may lead to a means to alleviate the RF signal bandwidth limitation.

7.3 Publications

1. B. Masella, X. Zhang, "A novel single wavelength balanced system for radio over fiber links," *IEEE Photon. Technol Lett.,* vol. 18, pp. 301-303, Jan. 2006.
2. B. Masella, X. Zhang, "A simplified radio over fiber balanced system with suppression of both second and third-order nonlinear distortions," *Photonics North '06,* MIC-05-4-2, June. 2006.
3. B. Masella, X. Zhang, "Linearized optical single-sideband Mach–Zehnder modulator for radio-over-fiber systems," *IEEE Photon. Technol. Lett.,* vol. 19, pp. 2024-2026, Dec 2007.
4. B. Masella, X. Zhang, "Linearized optical single sideband Mach-Zehnder electro-optic modulator for radio over fiber systems," *Optics Express,* vol. 1, pp. 9181-9190, June 2008.
5. B. Masella, B. Hraimel and X. Zhang, "Enhanced spur-free dynamic range using mixed-polarization in optical single sideband Mach-Zehndermodulator", Accepted for publication in *J. Lightwave Technol.,* 2009.
6. B. Masella, B. Hraimel, X. Zhang, "Mixed-polarization to improve dynamic range of optical single sideband in a Mach-Zehnder modulator," *OFC/NFOEC.* , paper OWP2, Mar. 2009.

References

[1] S. V. Kartalopoulos, " DWDM Networks, Devices and Technology", Wiley-Interscience, Piscataway, New Jersey, pp. 270-290, 2003.

[2] A. J. Cooper, .Fiber/Radio for the provision of cordless/mobile telephony services in the access network,. *Electron. Lett.,* vol. 26, no. 24, pp. 2054.2056, Nov. 1990.

[3] H. Al-Raweshidy and S. Komaki, "Radio over fiber technologies for mobile communicationnetworks", *Artech House*, Boston, London, pp. 188-414, 2002

[4] J. A. Chiddix, H Laor, D. M. Pangrac, L. D. Williamson and R.W. Wolfe, "AM video on fiber in CATV systems: need and implementation," *IEEE J. Selected Areas in Communications,* vol. 8, pp. 1229-1239, 1990.

[5] T. E. Darcie and G. E. Bodeep, "Lightwave subcarrier CATV transmission systems," *IEEE Trans. Microwave Theory and Techniques,* vol. 38, pp. 524-533, 1990.

[6] A. A. M. Saleh, "Fundamental limit on number of channels in subcarrier-multiplexed lightwave CATV system," *Electron. Lett.,* vol. 25, pp. 776-777, June, 1989.

[7] K. Alameh and R. A. Minasian, "Ultimate limits on subcarrier multiplexed lightwave transmission," *Electron. Lett.,* vol. 27, pp. 1260-1262, 1991.

[8] N. J. Frigo, M. R. Phillips and G. E. Bodeep, "Clipping distortion in lightwave CATV systems: models, simulations and measurements," *J. Lightwave Technol.,* vol. 11, pp. 138-146, 1993.

[9] B. H. Wang, P. Y. Chiang, M. S. Kao and W. I. Way, "Large-signal spurious-free dynamic range due to static and dynamic clipping in direct and externally modulation systems," *J. Lightwave Technol.,* vol. 16, pp. 1773-1785, 1998.

[10] A. Dutta-Roy, "Cable is not just for TV," IEEE Spectrum., pp. 53-59, May, 1999.

[11] S, Ovadia and C. Lin, "Performance characteristics and applications of hybrid multichannel AM-VSB/MQAM video lightwave transmission systems," *J. Selected Areas in Communications,* vol. 16, pp. 1171-1186, 1998.

[12] N. A. Olsson, "Lightwave systems with optical amplifiers," *J. of Lightwave Technol.*, vol. 7, pp. 1071-1082, 1989.

[13] A. J. Lowery, "Transmission-line laser modeling of semiconductor laser amplified optical communication systems," *IEEE Proc.-J.*, vol. 139, pp. 180-188, June. 1992.

[14] http://www.iec.org/online/tutorials/epon/index.asp, Feb. 18, 2009.

[15] M. Sekita and et al., TV video transmission by analog baseband modulation of 1.3um band laser diode," 6th Europ. Conf. Opt. Comm., pp. 394-396, 1980.

[16] D. A. Atlas, "Non-linear optical crosstalk in WDM CATV systems," *IEEE/LOES Summer Topical Meeting-RF Photonics for CATV and HFC Systems,* 1999.

[17] C. Y. Kou, "Fundamental second-order nonlinear distortions in analog AM CATV transport systems based on single frequency semiconductor lasers," *IEEE Journal of Lightwave Technology.*, vol. 10, pp. 235-243, 1992.

[18] K. Maeda, H. Nakata and K. Fujito, "Analysis of BER of 16QAM signal in AM/16QAM optical transmission system," *IEEE Electronics Letters.*, vol. 29, pp. 640-641, 1993.

[19] D. Wilt, K. Y. Lau and A Yariv, "The effect of lateral carrier diffusion on the modulation response of a semiconductor laser," *J. App. Phys.*, vol. 52, pp. 4970-4974, 1981.

[20] R. S. Tucker and D. J. Pope, "Circuit modeling of the effect of diffusion on damping in a narrow strip semiconductor," *IEEE J. Quantum Electron.*, vol. 19, pp. 1179-1183, 1983.

[21] Y. Nishimura, "Spectral hole-burning and non-linear gain decrease in-band to level transition semiconductor laser," *IEEE J. Quantum Electron.*, vol. 19, pp. 1179-1183, 1983.

[22] P. M. Boers and M. T. Vlaardingerbroek, "Dynamic behavior of semiconductor lasers," *Electron. Lett.*, vol. 21, pp. 206-208, May, 1975.

[23] K. J. Williams, R. D. Esman and M. Dagenais, "Nonlinearities in p-i-n microwave photodetectors," *IEEE Journal of Lightwave Technology.*, vol. 14, pp. 84-96, 1996.

[24] T. Ozeki and E. H. Hara, "Measurement of nonlinear distortion in photodiodes," *IEEE Electronics Letters.*, vol. 12, p. 80, 1976.

[25] M. Dentan and B. deCremoux, "Numerical simulation of the nonlinear response of a p-i-n photodiode under high illumination," *IEEE Journal of Lightwave Technology.*, vol. 8, p. 1137, 1990.

[26] R. R. Hayes and D. L. Persechini, "Nonlinearities of p-i-n photodetectors," *IEEE Photonics Technology Letters.*, vol. 5, pp. 70-72, 1993.

[27] T. E. Darcie and R. S. Tucker, "Intermodulation and harmonic distortion in InGaAsP lasers," *Electron. Lett.*, vol. 21, pp. 665-666, 1990.

[28] S. D. Walker, M. Li, A. C. Boucouvalas, D. Cunningham and A. N. Coles, "Design techniques for subcarrier multiplexed broadcast optical networks," *IEEE J. Selected Areas in Communications.*, vol. 8, pp. 1276-1284, 1990.

[29] T. S. Rappaport, " Wireless communication principles and practice", *Prentice Hall*, Upper Saddle River, New Jersey, pp. 14-17, 1996.

[30] D. Wake, D. Johansson and D. G. Moodie, "The passive picocell – a new concept in wireless network infrasructiure", electron. Lett., vol. 33, pp. 404-406, 1997.

[31] H. B. Kim, "Radio over fiber architecture," Electronic and Information Technology, University of Berlin, Berlin, M.Sc. thesis, Chapter 3, 2005.

[32] http://www.vpiphotonics.com, April 2009.

[33] S. A. Havstad, A. B. Sahin, O. H. Adamczyk, Y. Xie, A. E. Willner, "Distance-independent microwave and millimeter wave power fading compensation using a phase diversity configuration," *IEEE Photon. Technol. Lett.,* vol. 12, pp. 1052-1054, Aug. 2000.

[34] M. Nazarathy, C. H. Gall and C. Y. Kuo, "Predistorter for high frequency optical communications devices," *U.S. Patent Number 5,424,680*, June, 1995.

[35] H. A. Blauvelt and H. L. Loboda, "Predistorter for linearization of electronics and optical signals," *U.S. Patent Number 4,992,754,* Feb., 1991.

[36] L. Roselli, V. Borgioni, F. Zepparelli, F. Ambrosi, M. Comez, P. Faccin, and A. Casini, "Analog laser pre-distortion for multiservice radio over fiber system," *J. Lightwave Technol.*, vol. 21, pp.1211-1223, May 2003.

[37] L. Roselli, V. Borgioni, F. Zepparelli, M. Comez, P. Faccin, A. Casini, "Predistortion circuit design for II and III order simultaneous linearization in multiservice telecommunication apparatuses," *IEEE MTT-S International Microwave Symposium Digest*, vol. 3, pp. 1711-1714, June 2002.

[38] S. P. Stapleton, "Amplifier linearization using adaptive digital predistortion," *Appl. Microwave Wireless,* vol. 13, pp. 72-77, Feb. 2001.

[39] F. W. Willems, W. Muys and J. S. Leong, "Simultaneous suppression of stimulated Brillouin and interferometric noise in externally modulated lightwave AM-SCM systems," *IEEE Photon. Technol Lett.,* vol. 12, pp. 1476-1478, 1994.

[40] D. Hassin ans R. Vahldieck, "Feed-forward linearization of anaolog modulated laser diodes: theoretical analysis and experimental verification," *IEEE Trans. Microwave Theory Tech.*, vol. 41, pp. 2376-2382, Dec. 1993.

[41] D. Hassin and R. Vahldiek, "Improvement feed-forward linearization of laser diodes-simulation and experimental results," *Elect. MTT-S Digest*, pp. 727-730, 1993.

[42] B. Buxton and R. Vahldieck, "Noise and intermodulation distortion reduction in an optical feed-forward transmitter," *Elect. MTT-S Digest*, pp. 1105-1108, 1994.

[43] M. Chongcheawchamnan, M. J. Blewett and I. Robertson, "Feed-forward linearization applied to a direct carrier modulation transmitter," *IEEE ISCS'2000*, vol. 1, pp. 655-658, 2000.

[44] J. L. Brooks, G. S. Maurer and R. A. Becker, "Implementation and evaluation of a dual parallel linearization system for AM-SCM video transmission," *IEEE J. Lightwave Technol.,* vol. 11, pp. 34-41, Jan. 1993.

[45] H. D. Jung, G. W. Lee, S. K. Han, "Nonlinearity suppression of electro-absorption modulator through dual-parallel modulation", *Microwave Technol. Lett.*, vol 29, pp. 2-5, 2001.

[46] H. Skeie and R. V. Johnson, "Linearization of electro-optica modulator by a cascade coupling of phase modulating electrodes," *Intergrated optical circuits, SPIE proceedings*, vol. 1583, pp. 153-164, 1991.

[47] T. V. Muoi, "Optical receivers," *Optoelectronic Technology and Lightwave Communications,* ED. Chinlon Lin, Chapter 16, Van Nostrand, Princeton, 1989.

[48] J. Yoshida, Y. Akahori, M. Ikeda, N. Uchida and A. Kozen, "Sensitivity limits of long-wavelength monolithically integrated p-i-n JFET photoreceivers," *IEEE J. Lightwave Technol.,*vol. 14, pp. 770-779, 1996.

[49] S. Mathai, F. Cappelluti, T. Jung, D. Novak, R. Waterhouse, D. Sivco, A. Cho, G. Ghione and M. Wu, "Experimental demonstration of a balanced electro-absorption modulated microwave photonic link," *IEEE Trans. Microwave Theory Tech.*, vol. 49, pp. 1956-1961, Oct. 2001.

[50] T. E. Darcie, R. Paiam, A. Moye, J. D. Bull, H. Kato and N. A. F. F. Jaeger, "Intensity-noise suppression in microwave-photonic links using polarization modulation," *IEEE Photon. Technol Lett.,* vol. 17, pp. 1941-1943, Sept. 2005.

[51] T. E. Darcie, A. Moye, "Modulation-dependent limits to intensity-noise suppression in microwave-photonic links," *IEEE Photon. Technol Lett.,* vol. 17, pp. 2185-2187, Oct. 2005.

[52] T. E. Darcie, P. F. Driessen, "Class-AB techniques for high-dynamic-range microwave-photonic links," *IEEE Photon. Technol Lett.,* vol. 18, pp. 929-931, April 2006.

[53] E. I. Ackerman, S. Wanuga, J. MacDonald and J. Prince, "Balanced receiver external modulation fiber-optic link architecture with reduced noise figure," *Microwave Symp. Dig. (IEEE MTT-S.,* vol. 2, pp. 723-726, June 1993.

[54] L. T. Nichols, K. J. Williams and R. D. Esman,"Optimizing the ultra-wide-band photonic link," *IEEE Trans. Microw. Theory Tech.,* vol. 45, pp. 1384-1389, Aug. 1997.

[55] C. Y. Kuo, D. Piehler, C. Gall, J. Kleefeld, A. Nilsson and L. Middleton, "High performance optically-amplified 1550 nm lightwave AM-VSB CATV transport system," *OFC '96 Technical Degest,* vol. 2, paper WN2.

[56] D. Piehler, J. Kleefeld, C. Gall, C. Y. Kou, A. Nilsson and X. Zou, "Optical amplifiers and their applications," *Technical Degest, Monterey* , paper SaB2, 1996.

[57] Y. Wu, "Optical heterodyned radio over fiber link design using electro-absorption and electro-optic modulators," University of California, San Diego, Ph.D. thesis, Chapter 1, 2004.

[58] B. Masella, X. Zhang, "A novel single wavelength balanced system for radio over fiber links," *IEEE Photon. Technol Lett.,* vol. 18, pp. 301-303, Jan. 2006.

[59] F. Koyama, K. Iga, "Frequency chirping in external modulator," *J. Lightwave Technol.,* vol. 6, pp. 87-93, Jan. 1988.

[60] B. Liu, J. Shim, Y. Chiu, A. Keating, J. Piprek, J. E. Bowers, "Analog characterization of low-voltage MQW traveling-wave electro-absorption modulators," *J. Lightwave Technol.,* vol. 21, pp. 3011-3019, Dec. 2003.

[61] A. Loayssa, M. Alonso, D. Benito, M. Garde, "Linearization of electrooptic modulators at millimeter-wave frequencies," IEEE *Lasers and Electro-Optics Society (LEOS) Annual Meeting,* vol. 1, pp. 275-276, Nov. 1999.

[62] A. Loayssa, C. Lim, A. Nirmalathas, D. Benito,"Design and performance of the bidirectional optical single-sideband modulator," *J. Lightwave Technol.,* vol. 21, pp. 1071-1082, April 2003.

[63] B. Haas, T. Murphy, "A simple, linearized, phase-modulated analog optical transmission system," *IEEE Photon. Technol. Lett.,* vol. 19, pp. 729-731, May 2007.

[64] X. Gu, Y. He, H. Kosek and X. Fernando, "Transmission efficiency improvement in microwave fiber-optic link using sub-picometer optic bandpass filter," *Photonics North 2005*, Paper 5971-85, Toronto.

[65] M. Attygalle, C. Lim, G. Pendock, A. Nirmalathas and G. Edvell, "Transmission improvement in fiber wireless links using fiber Bragg grating," *IEEE Photon. Technol. Lett.,* vol. 17, pp. 190-192, Jan. 2005.

[66] A. Willner, K. Feng, J. Cai, S. Lee, J. Peng and H. Sun, "Tunable compensation of channel degrading effects using nonlinearly chirped passive fiber Bragg gratings," *IEEE J. Selected Topics in Quantum Electronics,* vol. 5, pp. 1298-1311, Sept. 1999.

[67] B. Masella, X. Zhang, "A simplified radio over fiber balanced system with suppression of both second and third-order nonlinear distortions," *Photonics North '06,* MIC-05-4-2, June. 2006.

[68] G. K. Gopalakrishnan, I. L. Gheorma, "Simultaneous, bidirectional modulation of two channels in single optical modulator," *IEEE Photon. Technol Lett.,* vol. 19, pp. 886-888, June 2007.

[69] I. L. Gheorma, G. K. Gopalakrishnan, "RF photonic techniques for same frequency simultaneous duplex antenna operation," *IEEE Photon. Technol Lett.,* vol. 19, pp. 1014-1016, July 2007.

[70] B. Masella, J. X. Zhang, "Linearized optical single sideband Mach-Zehnder electro-optic modulator for radio over fiber systems," *Optics Express,* vol. 1, pp. 9181-9190, June 2008.

[71] A. Loayssa, C. Lim, A. Nirmalathas, D. Benito, Design and performance of the bidirectional optical single-sideband modulator," J. Lightwave Technol. 21, 1071-1082 (2003)

[72] A. Ramaswamy, L. Johnsson, J. Klamkin, C. Shedon, H. Chou, M. Rodwell, L. Coldren, J. Bowers, "Coherent receiver based on a broadband optical phase locked loop," in Proc. OFC 2007, post deadline paper PDP3.

[73] B. Masella, J. X. Zhang, "Linearized optical single-sideband Mach–Zehnder modulator for radio-over-fiber systems," *IEEE Photon. Technol. Lett.,* vol. 19, pp. 2024-2026, Dec. 2007.

[74] L. M. Johnson, H. V. Roussell "Reduction of intermodulation distortion in interfermetric optical modulators," *Opt. Lett.,* vol. 13, pp. 928-930 Oct. 1988.

[75] S. A. Havstad, A. B. Sahin, O. H. Adamczyk, Y. Xie, A. E. Willner, "Distance-independent microwave and millimeter wave power fading compensation using a phase diversity configuration," *IEEE Photon. Technol. Lett.,* vol. 12, pp. 1052-1054, Aug. 2000.